

GIROMILL WIND TUNNEL TEST AND ANALYSIS
VOLUME 2. TECHNICAL DISCUSSION

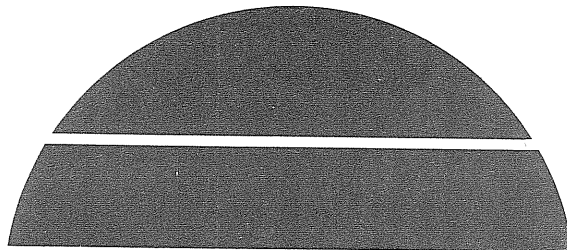
Final Report, June 1976—October 1977

By
W. A. Moran

October 1977
Date Published

Work Performed Under Contract No. EY-76-C-02-2617

McDonnell Aircraft Company
St. Louis, Missouri



U.S. Department of Energy



Solar Energy

AUG 7 1978

C. E. ELDERKIN

NOTICE

This report was prepared as an account of work sponsored by the United States Government. Neither the United States nor the United States Department of Energy, nor any of their employees, nor any of their contractors, subcontractors, or their employees, makes any warranty, express or implied, or assumes any legal liability or responsibility for the accuracy, completeness or usefulness of any information, apparatus, product or process disclosed, or represents that its use would not infringe privately owned rights.

This report has been reproduced directly from the best available copy.

Available from the National Technical Information Service, U. S. Department of Commerce, Springfield, Virginia 22161.

Price: Paper Copy \$6.00
Microfiche \$3.00

**GIROMILL WIND TUNNEL
TEST AND ANALYSIS
VOLUME II - TECHNICAL DISCUSSION**

Final Report for the
Period June 1976 - October 1977

W.A. Moran

MCDONNELL AIRCRAFT COMPANY
P.O. Box 516
St. Louis, Missouri 63166 (USA)

Date Published - October 1977

Prepared for the United States
Energy Research and Development Administration
Division of Solar Energy

Under Contract No. EY-76-C-02-2617.A001

FOREWORD

This report was prepared for the United States Energy Research and Development Administration (ERDA) by the McDonnell Aircraft Company, a division of the McDonnell Douglas Corporation, P.O. Box 516, St. Louis, Missouri, 63166. The study was performed under ERDA contract EY-76-C-02-2617.A001 (Formerly: E(11-1)-2617). This final report covers the period from June 1976 to September 1977.

The study was under the direction of Robert V. Brulle assisted by William A. Moran who performed the aerodynamic analysis and planned the wind tunnel test. Personnel contributing to the effort include, Joseph L. Anglin - model design, Paul R. Hendricks - instrumentation, and Richard Hardin - wind tunnel test engineer.

ABSTRACT

A wind tunnel test of a Giromill rotor was conducted. The objective of this test was to substantiate the performance computed by the Larsen cyclogiro vortex theory. Additional objectives were to obtain performance comparison data between the Giromill, a sinusoidal blade modulation Giromill, a Darrieus rotor, and a modified Darrieus rotor that flips the blades a few degrees.

A three bladed Giromill rotor having a diameter of 2.13 m (7 ft) and a span of 1.52 m (5 ft) was tested in the McDonnell Aircraft Company 15 x 20 ft. Mini Speed Wind Tunnel. The blade modulations were accomplished through use of a cam and push rod arrangement. Replaceable cams provided the desired blade modulation at the various operating points. Various operating conditions were achieved by adjusting the rotor RPM and tunnel speed. A total of 36 data runs were conducted at three nominal rotor RPM values; 80 and 100 RPM were used for the Giromill test mode, and 120 RPM for the Darrieus test mode. A torque meter measured the rotor torque and together with the measured RPM provided the rotor power.

The results show that the Giromill has good performance, equal to or much better than that predicted by theory, and outperforms the other types of vertical axis wind turbines tested. Continued use of the theoretically computed performance appears warranted. Based on that theory, the maximum power output of a Giromill is $C_{p_{\max}} = .54$.

TABLE OF CONTENTS

<u>Section</u>	<u>Page</u>
1. INTRODUCTION	1
2. WIND TUNNEL TEST PLAN ANALYSIS	3
3. MODEL DESIGN	8
4. INSTRUMENTATION	16
5. DATA REDUCTION	18
6. PERFORMANCE PREDICTION TECHNIQUES	21
7. WIND TUNNEL TEST	47
8. TEST RESULTS AND ANALYSIS	55
9. CONCLUSIONS	82
10. REFERENCES	84

LIST OF ILLUSTRATIONS

<u>Figure No.</u>	<u>Title</u>	<u>Page</u>
1	Giromill Concept	2
2	Model Design Parameter Relationships	4
3	Giromill Model Installation	7
4	Model Design Criteria	9
5	Blade Design	10
6	Lower Support Arm Assembly	11
7	Upper Support Arm Assembly	12
8	Blade Modulation Push Rod Assembly	13
9	Drive Train Installation	15
10	Rotor Control and Data Acquisition Schematic	17
11	Rotor Performance Data Sign Convention	19
12	Lift Curve Component Definitions	23
13	Lift Curve Slope vs Reynolds Number	24
14	Maximum Lift Coefficient vs Reynolds Number	24
15	Angle of Attack Change Between C_{l_B} and $C_{l_{max}}$ vs Reynolds Number	25
16	Lift Curve Break vs Reynolds Number	26
17	Lift Curve Used in Cyclogiro Vortex Theory Program	27
18	Two Dimensional Drag Due to Lift	29
19	Drag Due to Lift Above Stall	29
20	Drag Due to Lift Above Stall Used in Vortex Theory Program	30
21	Variation of Effective Arm Drag Coefficient with Blade Speed Ratio and Phase Angle	32
22	Drag Comparison - Upper Arm	32
23	Component Drag Coefficients	34
24	Zero Lift Equation Drag Coefficients	34

LIST OF ILLUSTRATIONS (Cont)

<u>Figure No.</u>	<u>Title</u>	<u>Page</u>
25	Giromill Model Performance Estimates from Vortex Theory Program	35
26	Blade Rock Angle Comparison	37
27	Giromill Model Performance Estimates from Vortex Theory Program	38
28	Giromill Blade Rotation	39
29	Induced Camber Effect	41
30	Giromill Model Performance Estimates Including Blade Rotation Rate Effects	44
31	Giromill Model Performance Estimates Including Blade Rotation Rate Effects	45
32	Predicted Darrieus Mode Performance Including Rotation Rate Effects	46
33	Giromill Test Record	48-49
34	Comparison Between Torque Meter Check Loadings and Calibration Curve	51
35	Probe Position Diagram	53
36	Velocity Comparison Hot Film Probe vs Pitot-Static System	56
37	Kollsman and Hot Film Probe Velocity Comparison	57
38	Percent Velocity Difference Between Tunnel System and Hot Film Probe vs Giromill Power Coefficient	58
39	Comparison Between Predicted Giromill Performance and Test Data at the CAM Design Points	59
40	Comparison Between Predicted Giromill Performance and Test Data at the CAM Design Points	60
41	Giromill Power Coefficient Variation with Blade Speed Ratio	62
42	Giromill Power Coefficient Variation with Blade Speed Ratio	63
43	Giromill Power Coefficient Variation with Blade Speed Ratio	64

LIST OF ILLUSTRATIONS (Cont)

<u>Figure No.</u>	<u>Title</u>	<u>Page</u>
44	Giromill Power Coefficient Variation with Blade Speed Ratio	65
45	Tare Run Data	66
46	Giromill Power Coefficient Variation with Blade Speed Ratio	67
47	Darrieus Mode Power Coefficient Variation with Blade Speed Ratio	69
48	Comparison Between Predicted Giromill Performance and Test Data at the CAM Design Points	71
49	Giromill Power Coefficient Variation with Blade Speed Ratio	72
50	Giromill Power Coefficient Variation with Blade Speed Ratio	73
51	Giromill Power Coefficient Variation with Blade Speed Ratio	74
52	Giromill Power Coefficient Variation with Blade Speed Ratio	75
53	Giromill Power Coefficient Variation with Blade Speed Ratio	77
54	Darrieus Mode Power Coefficient Variation with Blade Speed Ratio	78
55	Giromill Wind Tunnel Test Model Performance Envelope .	79
56	Giromill Wind Tunnel Test Model Performance Envelope .	80
57	Comparison of Computed and Test Giromill Performance Envelopes	81
58	Giromill Wind Tunnel Test Analog Tape Data Reduction	83

SYMBOLS AND DEFINITIONS

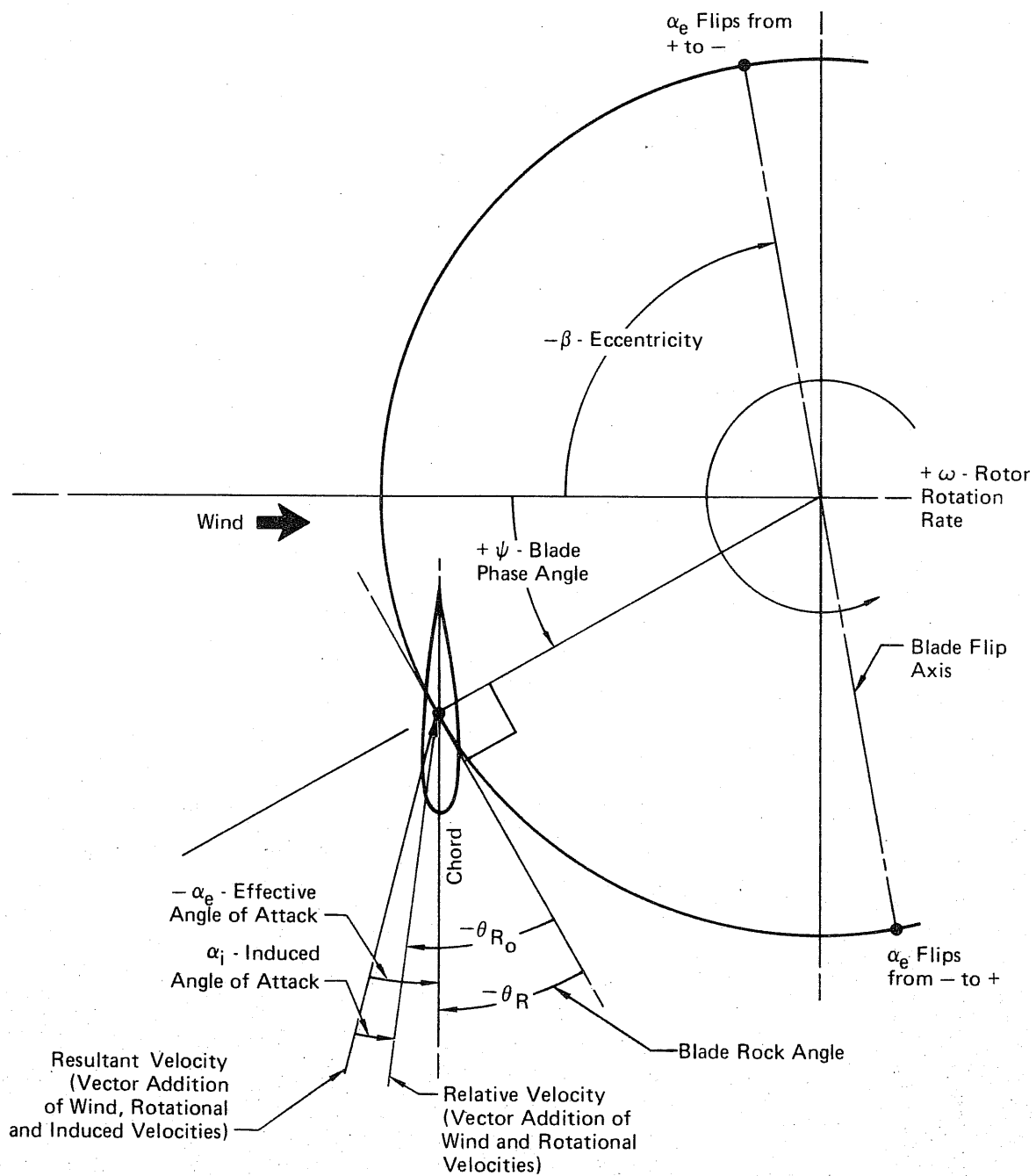
<u>Symbol</u>	<u>Definition</u>
A	Rotor Capture area = $b \times D = 35 \text{ FT}^2 (3.25 \text{ m}^2)$
a	Three dimensional lift curve slope
AR	Aspect ratio = $\frac{\text{span}}{\text{area}}$
b	Blade span, 5 ft. (1.52 m)
c	Chord blade or rotor arm, blade chord = .7 ft. (.213 m)
c_d	Two dimensional drag coefficient
c_{d_e}	A drag coefficient acting at the blade which produces the same torque about the hub as the integrated drag of the rotor arms
c_{d_o}	Two dimensional drag coefficient for zero lift
C_D	Three dimensional drag coefficient
C_{D_o}	Three dimensional drag coefficient for zero lift
C_{D_q}	Change in drag due to pitch rate $\partial C_D / \partial \frac{qc}{2V}$
c_l	Two dimensional lift coefficient
c_{l_α}	Two dimensional lift curve slope = $\frac{\partial c_l}{\partial \alpha}$
C_{l_B}	Lift coefficient at which lift curve becomes non linear
$C_{l_{\max}}$	Maximum two dimensional lift coefficient
C_L	Three dimensional lift coefficient
C_{L_q}	Change in lift due to pitch rate $\partial C_L / \partial \frac{qc}{2V}$
C_{L_α}	Three dimensional lift curve slope = $\frac{\partial C_L}{\partial \alpha}$
C_{M_q}	Change in pitching moment due to pitch rate $\partial C_M / \partial \frac{qc}{2V}$
C_P	Power Coefficient = $\frac{(Q-Q_F) \omega}{1/2 \rho V_T^3 A}$
$C_{P_{\max}}$	Maximum power coefficient
C_Q	Torque Coefficient = $\frac{(Q-Q_F)}{1/2 \rho V_T^2 R A}$
D	Rotor diameter = 7 ft (2.13 m)
E	Jones edge velocity correction factor = $\frac{\text{semi perimeter}}{\text{span}}$
f	Lift curve slope correction factor
N	Number of blades or number of data points

SYMBOLS AND DEFINITIONS (Continued)

<u>Symbol</u>	<u>Definition</u>
P	Tunnel static pressure
P _T	Tunnel total pressure
Q	Measured torque
Q _F	Torque due to friction
q	Tunnel dynamic pressure, or pitch rate
RN	Reynolds Number = $\frac{r\omega c}{\nu}$
r	Radius of point of interest from Giromill center or rotation
R	Blade radius = 3.5 ft (1.07 m)
S _B	Blade reference area = 3.5 ft ² (0.325 m ²)
S _A	Rotor arm reference area
T	Tunnel temperature
V _B	Blade velocity = $V_W \lambda^2 - 2\lambda \sin \psi + 1$
V _K	Tunnel free stream velocity measured by Kollsman pitot-static probe
V _P	Tunnel free stream velocity measured by hot film anemometer probe
V _T	Tunnel free stream velocity measured by mini speed pitot-static system
V _W	True free stream velocity
α	Angle of attack measured from the free stream velocity vector to the chord plane
α_B	Angle of attack where lift curve becomes non-linear
α_e	Angle of attack measured from the resultant velocity vector which includes the rotor induced velocities, to the blade chord. This α_e is equivalent to the α relating the two dimensional airfoil characteristics
α_{\max}	Angle of attack for $C_{l_{\max}}$
α_w	Angle between relative wind and line tangent to blade path
β	Eccentricity or blade phase angle where blade flips from a positive to negative effective angle of attack
θ_R	Blade rock angle

SYMBOLS AND DEFINITIONS (Continued)

<u>Symbol</u>	<u>Definition</u>
λ	Blade speed ratio $\frac{\omega R}{V_T}$
ν	Kinematic viscosity
ρ	Tunnel air density
σ	Solidity $\frac{Nc}{2R}$
ψ	Blade phase angle
ω	Rotor rotation rate



Note: Some angles shown negative to be consistent with normal Giromill operating conditions.

CYCLOGIRO ROTOR PARAMETERS DEFINITION

SUMMARY

The feasibility of the Giromill as a viable wind energy conversion system was verified by the initial one year feasibility study completed in May 1976. The study described herein continues the Giromill investigation by performing a wind tunnel test of a model Giromill rotor.

The primary objective of the wind tunnel test was to obtain data for comparison with the Larsen cyclogiro vortex theory program employed for predicting the Giromill performance.

The model had a rotor diameter of 7 ft. (2.13 meters) and a solidity (total blade area divided by rotor span times diameter) of 0.3. This was achieved by a three bladed rotor having blade chords of 8.4 in. (21.3 cm) and a span of 5 ft. (1.52 meters). The blades were modulated by use of replaceable cams, that simulated the various operating conditions, and a push rod arrangement connected to a bellcrank about the blade pivot point. The push rod was recessed in the lower blade support arm to reduce unwanted drag. Rotor RPM control was achieved with an electric motor/generator that could be used to either drive the rotor or absorb the rotor power in a light bank to maintain RPM. A torque meter measured the rotor shaft torque, and together with the RPM was used to measure the power of the rotor.

Due to the importance of accurate velocity measurement on the measured performance, and due to the low velocities necessary for this test, two independent velocity measurement systems were used; the standard pitot-static tunnel system and a hot film anemometer system. These two systems differed by approximately 11% during the test with the hot film velocity being the lower. This difference could not be resolved. The best overall agreement with predicted performance was achieved using the pitot-static system to reduce the data but credible evidence also exists to support the higher performance based on the hot film velocity.

Until the higher performance is verified by future tests, the Larsen Cyclogiro vortex theory program will be used to predict performance.

1. INTRODUCTION

A wind tunnel test was conducted on a model of a Giromill wind turbine. The Giromill is shown in Figure 1. It consists of a number of vertical blades rotating around a central tower. The blade angles of attack are individually modulated to achieve high conversion efficiency regardless of the wind direction. Thus compared to conventional windmills, tower and blade construction are considerably simplified.

The objective of this current study was to obtain wind tunnel test data on a model Giromill rotor to verify the theoretical results computed by the Larsen cyclogiro vortex theory program.

Secondary objectives include the comparison of the Giromill blade modulation scheme of operation with, (1) a sinusoidal blade modulation scheme, (2) a Darrieus mode of operation, and (3) a modified Darrieus mode where the blades are flipped ± 3 degrees.

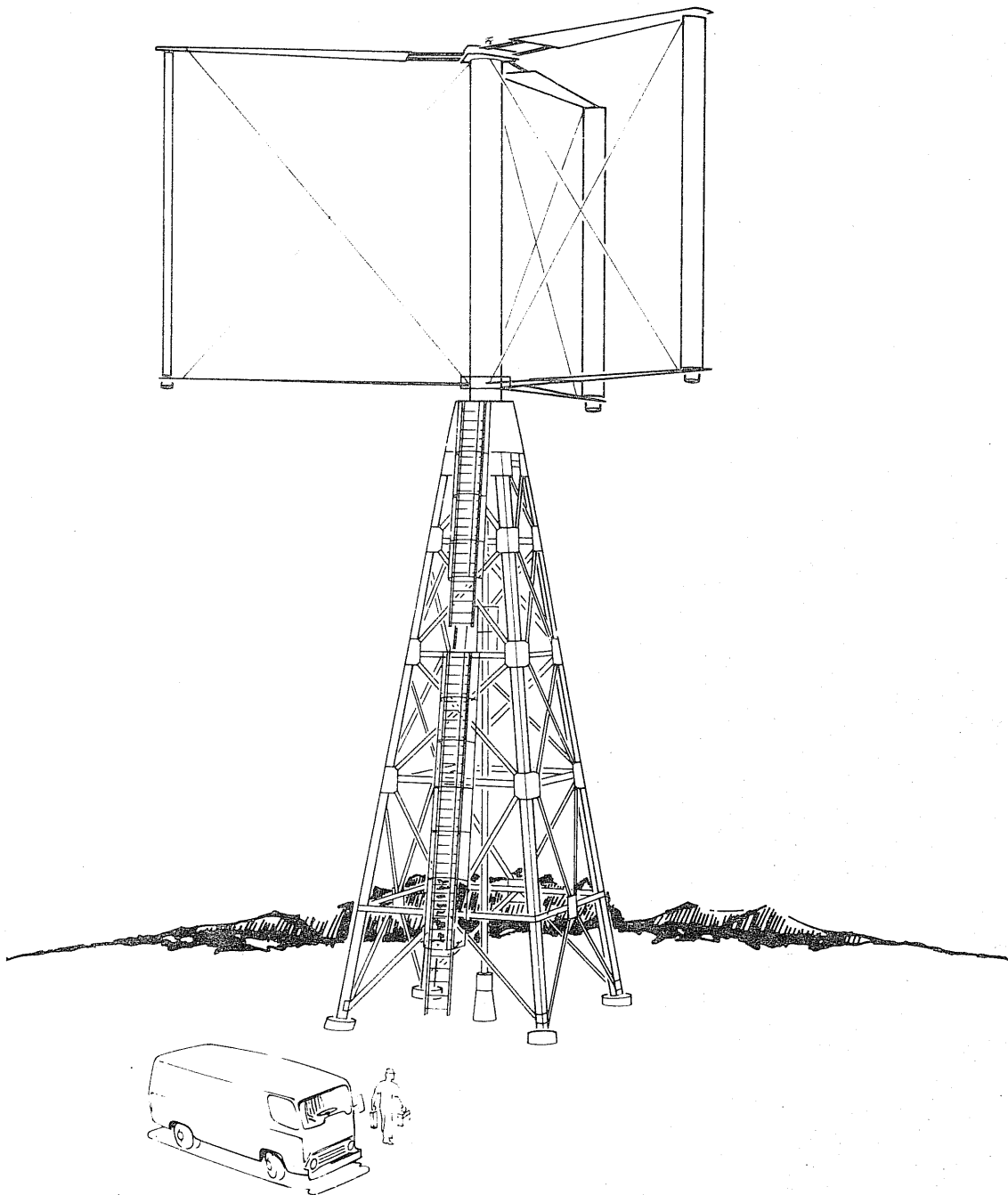


FIGURE 1
GIROMILL CONCEPT

2. WIND TUNNEL TEST PLAN ANALYSIS

2.1 Plan Rationale

The Larsen cyclogiro vortex theory computer program, described in Reference 1, is used for predicting the Giromill performance. The wind tunnel model test was for the purpose of obtaining data to compare with the Larsen vortex theory program computation results. The wind tunnel model itself does not have to be a scale model of the full size production system. The rationale, regarding Giromill performance validation, is to use the wind tunnel test results to verify the estimated model performance, based on model characteristics, and thereby show the Larsen cyclogiro computer program to be satisfactory. Hence the performance of the full scale Giromill systems can be computed with confidence. If the wind tunnel test results do not validate the predicted performance, then sufficient data should be available from the test to allow a discrepancy analysis to be conducted to ascertain the reasons for the variance.

2.2 Model Design Parameter Relationships

The test was conducted in the McDonnell Aircraft Company 15 x 20 foot (4.6 x 6.1 meter) Mini-Speed Wind Tunnel (MSWT). This tunnel is an open circuit continuous flow tunnel with an open jet test section. Controlled velocities down to 1 meter/sec (mps) can be achieved.

The model design was required to be sufficiently flexible to allow the gathering of all data needed to achieve the test objectives, and to account for the various constraints dictated by the model, tunnel limitations, testing limitations, and data requirements.

The relationships between the Giromill model rotor diameter (D), RPM, solidity (σ), and blade chord (c) were formulated and are plotted in Figure 2. This figure shows the parameter trade offs that were considered in selecting the model design point. A constant tunnel wind speed of 4.1 mps was assumed for these relationships.

A small diameter Giromill rotor operates at a high RPM. A high RPM increases the centrifugal load on the blades and creates greater dynamic problems. Thus, one tends towards selecting a model having a large diameter and high solidity, since both of these parameters reduce the operating RPM. However, the diameter of the model is limited by the size of the tunnel. Too large a diameter will create tunnel blockage or flow variations which may invalidate the results of the test. Increasing the solidity of the rotor also has the effect of decreasing the operating RPM. There is, however, a limit as to how far one can increase the solidity. This is because it was decided to use a cam and push rod arrangement to modulate the blades.

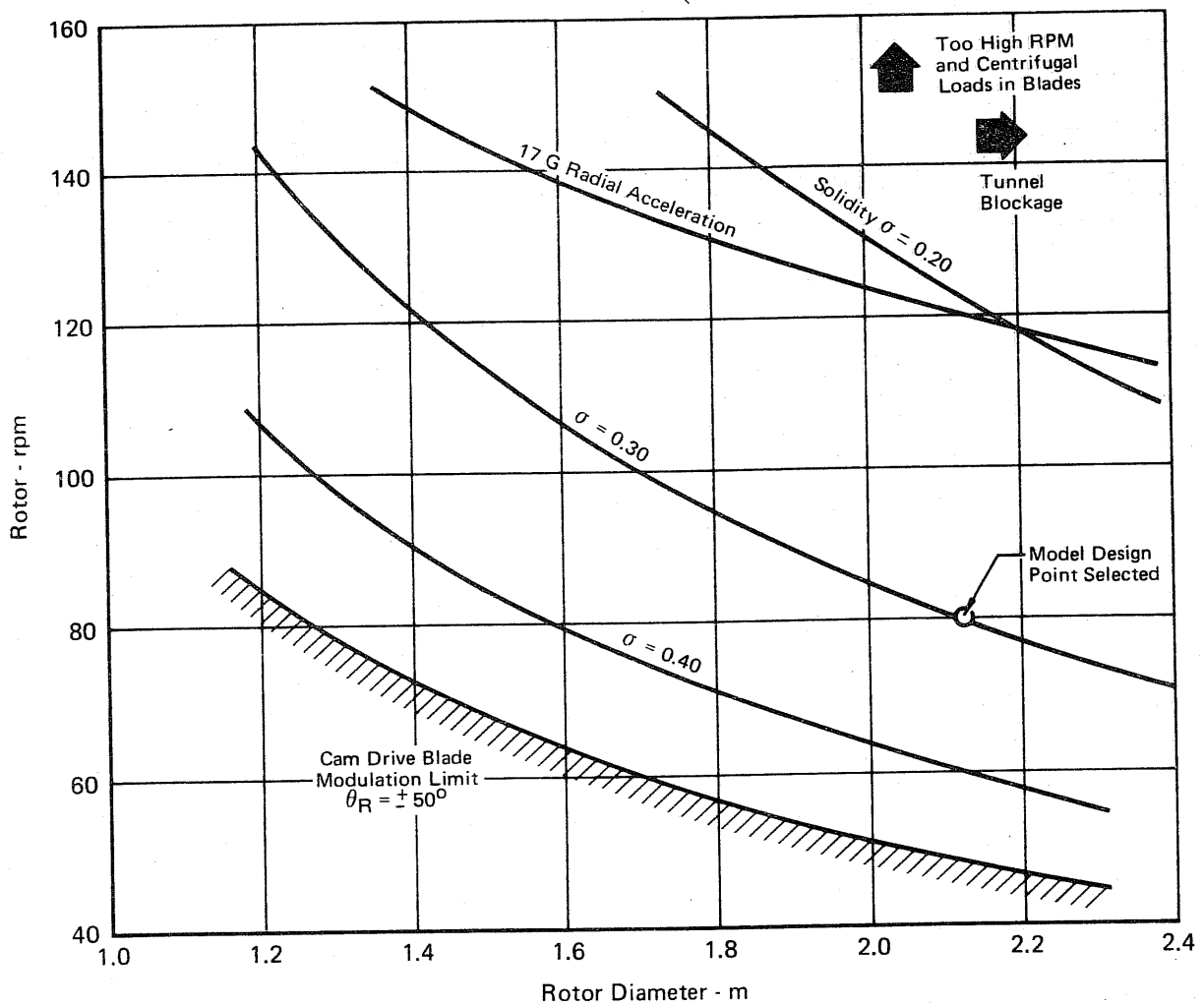


FIGURE 2
MODEL DESIGN PARAMETER RELATIONSHIPS
 Tunnel Wind Velocity = 4.1 MPS

A cam and push rod connected to a bellcrank about the blade pivot limits the blade modulation to about ± 50 degrees, which in turn limits the model rotor solidity as shown in Figure 2. This type of blade modulation scheme was selected to reduce the cost of the test. It was determined that the blade modulation cams could easily be fabricated using a numerically controlled milling machine and the model designed to allow quick cam changes for the various test conditions.

High solidity also increases the effect of blade moments and other forces tending to retard the rotor due to the blade pitching as it rotates. A theoretical correction derived in this report is applied to account for the effect of blade rotation rate. This effect is approximately proportional to the cube of solidity, and a large theoretical correction is not desirable.

Accounting for all of the above parameters resulted in the selection of the model design point shown in Figure 2. The rotor has a diameter of 2.13 meters and a solidity (σ) of 0.300 (based on rotor capture area). This was achieved by a three bladed rotor having a blade chord of 21 cm. The rotor span was chosen to be as large as practical to maximize the various aerodynamic forces to be measured but also avoid tunnel blockage. A span of 1.52 meters was selected. Design details of the model are discussed in Section 3.

Two methods of obtaining data at various blade speed ratios (λ 's) are possible. One is by varying the tunnel wind speed at constant RPM. The other is by varying rotor RPM at a constant tunnel speed. Analysis of these two methods led to selection of essentially a constant RPM test operation and changing the tunnel wind speed to achieve the various λ 's.

Several factors influenced this decision; 1) constant RPM operation would decrease the risk of encountering structural resonance frequencies, 2) average Reynolds number is merely a function of RPM, 3) constant RPM causes the least variation in rotor and cam drive friction tare. The nominal RPM selected for Giromill mode testing was originally 80 but was increased to 100 during the test for increased accuracy. The Darrieus mode tests were run at 120 RPM.

The blade modulation schemes implemented by the various cams were defined theoretically. In order to evaluate the applicability of these theoretical modulation schemes, it was necessary to vary the blade speed ratio a small amount about

the nominal value. This small variation in λ was implemented by varying the RPM a small amount about the nominal value. The procedure arrived at to evaluate a cam modulation scheme was to first adjust the tunnel speed and rotor RPM to the nominal values, and then vary slightly the rotor RPM to obtain the λ variation desired.

Rotor RPM control was achieved with a three HP electric motor/generator connected to the rotor support pedestal and attached to the rotor shaft through a torque balance and RPM sensor. The motor could be used to either drive the rotor or absorb the rotor power by acting as either a motor or a generator. The output of the torque balance and RPM sensor were used to obtain the rotor shaft power. The system is based on the Sandia Laboratories design used in the wind tunnel test of the Darrieus Rotor reported in Reference 3. A sketch of the Giromill rotor installed in the mini-speed wind tunnel is shown in Figure 3.

The Giromill was the primary operating mode tested. In addition to the Giromill operation, limited tests of a sinusoidal blade modulation Giromill mode were run. This type of modulation was obtained by a cam that has a sine wave fit to the blade modulation scheme computed by the cyclogiro vortex theory program. Also two Darrieus type modes with the blades rocked $+3^\circ$ (or -3°) on the upwind side and -3° (or $+3^\circ$) on the downwind side were tested.

When operating in the Giromill mode, 80 RPM was originally planned because of the unknown effects of high RPM and attendant high radial acceleration loads on the rock angle cam drive system when large blade modulation rock angles were being used. The Darrieus mode which must operate at a high blade speed ratio and does not have blade rock angle modulations (the $\pm 3^\circ$ flip modes, has very small modulations) was scheduled to be run at 120 RPM to avoid operating at unacceptably low tunnel velocities. After verification during the test that 100 RPM could be used for the Giromill mode, this operating speed was used for the remaining Giromill runs. This enabled a 55% increase in dynamic pressure and therefore greater accuracy over the 80 RPM runs.

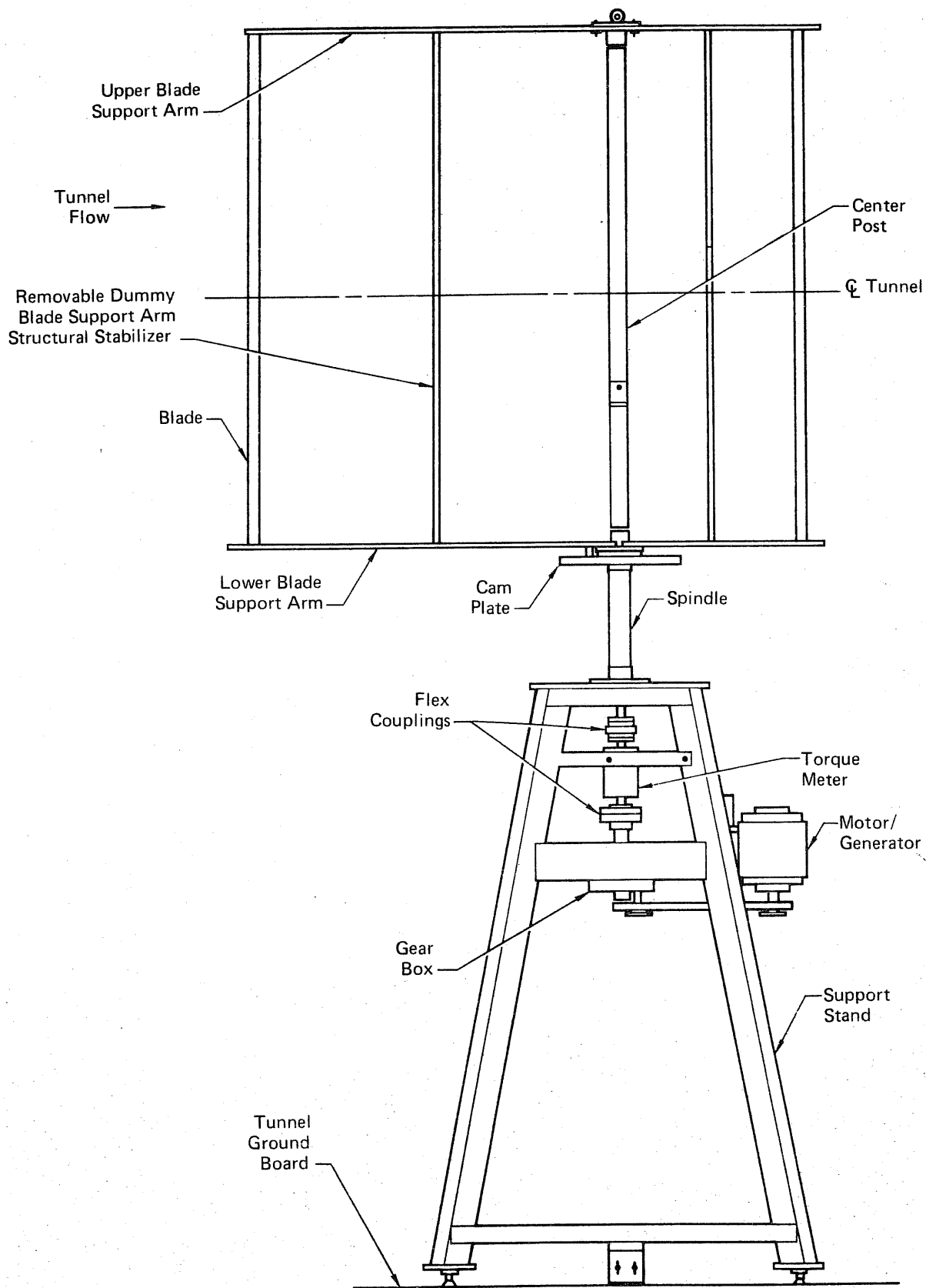


FIGURE 3
GIROMILL MODEL INSTALLATION

3. MODEL DESIGN

Model design criteria were established to fulfill the objectives of the test previously described. The model was then designed to these criteria. The design criteria established are summarized in Figure 4. A drawing showing the model installation in the tunnel was presented in Figure 3. Brief descriptions of several of the more pertinent parts follows.

The blades had a leading edge of aluminum backed by a balsa wood aft section. The entire blade was covered with a layer of silk, doped and painted. Figure 5 presents a drawing of the blade design.

The upper and lower blade support arms and the vertical blade support arms structural stabilizers were all made from aluminum. The support arms structural stabilizers were used only during runs to determine their power degradation for use in design of full scale Giromills. They were not structurally required for this model and were removed for all other runs. The upper arms and vertical blade support arm structural stabilizers were contoured into a NACA 0015 airfoil shape. The lower arm had an NACA 0015 airfoil shape outboard of 30% of the radius. A blade modulation push rod cut out was milled in the arm airfoil shape. Inboard of the 30% radius the leading edge of the lower arm had a round shape and the trailing edge was cut away to expose the push rod assembly. The arm was flared out at the blade end to accommodate a larger cut out needed for the blade modulation bellcrank assembly. The lower support arm assembly is shown in Figure 6, and the upper support arm assembly in Figure 7.

The center post consisted of a stainless steel two inch tube. A solid stainless steel axle was fitted in the lower 20 inches inside this tube. The axle continued down through the spindle and bearings to react the rotor bending load. Steel flanges welded to the center post carried the blade support arms. A steel spindle, fastened to a structural steel model support stand, supports the axle through a pair of low friction ball bearings set 15 inches apart.

A blade modulation push rod assembly was fitted in each lower blade support arm. This push rod assembly followed the blade modulation cam and transmitted the motion through a bellcrank to the blade. A spring kept a low friction cam follower bearing, slightly smaller than the cam slot, riding on the inner surface of the cam slot. The cams were made of aluminum. To facilitate cam installation, they were made from two pieces butted together and tack welded. After the cam slot was milled, and the installation hole pattern drilled, the tack weld was broken to provide a two part cam. Figure 8 shows the blade modulation push rod assembly.

Design Features

- Three bladed Giromill rotor ($N = 3$)
- Diameter (D) = 7 ft (2.1 m)
- Span (b) = 5 ft (1.5 m)
- Blade chord (c) = 0.7 ft (0.2 m)
- Rotor solidity (σ) = $\frac{Nc}{D} = 0.3$
- Blade airfoil NACA 0015
- Blade pivot 25% c
- Blade c.g. should be at or slightly forward 25% c
- Maximum windward drag force on the rotor is 8 lb (36 N)
- Maximum blade airload normal force is about 20 lb (89 N) (100 rpm operating in Giromill mode)
- Blade airload normal force in Darrieus mode is about 10 lb (44 N) (120 rpm)
- Use low friction bearings throughout the model
- Blade support arms must be streamlined from about 30% outboard from the axis
- Blade modulation push rod should be recessed within the blade support arm

Rotor Test Modes

- Giromill mode must provide a blade modulation capability of about ± 50 degrees
- Sinusoidal Giromill mode
- Darrieus mode
- Modified Darrieus mode where the blades are flipped 3 degree over 30 degrees of rotor travel as the blades pass through 90 and 270 degree blade phase angle

Rotor Test Regions

- Giromill and sinusoidal Giromill modes will be run at a nominal 80 and 100 rpm with blade speed ratios (λ) from 1.3 to 3.5
- Darrieus and modified Darrieus modes will be run at a nominal 120 rpm with blade speed ratios from 2.0 to 5.5

Instrumentation

Parameters to be measured are:

- Rotor torque (Q)
- Rotor rpm
- Blade 1 phase angle (ψ)
- Tunnel conditions
 - Test velocity (V_W)
 - Dynamic pressure (q)
 - Static temperature (T)
 - Static pressure (P)

FIGURE 4
MODEL DESIGN CRITERIA

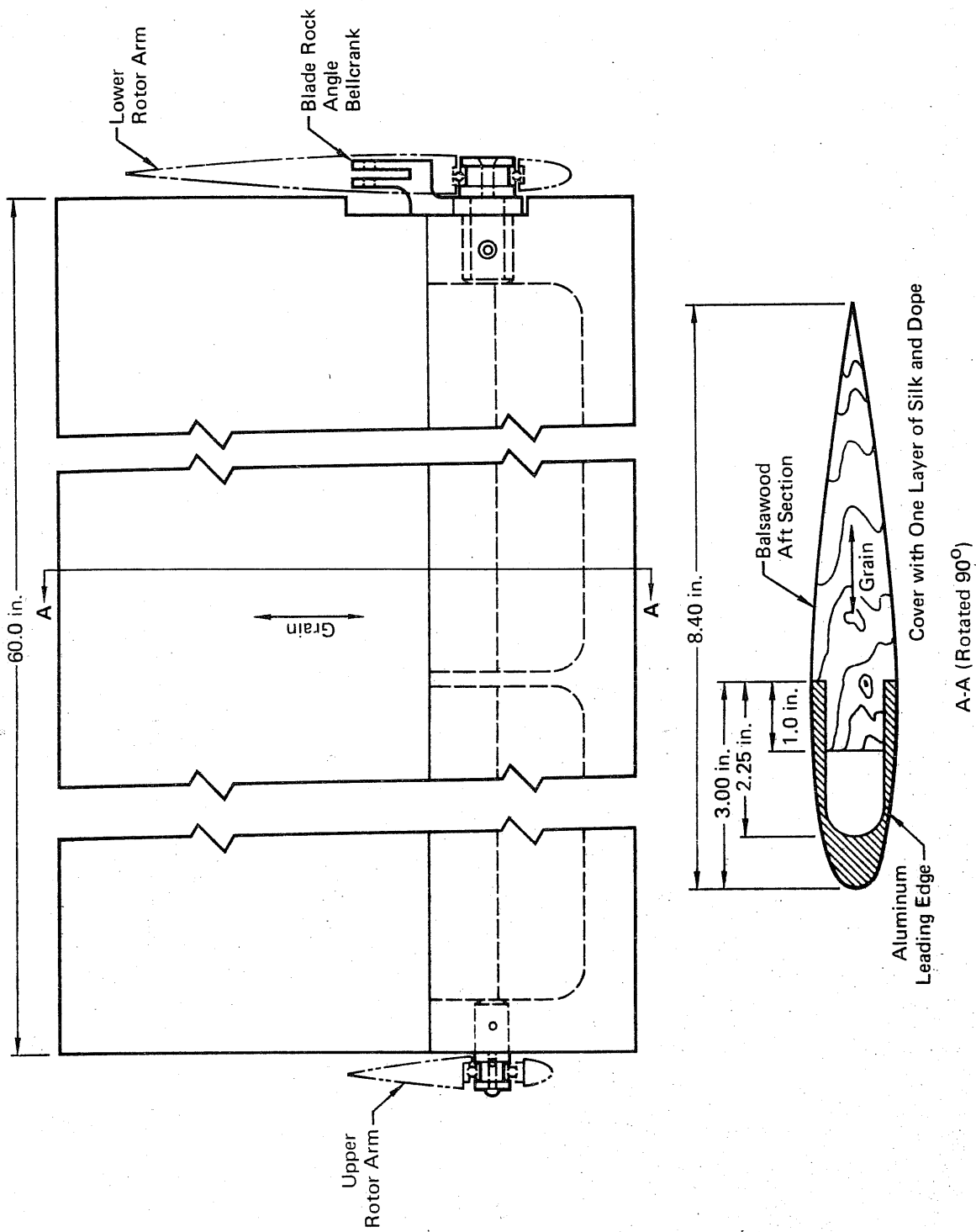


FIGURE 5
BLADE DESIGN

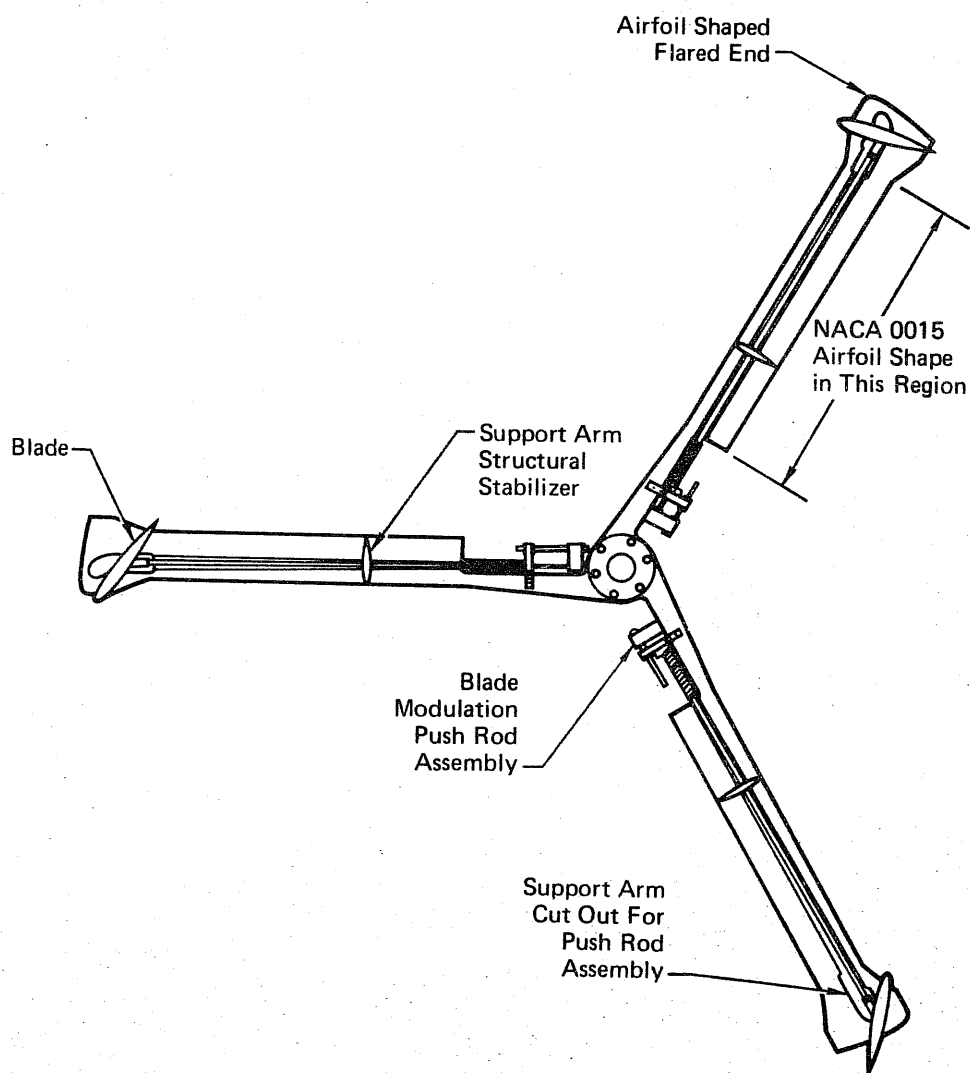


FIGURE 6
LOWER SUPPORT ARM ASSEMBLY

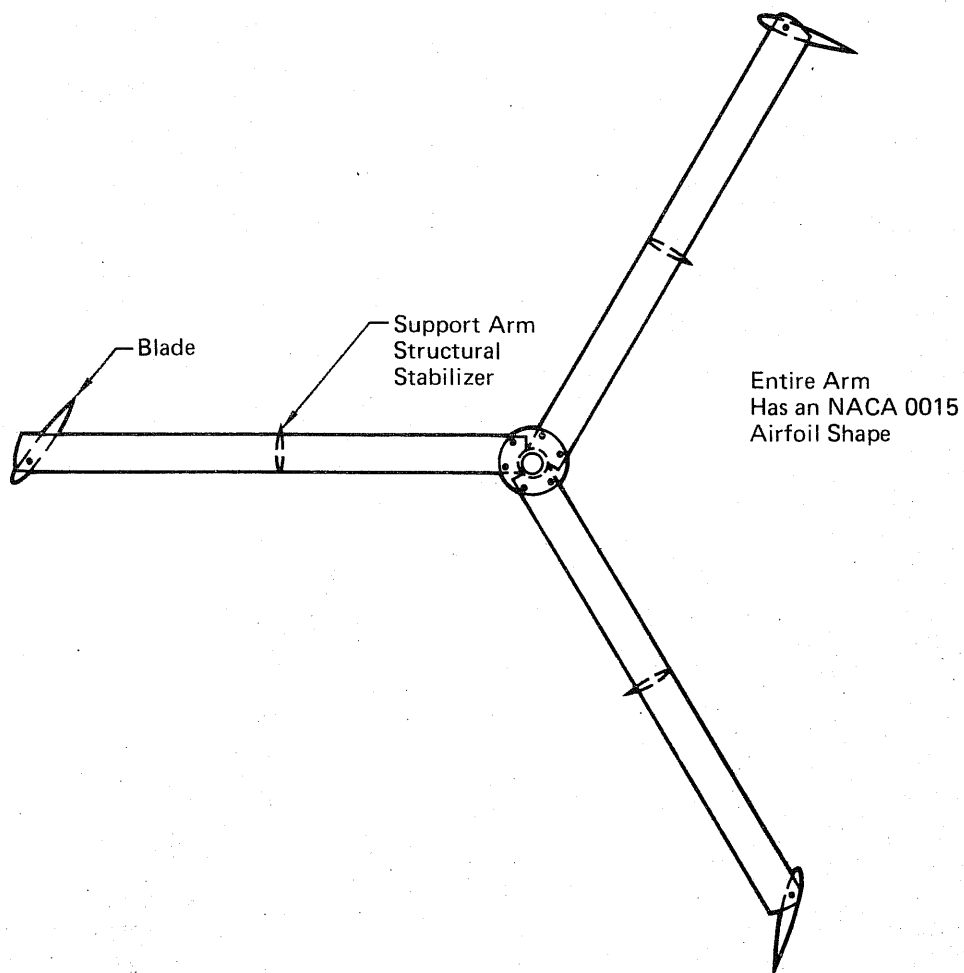


FIGURE 7
UPPER SUPPORT ARM ASSEMBLY

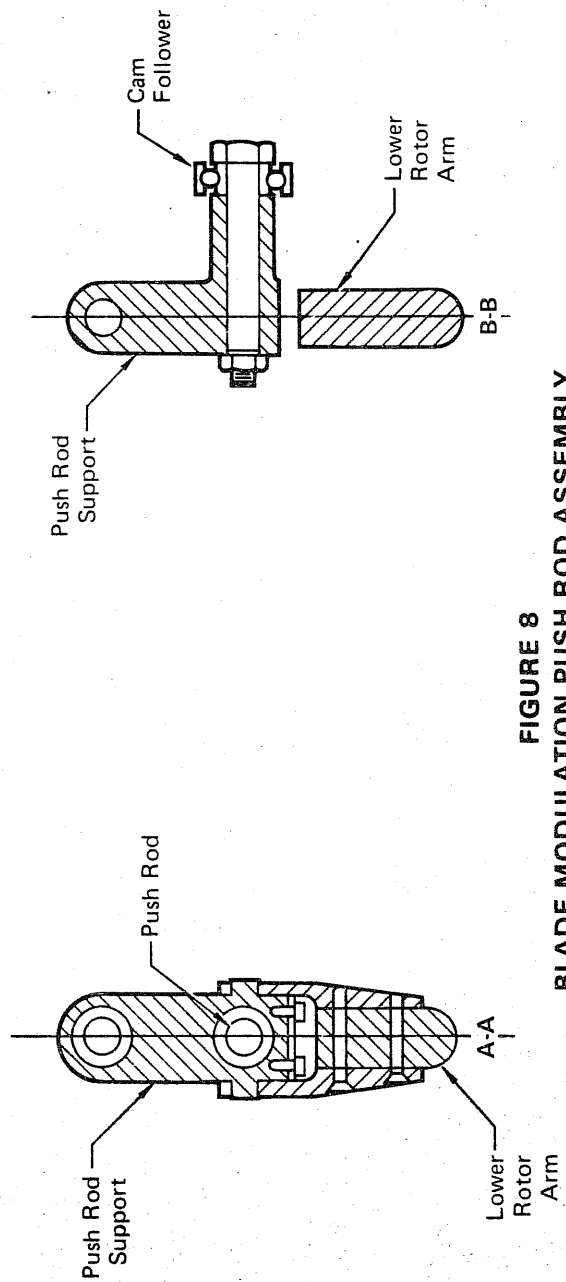
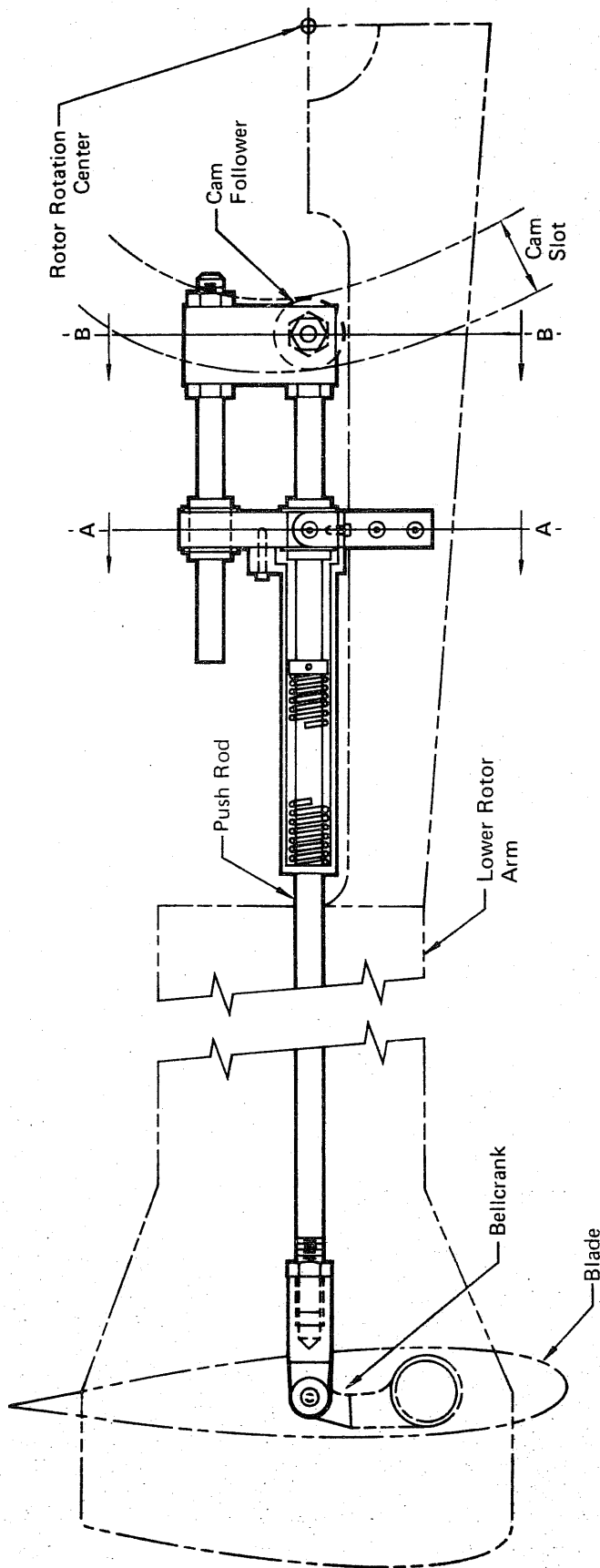


FIGURE 8
BLADE MODULATION PUSH ROD ASSEMBLY

RPM of the rotor was controlled by a motor/generator that either provided power as a motor or acted as a generator to absorb power to maintain RPM. The power from the generator was dissipated in a light bank. The motor/generator was connected to the rotor through a drive train consisting of a belt drive, gear box, two flexible couplings, and a torque meter. The installation is shown in Figure 9. The gear box and belt drive increase the Giromill rotor RPM from 80 to about 1000 at the motor/generator. The torque meter, isolated by the two flexible couplings, measured the torque and RPM. Two equal size gears transmit the rotor motion to a potentiometer that was calibrated to measure blade 1 phase angle. The entire drive train installation was mounted on the support stand as illustrated in Figure 3.

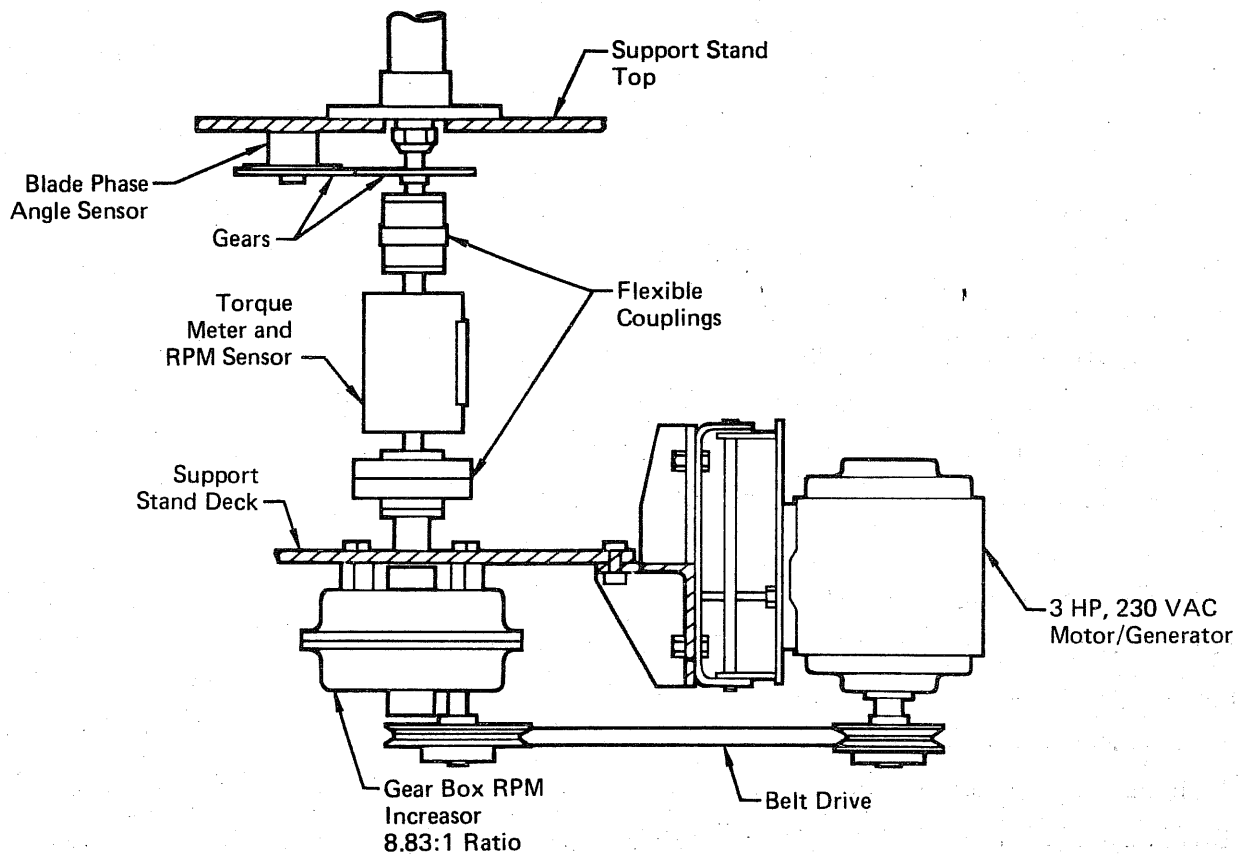


FIGURE 9
DRIVE TRAIN INSTALLATION

4. INSTRUMENTATION

Rotor RPM and shaft torque, from which power was calculated, was measured by a Lebow Model 1104-200 strain gauge type torquemeter. The installation arrangement was shown in Figure 9. RPM was sensed by a magnetic pickup within the torque meter and displayed on a digital counter as an operational parameter. The RPM signal was also conditioned in an ANADEx model PI 608 frequency to d.c. converter and recorded on the Digital Data Acquisition System (DDAS). The DDAS is the MSWT data collection and processing system. The torque signal was recorded on an analog channel of the DDAS.

Blade 1 phase angle was measured by a Bourns Model 6574 single turn precision potentiometer geared to the rotor shaft on a one to one gearing ratio. The signal was recorded on an analog channel of the DDAS.

Wind tunnel airspeed was measured by two methods. One was the standard MSWT velocity system which consists of differential pressure measurement of total and static pressure, using four pitot tubes located symmetrically around the tunnel bellmouth. The four totals are manifolded together, as are the four statics, and the differential pressure is measured with a Datametric model 1015S electronic Manometer. The Electronic Manometer has a digital output which is recorded with five digit precision. The tunnel air temperature is measured with a thermocouple and 150°F reference junction box and recorded on an analog channel.

At the extremely low air speeds of this test, airspeed accuracy is the limiting factor in the accuracy of the results. An alternative system which promised improved airspeed measurement accuracy was a Thermo System Inc. hot film anemometer featuring a model 1210-60 probe and a model 1050 anemometer module. The probe was located 8'9" ahead of the model centerline and 1 ft. above top of the rotor in order to obviate any interference effects between probe and model.

Two Endevco Model 2226C accelerometers, orthogonally aligned, were placed on the support spindle just below the cam plate. The signals were conditioned through an Endevco Model 2709 charge amplifier and displayed on a Brush MK 200 eight channel strip chart recorder by the tunnel control console. These accelerometers were monitored during the test to assure that no model vibrations occurred that could cause structural dynamic instabilities.

Figure 10 presents a schematic of the rotor control and data acquisition system described in this section.

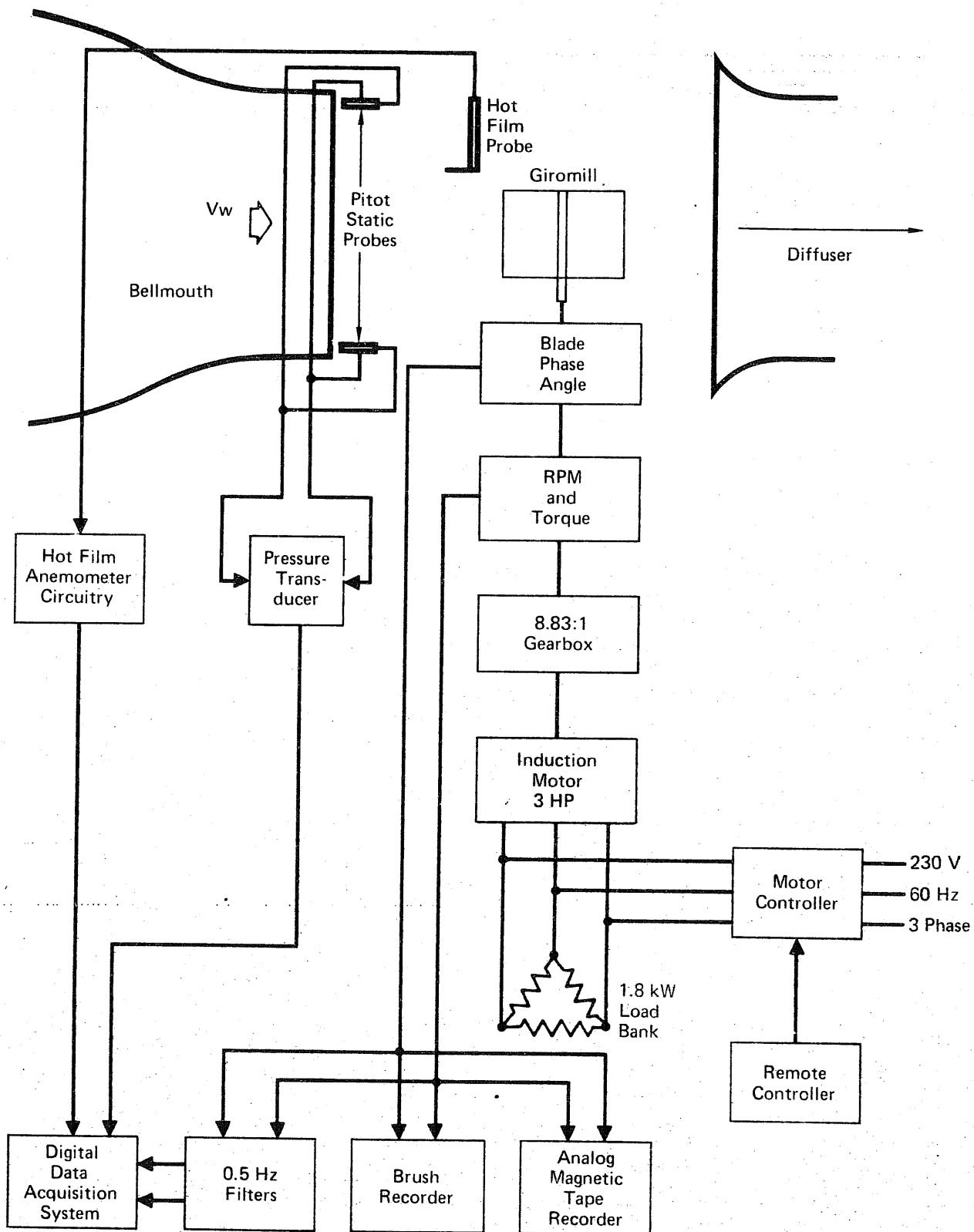


FIGURE 10
ROTOR CONTROL AND DATA ACQUISITION SCHEMATIC

5. DATA REDUCTION

The procedures and equations used for reducing the test data collected are described in this section. Rotor digital data collected during the test consisted of:

Torque	- Q - in lbs
Rotor rotation rate	- RPM
Test section tunnel velocity	- V_W - ft/sec
Test section tunnel dynamic pressure	- q - lbs/sq ft
Blade 1 phase angle	- ψ - deg

The Giromill rotor turns counterclockwise looking down on the model. This is defined as a positive rotation. A positive torque is defined as a torque tending to turn the rotor in a positive (counterclockwise) direction. Using this torque definition means that the bearing friction torque and torque due to support arm drag is negative.

Blade 1 phase angle, ψ , is measured counterclockwise from the tunnel wind velocity as shown in Figure 11. Blade numbering is as shown with blade 1 arbitrarily selected.

Multiple data points of the above parameters were obtained. Two samples were taken at a data rate of 10 points per second (fastest rate possible) for 2 seconds each ($N = 40$ points). There was a random time period pause between each sample. A printout of each rotor data point was obtained. Data reduction calculations using the data collected were computed as follows and printed out.

$$\text{Average torque } Q_{av} = \frac{\sum_{1}^N Q}{N}$$

$$\text{Average RPM } RPM_{av} = \frac{\sum_{1}^N RPM}{N}$$

$$\text{Blade speed ratio } \lambda = \frac{2\pi RPM_{av} R}{60 V_W}$$

R = Rotor radius = 3.5 ft. (1.07m)

Torque coefficient (uncorrected for friction torque)

$$C_Q = \frac{Q_{av}(1/12)}{1/2 \rho A V_W^2 R} = \frac{Q_{av}(1/12)}{q A R}$$

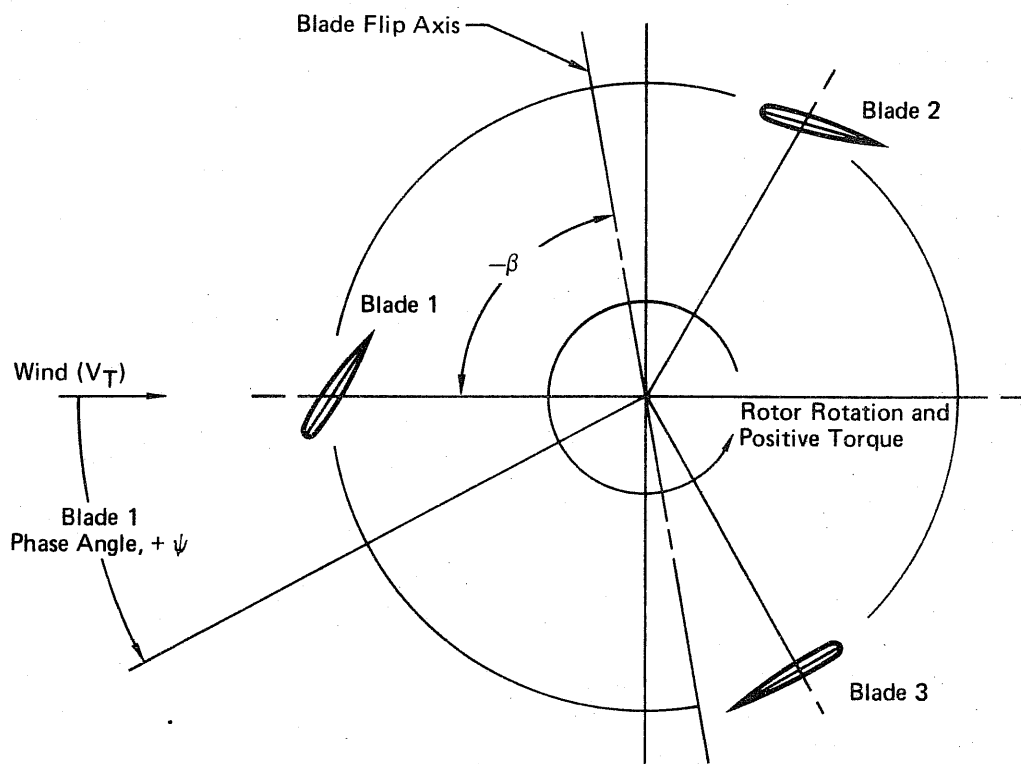


FIGURE 11
ROTOR PERFORMANCE DATA SIGN CONVENTION

A = Rotor capture area (span x dia) = 35 sq. ft. (3.25 m²)

Power coefficient (uncorrected for friction torque)

$$C_p = \frac{Q_{av} (1/12) \left(\frac{2\pi \text{ RPM}_{av}}{60} \right)}{1/2 \rho A V_W^3} = C_Q \lambda$$

The torque and power coefficients corrected for friction torque were also calculated. The friction torque correction was obtained as described in Section 7.1 from the tare data collected, and was input to the data reduction program as a function of test RPM.

The maximum data rate of 10 points per second resulted in one data point every 48° at 80 RPM and one data point every 72° at 120 RPM. This spacing was not small enough to ensure that an accurate average torque could be obtained using the values obtained at these phase angles. The torque signal was therefore transmitted through a .5 Hz filter before being recorded. Although this greatly increased the average torque accuracy, any time variation of torque was suppressed, therefore, unfiltered torque, along with the RPM, and blade phase angle were recorded on analog magnetic tape for later reduction at a high data rate.

6. PERFORMANCE PREDICTION TECHNIQUES

The Larsen cyclogiro vortex theory program described in Reference 1 was used to calculate the performance of the Giromill wind tunnel model. Additional corrections accounting for blade rotation rate were applied to the vortex theory results to arrive at a final performance prediction. Blade lift and total rotor drag coefficients are used in the calculation. The coefficients are dependent on the blade airfoil, rotor configuration and the test Reynolds number (RN). The drag includes drag on the blades, the support arms, guy wires, and any interference drag between the blade and the support arms. The total drag must be related to an equivalent drag coefficient acting on the blade for use in the program.

The following is the rationale used to estimate the lift and drag characteristics of the Giromill wind tunnel model and the resulting performance computed using the cyclogiro vortex theory program.

6.1 Aerodynamic Analysis

The Giromill wind tunnel model operates at a much lower Reynolds number than a full scale Giromill. The NACA 0015 airfoil section was chosen for the wind tunnel model because of the relatively large amount of wind tunnel data available at low RN and because its characteristics in the expected RN range are better (less drag for equal lift) than any other symmetrical section for which data were available.

The average Reynolds number, RN_{av} , for the wind tunnel model, is computed by:

$$RN_{av} = \frac{R\omega c}{v} = 1634.2 \text{ (RPM)}$$

and the RN range is computed by

$$RN_{av} \left(1 - \frac{1}{\lambda}\right) \leq RN \leq RN_{av} \left(1 + \frac{1}{\lambda}\right)$$

For 80 RPM and $\lambda = 1.3$, the RN range is 30,200 to 231,300 with an average RN of 130,700. This is the lowest λ test value, and results in the lowest minimum and highest maximum values of Reynolds number.

The lift curve characteristics used in the Larsen cyclogiro computer program must be two dimensional, the three dimensional effect being calculated within the program. The two dimensional (section) lift curve for the Giromill model was constructed from the data presented in References 4 and 5. The data from Reference 4 are two dimensional, while the data from Reference 5 are three dimensional referenced to an aspect ratio, AR, of six.

The two dimensional data from Reference 4 were corrected for the Jones edge-velocity factor, E (Reference 6, Page 11). E is the ratio of the semiperimeter to the span of the Giromill model blade. The correction takes the form

$$C_{l_{\alpha}} \text{ (Giromill blade)} = C_{l_{\alpha}} \text{ (Ref. 4)} \frac{E \text{ (Ref. 4)}}{E \text{ (Giromill)}}$$

For the Giromill blade $E = 1.14$.

The three dimensional data from Reference 5 were first reduced to two dimensional form using the relationship obtained by rearranging the equation presented in Reference 6, Page 11 to

$$a_e = \frac{a/f}{1 - \frac{a}{f} \frac{57.3}{\pi AR}}$$

In our symbology and accounting for the Jones edge velocity factor

$$C_{l_{\alpha}} \text{ (Giromill)} = \frac{\frac{C_{L_{\alpha}} \text{ (Ref. 5)}}{f \text{ (Ref. 5)}}}{1 - \frac{C_{L_{\alpha}} \text{ (Ref. 5)}}{f \text{ (Ref. 5)}} \frac{57.3}{\pi AR \text{ (Ref. 5)}}} \frac{E \text{ (Ref. 5)}}{E \text{ (Giromill)}}$$

The factor f is an empirical correction to account for real flow over an airfoil, and is a function of the taper ratio and aspect ratio.

Figures 12 through 16 define and present the various lift curve parameters plotted vs Reynolds number. Since the average test RN for the planned 80 RPM is 130,700, the values of the parameters at that RN were used to construct the curve shown in Figure 17 to predict the model performance using the Larsen cyclogiro vortex theory program.

No consistent trend for drag vs RN could be determined from the data of Reference 4 and 5. Reference 4 states that the drag data at RN less than 800,000 are unreliable. A value for C_{d_0} (C_d at $C_l = 0$) was obtained from Reference 7, Page 6-2. This was felt to be the most reliable source due to the large amount of data collected and the careful correlation of the data by the author. A blade C_{d_0} value of 0.018 was selected.

For the drag due to lift increment, $C_d - C_{d_0}$, data available from References 4 and 5 for RN in the neighborhood of 130,700 were plotted together to form a drag

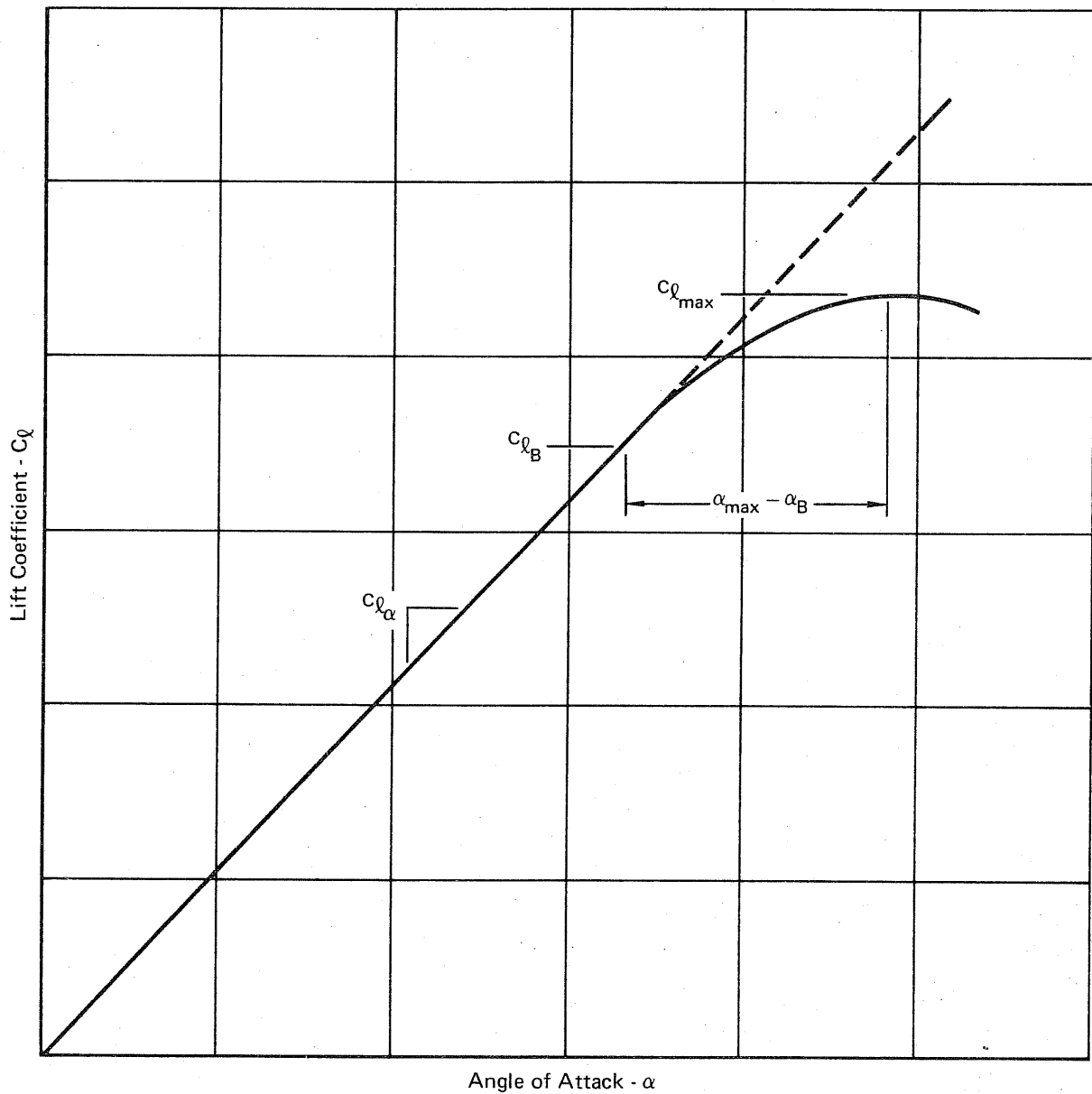


FIGURE 12
LIFT CURVE COMPONENT DEFINITIONS

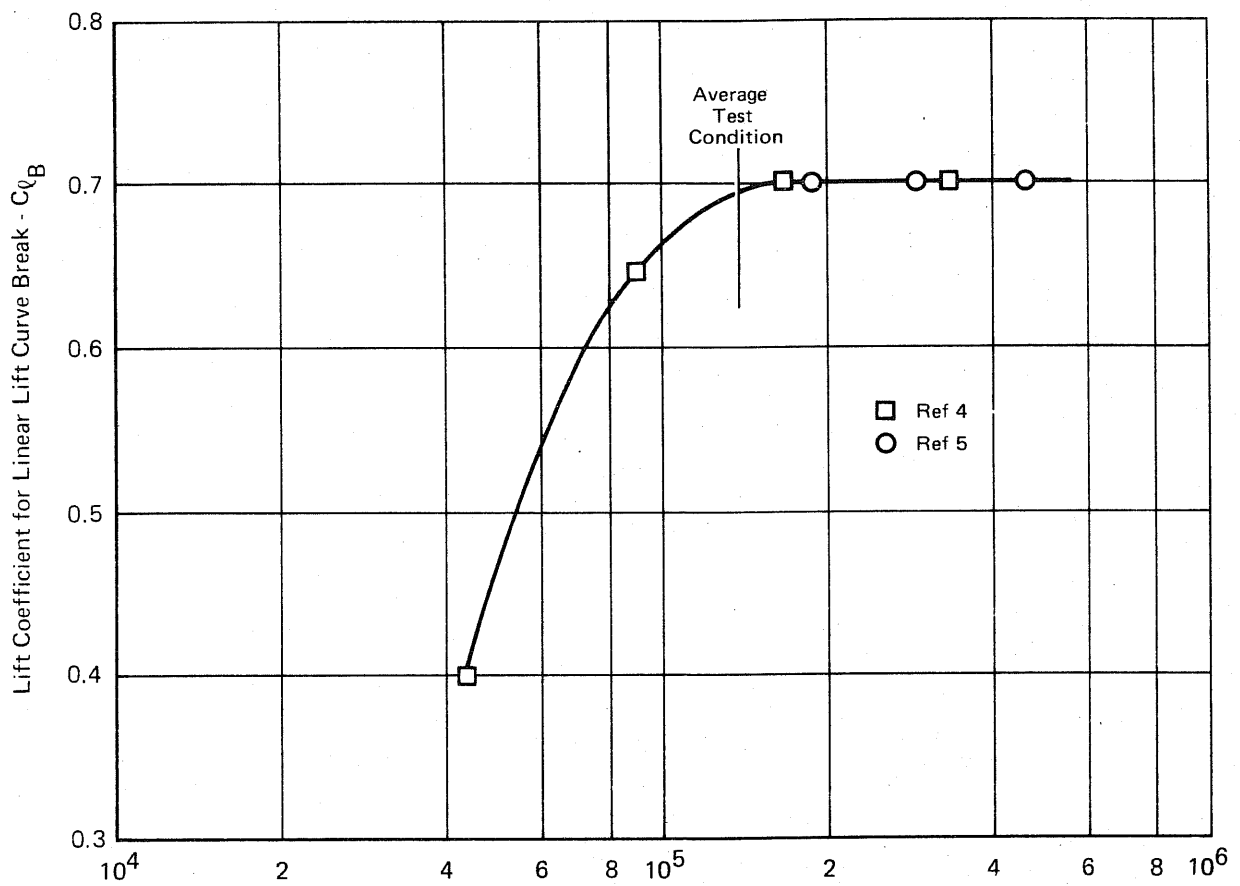


FIGURE 16
LIFT CURVE BREAK vs REYNOLDS NUMBER
 NACA 0015

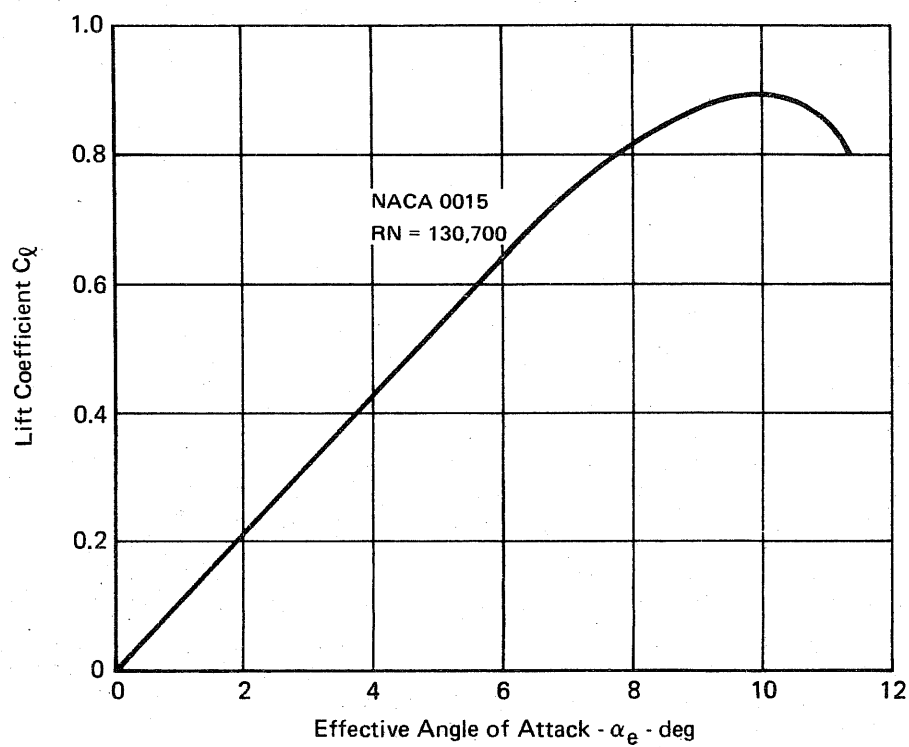


FIGURE 17
LIFT CURVE USED IN CYCLOGIRO VORTEX THEORY PROGRAM

envelope. From these data it was noted that C_d at $C_{l_{max}}$ was approximately 0.035 for all RN. The drag curve chosen for use in the Larsen cyclogiro vortex theory program was the highest drag coefficient shown in the drag envelope of Figure 18 but with $C_d - C_{d_0} = 0.035$ at $C_{l_{max}}$. The higher drag curve was chosen because it was felt that the Giromill blade may have a slightly higher than normal drag due to the RN variation experienced during a revolution. Any flow separation or boundary layer thickening occurring during the low RN portion of the revolution will at least partially carry over into the high RN portion. Since the high RN portion produces most of the torque, the carryover of low RN effects to the high RN region would be more significant than vice versa. The magnitude of this effect is unknown, so that the addition of an arbitrary drag increment could not be justified; however, a conservative approach to determining the drag at the average RN was felt to be warranted.

The Giromill test was planned so that continuous operation above the stall angle of attack is avoided. However, due to approximations in the blade modulation technique, described later, blade angles exceeded that predicted for stall momentarily at several points during the rotation. This occurred only for the highest nominal blade angle of attack tested, namely 9° . For this reason, drag above stall was of interest. Data from Reference 4 shown in Figure 19, indicates that drag tends to rapidly approach the value for zero leading edge suction; $C_d - C_{d_0} = C_L \tan \alpha$. The drag due to lift above stall used in the vortex theory program is shown in Figure 20. It was assumed that drag due to lift reached a value of $C_L \tan \alpha$ at two degrees above stall. The three dimensional data of Figure 19 reaches $C_L \tan \alpha$ at 3.3 degrees above stall. If this were corrected to the Giromill lift curve slope, the value would decrease to 2.5 degrees above stall. The additional half degree increment was subtracted to attempt to allow for 3 dimensional effects in the stall region that can not be accounted for in the vortex theory program.

In addition to the blade drag, the drag of the rotor arms must be accounted for. The drag coefficient, as utilized in the Larsen cyclogiro vortex theory program, is assumed to act at the blade. An equivalent drag coefficient, C_{de} , was determined which, when acting at the blade, would produce the same torque about the rotor shaft as the distributed drag along the arm. The relationship between C_{de} and the rotor arm drag coefficient was determined to be:

$$C_{de} \frac{(R) \left(\frac{1}{2} \rho V_B^2 S_B \right)}{\cos \alpha_w} = \int_0^{r_1} c_{d_1} \left(\frac{1}{2} \rho V_r^2 \right) c_{A_1} r dr + \dots$$

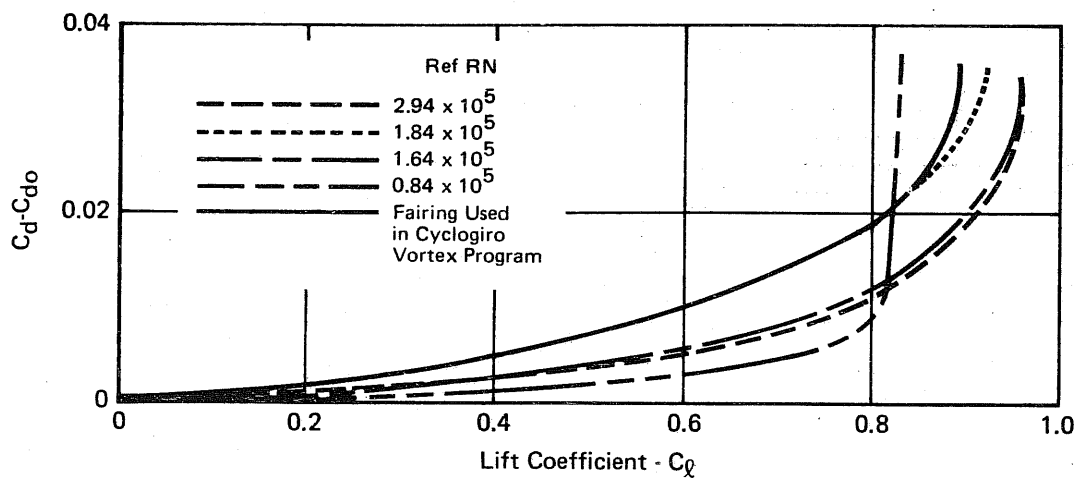


FIGURE 18
TWO DIMENSIONAL DRAG DUE TO LIFT
 NACA 0015

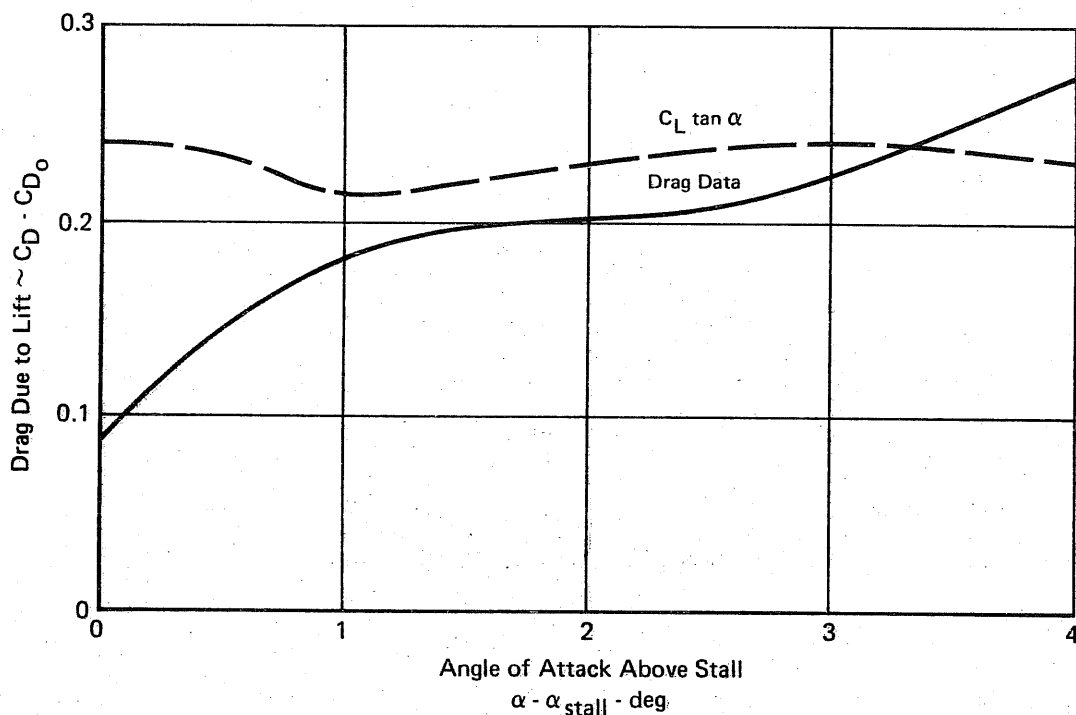


FIGURE 19
DRAG DUE TO LIFT ABOVE STALL
 Ref 4 Data RN = 1.89×10^5
 stall = 14.5° AR = 6.0

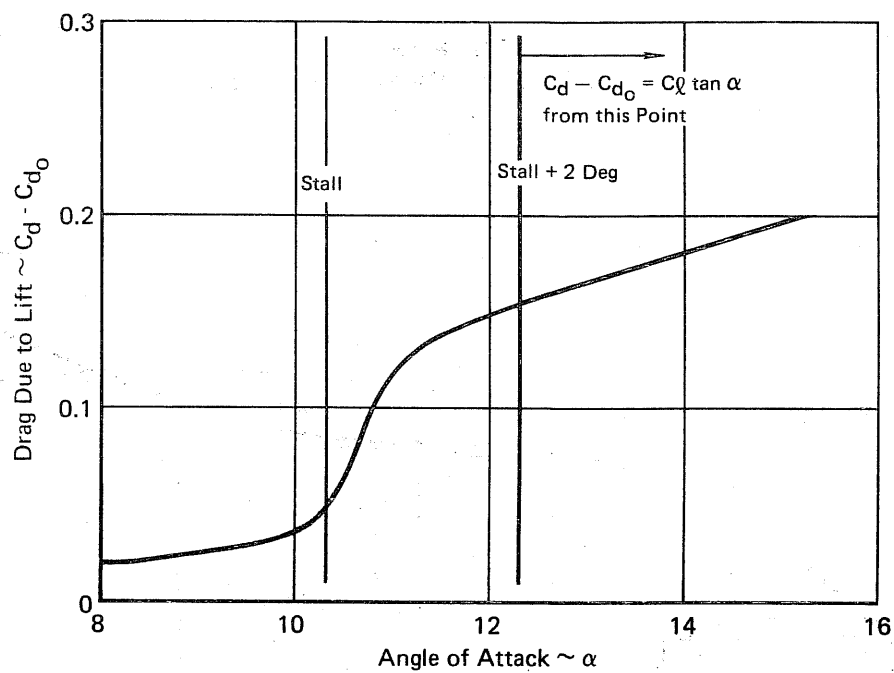


FIGURE 20
DRAG DUE TO LIFT ABOVE STALL
USED IN VORTEX THEORY PROGRAM

$$+ \int_{r_n}^R c_{d_n} \left(\frac{1}{2} \rho v_r^2 \right) c_{A_n} r dr \quad (1)$$

where

$r_1 \dots r_n$ = radii defining arm sections where c_d and c_A can be assumed constant and

R = rotor radius

ρ = air density

S_B = rotor blade area

$c_{A_1} \dots c_{A_n}$ = rotor arm chord for sections to be integrated

α_w = angle between relative wind and blade path tangent =

$$\tan^{-1} \frac{\cos \psi}{\lambda - \sin \psi}$$

V_B = blade velocity = $V_T \sqrt{\lambda^2 - 2\lambda \sin \psi + 1}$

V_r = arm velocity at r ; $V_T \left(\lambda \frac{r}{R} - \sin \psi \right)$

The $\cos \alpha_w$ term is to account for the fact that the orientation of the blade drag is not perpendicular to the arm, but is along the relative wind generated by the wind vector and the rotational velocity vector. Induced angle of attack due to the vorticity was not accounted for, but for arm drag purposes, this has a small effect.

The necessity for breaking the arm into multiple parts is due to the restriction that velocity must not change sign along each arm section to be integrated and the c_A and C_{dA} (component drag coefficient based on its reference area S_A) must be a continuous function of r or constant in value.

For an arm of constant chord, C_{dA} , and shape, such as the Giromill upper rotor arm, solution of the above equation yields the result that for large blade speed ratios

$$C_{de} = 0.25 C_{dA} \frac{S_A}{S_B} \quad (2)$$

For low blade speed ratios, C_{de} is a strong function of ψ . Figure 21 shows that for $\lambda = 1.3$ (the lowest λ to be tested), C_{de} becomes negative on the downwind portion of the revolution. Since no provision exists in the Larsen cyclogiro vortex theory program for variations in C_d with ψ , it was necessary to choose a single representative value. Figure 22 shows comparisons of drag of the upper rotor arm ($C_{de} \frac{1}{2} \rho V_B^2 S_B$) as a function of ψ obtained by using Equation (2) with that ob-

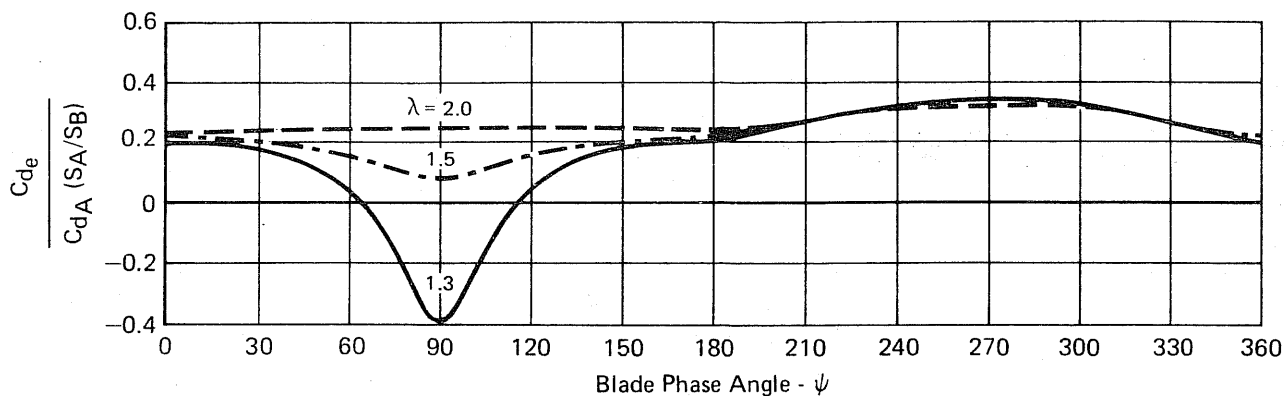


FIGURE 21
VARIATION OF EFFECTIVE ARM DRAG COEFFICIENT WITH BLADE SPEED RATIO AND PHASE ANGLE

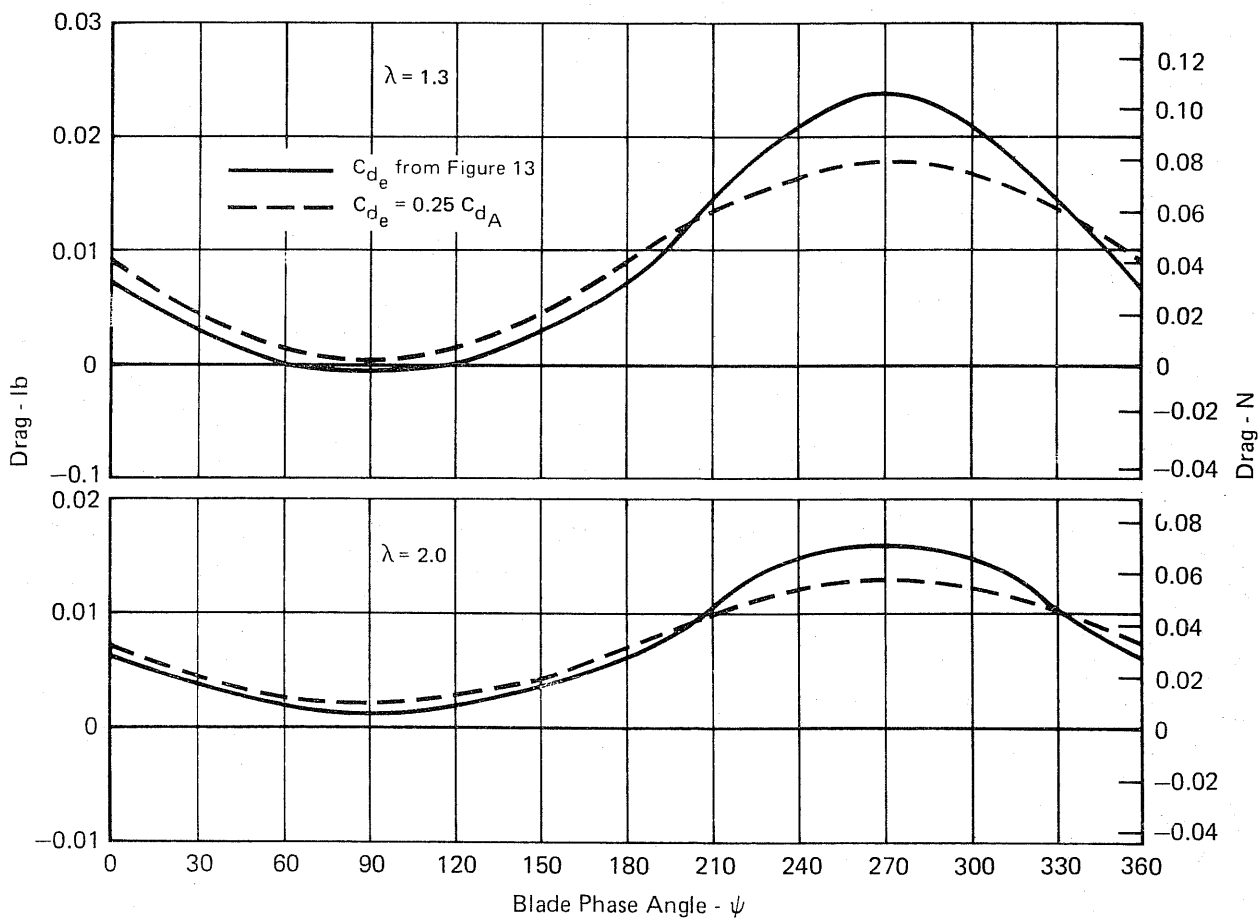


FIGURE 22
DRAG COMPARISON - UPPER ARM

tained by using the Equation (1) C_{d_e} variation with ψ and λ shown in Figure 21. Relatively good agreement is obtained even at $\lambda = 1.3$ due to the fact that the region of largest disagreement in C_{d_e} is also the region of lowest dynamic pressure.

The results in Figure 22 show that the approximation for very large blade speed ratios is actually acceptable, for practical purposes, down to $\lambda = 1.3$. Therefore, the following approximate solutions to Equation (1) were used to calculate arm drag.

For a constant chord, constant drag coefficient arm, such as the upper rotor arm, Equation (2) is used directly. For cases where the arm does not extend out to the blade radius, R , or where the chord or drag coefficient is not constant, the arm can be divided into n segments of constant chord, constant drag coefficient. The effective drag coefficient of any segment with an area S_{A_n} is calculated by:

$$C_{d_{e_n}} = \frac{\frac{S_{A_n}}{S_B} C_{d_{A_n}}}{R^3 (r_2 - r_1)} \left[\frac{r_2^4}{4} - \frac{r_1^4}{4} \right] \quad (3)$$

where $C_{d_{A_n}}$ is the component drag coefficient and S_{A_n} its reference area for the n th arm section, r_1 is the inboard limit of this section and r_2 is the outboard limit. Equation (3) is obtained from Equation (1) using the large blade speed ratio approximation and integrating between arm limits r_1 and r_2 .

The Reynolds number used for the arms was that existing at $0.84R$. This point divides the arm drag; half of the effective arm drag occurs outboard of this point, and half inboard (assumes a constant C_{d_A} and high λ). This $0.84R$ arm radius point is obtained by forming the ratio of $C_{d_{e_n}}$ (Equation (3)) with $r_1 = 0$, to C_{d_e} (Equation (2)), and setting equal to 0.5. This is then solved for r_2 noting that $S_{A_n}/S_A = r_2/R$.

The drag coefficients, C_{d_A} , and corresponding reference areas for the rotor arms, guy wires, and a small protuberance of the blade shaft and bellcranks, are presented in Figure 23.

The component effective drag coefficients referenced to the blade area (3.5 sq ft. or 0.325 sq. meters) and including the blade and an estimated blade to arm interference drag are presented in Figure 24. This is the zero lift drag coefficient that was used in conjunction with the drag due to lift, shown in Figure 18 in the cyclogiro vortex theory program to compute the Giromill wind tunnel model performance.

3.2 Wind Tunnel Model Performance Predictions

The Giromill model performance, power coefficient versus blade speed ratio, calculated using the Larsen cyclogiro vortex theory program is shown in Figure 25

	Ref Area		
	C_{dA}	m^2	Ft^2
Upper Arm (NACA 0015 Airfoil Section)	0.045	0.0813	0.8750
Lower Arm			
4 in. Chord Blade (NACA 0015 Airfoil Section)	0.045	0.1006	1.0830
Flared Tip	0.014	0.0235	0.2530
Guy Wire	1.000	0.0014	0.0150
Blade Shaft and Bellcrank	1.000	0.0002	0.0022

**FIGURE 23
COMPONENT DRAG COEFFICIENTS**

	C_{de}
Upper Arm	0.0028
Lower Arm	0.0038
Guy Wires	0.0008
Blade Actuator	0.0005
Blade	0.0180
Interference	0.0002
Total:	0.0261

**FIGURE 24
ZERO LIFT EQUIVALENT DRAG COEFFICIENTS**

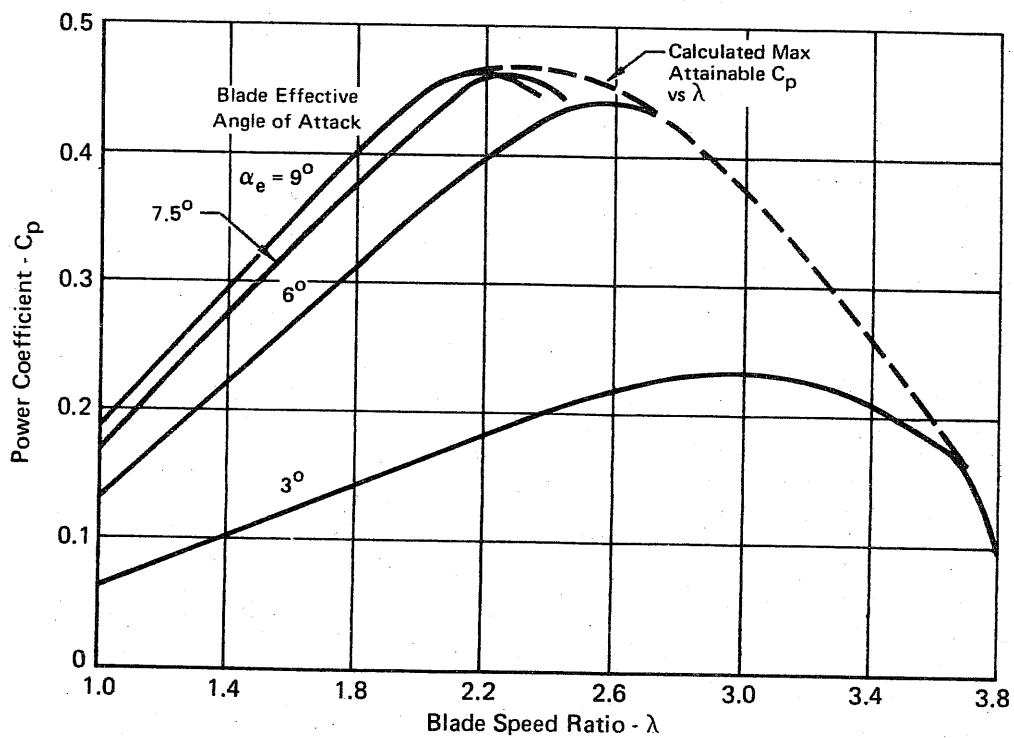


FIGURE 25
GIROMILL MODEL PERFORMANCE ESTIMATES FROM VORTEX THEORY PROGRAM
 Vortex Theory Program Computed Rock Angles

This figure shows that at a given angle of attack C_p decreases fairly rapidly for the blade speed ratios above that for $C_{p_{max}}$. The results of the wind tunnel test indicate that this rapid decrease may be due to limitations in the cyclogiro vortex theory. As described in Reference 1 the program does not converge to a solution for blade speed ratios much beyond that for $C_{p_{max}}$ at a given angle of attack. The performance shown in Figure 25 is based on a blade rock angle modulation which precisely maintains the desired angle of attack in the presence of varying relative wind angles and blade flow field induced angle of attack variations as the blade rotates through the angle ψ .

In order to ensure a smooth cam surface for controlling the wind tunnel model blade rock angle, the rock angles calculated by the cyclogiro vortex theory program were approximated by a Fourier type series of the form;

$$\theta_R = \theta_o + \sum_{n=1}^5 a_n \sin(n\psi) + b_n \cos(n\psi)$$

Figure 26 shows a typical comparison between the cyclogiro computer program rock angles and the series smoothed rock angles. When the smoothed rock angles are used in the cyclogiro program, the power coefficient variation with blade speed ratio shown in Figure 27 is the result. Comparison with Figure 25 shows the following: (1) no change for 3° nominal angle of attack, (2) a slight reduction in peak power ($-.005 \Delta C_p$) for the 6° angle of attack, (3) a small reduction in C_p for the 7.5 degree angle of attack which increases with λ ($\Delta C_p = -.012$ at $\lambda = 2.25$), and (4) a large decrease in C_p for 9° nominal angle of attack, especially at peak C_p .

The large decrease predicted for the 9° nominal angle of attack configurations is due to the fact that blade stall was predicted to occur at 10°. The smoothed rock angles caused the angle of attack to range between a low of about 6° and a high of about 12°. The high drag and lower lift associated with post stall angles of attack produces the drop in predicted performance.

The vortex theory program does not include the effects of blade rotation rate on the aerodynamic characteristics. As the blade travels along its circular path it has a rotation rate, q , which is the sum of the rotor rotation rate ω and the blade's rotation rate with respect to the rotor, $\dot{\theta}$ (see Figure 28).

$$q = \omega + \dot{\theta}$$

The average $\dot{\theta}$ for any complete rotor revolution is zero since the blade returns to the same position. A first order approximation is that the pitch rate of the blade is given by

$$q = \omega$$

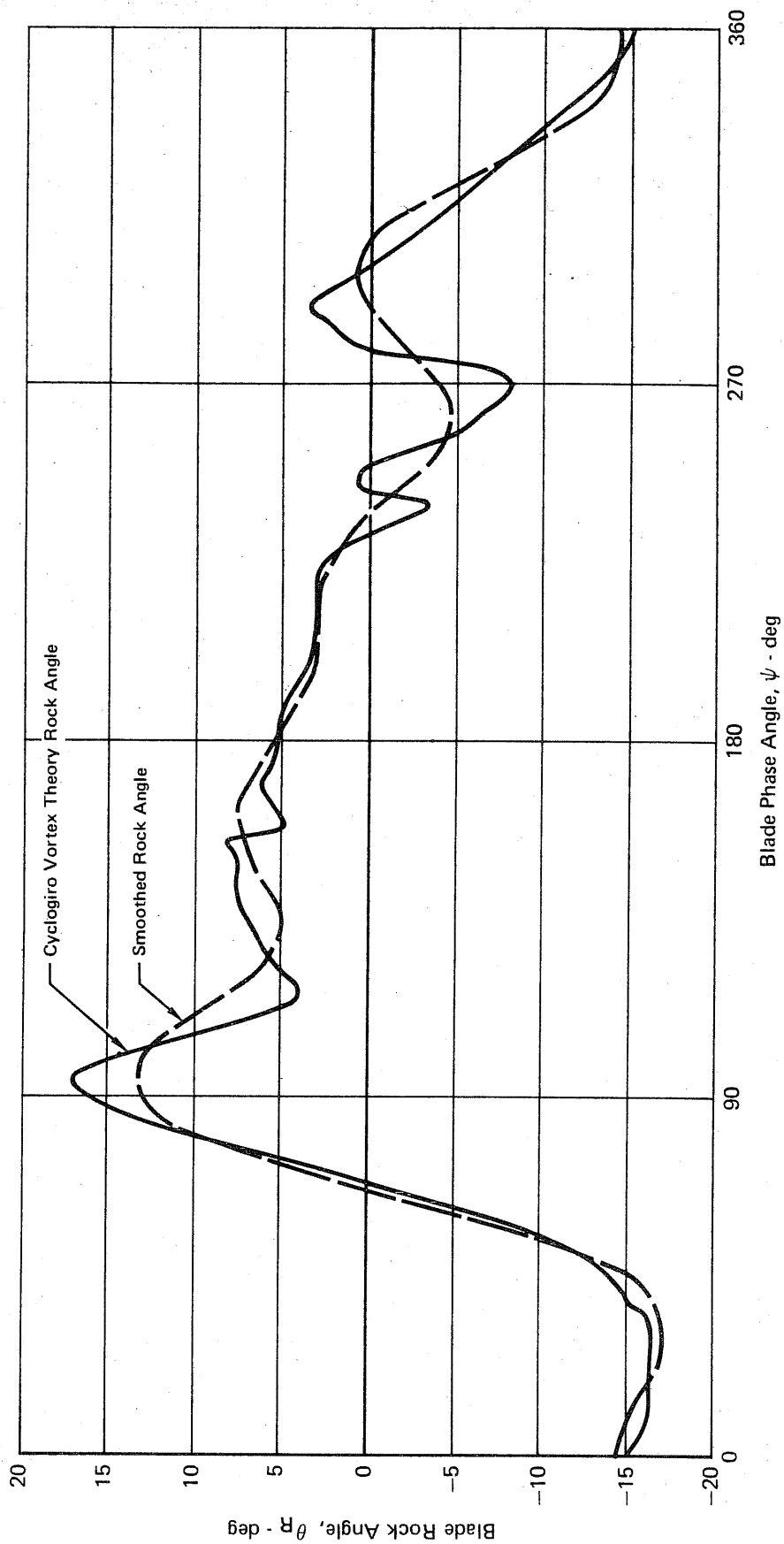


FIGURE 26
BLADE ROCK ANGLE COMPARISON

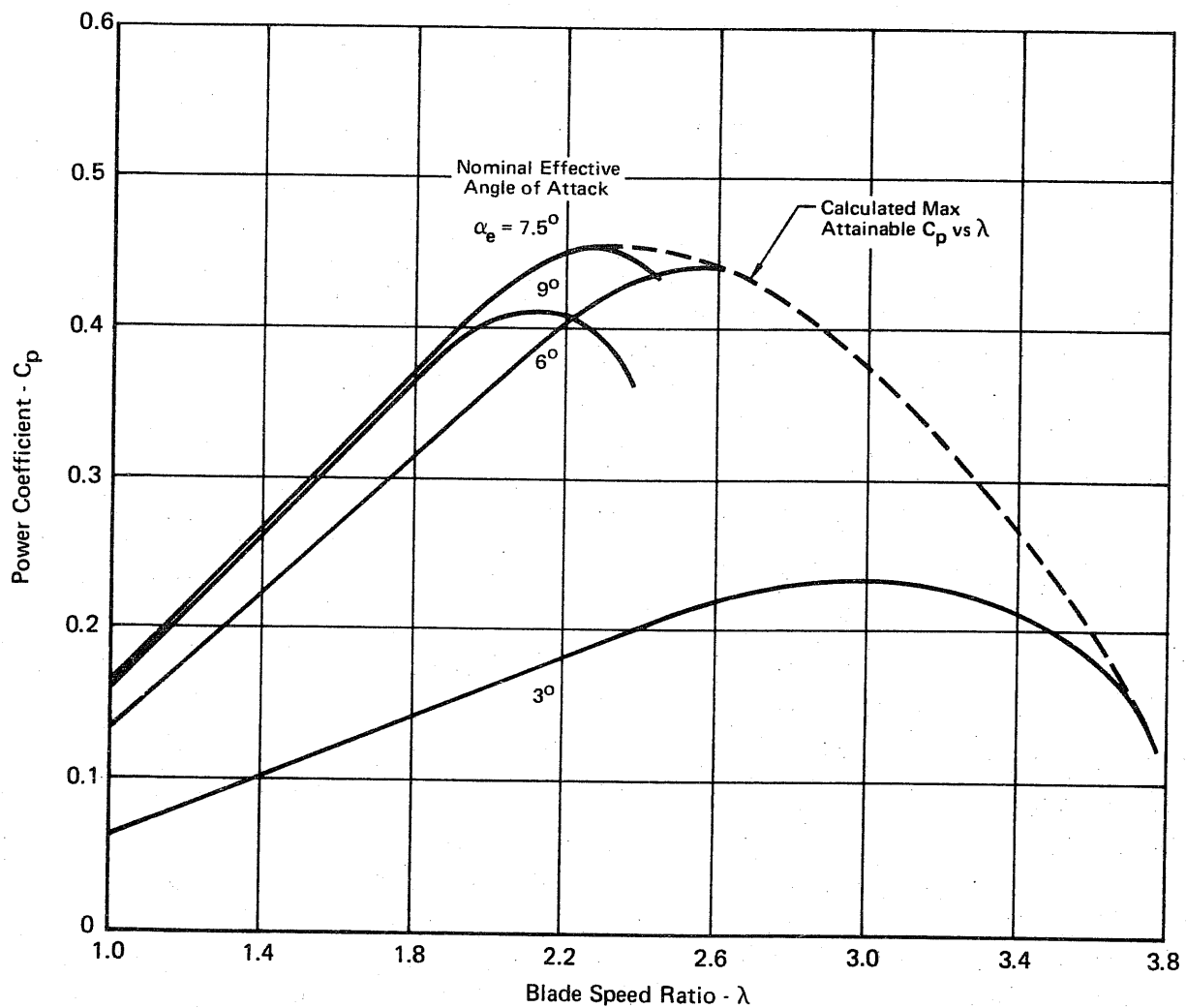


FIGURE 27
GIROMILL MODEL PERFORMANCE ESTIMATES
FROM VORTEX THEORY PROGRAM
 Series Smoothed Rock Angles

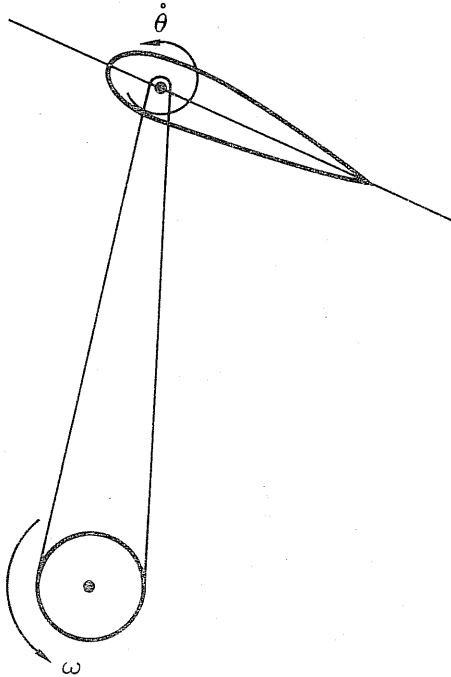


FIGURE 28
GIROMILL BLADE ROTATION

This blade pitching causes an induced camber effect shown in Figure 29. The change in lift and pitching moment due to this blade rotation can be accounted for in the linear, unstalled range by including the aerodynamic derivatives C_{mq} and C_{Lq} , defined as $C_{mq} = \frac{\partial C_m}{\partial (qc/2V_B)}$ and $C_{Lq} = \frac{\partial C_L}{\partial (qc/2V_B)}$.

The effects of C_{mq} and C_{Lq} on power coefficient are related to a blade moment which must be reacted by the rotor.

The moment M due to C_{mq} can be expressed as

$$M = C_{mq} \frac{qc}{2V_B} \frac{1}{2} \rho V_B^2 c S_B N \quad (4)$$

approximate V_B by $V_B = \omega R = \lambda V_W$ and q by $q = \omega$ so that

$$M = \frac{C_{mq} c^2 S_B \frac{1}{2} \rho \lambda^2 V_W^2 N}{2R}$$

since

$$\Delta C_p = \frac{M\omega}{\frac{1}{2} \rho A V_W^3} \quad \text{and} \quad \sigma = \frac{S_B N}{A} = \frac{cN}{2R}$$

$$\Delta C_p = \frac{2 C_{mq} \lambda^3 \sigma^3}{N^2} \quad (5)$$

The direct effect of C_{Lq} is negligible since the lift increase on the upwind side of the orbit is nearly cancelled out by the decrease in lift on the down wind side. However, C_{Lq} also effects the induced drag.

$$\frac{\partial C_D}{\partial \left(\frac{qc}{2V_B}\right)} = \frac{\partial}{\partial \left(\frac{qc}{2V_B}\right)} \frac{1}{\pi A e} (C_{LSTATIC} + C_{Lq} \frac{qc}{2V_B})^2$$

$$C_{Dq} = \frac{2 C_{Lq}}{\pi A e} (C_{LSTATIC} + C_{Lq} \frac{qc}{2V_B})$$

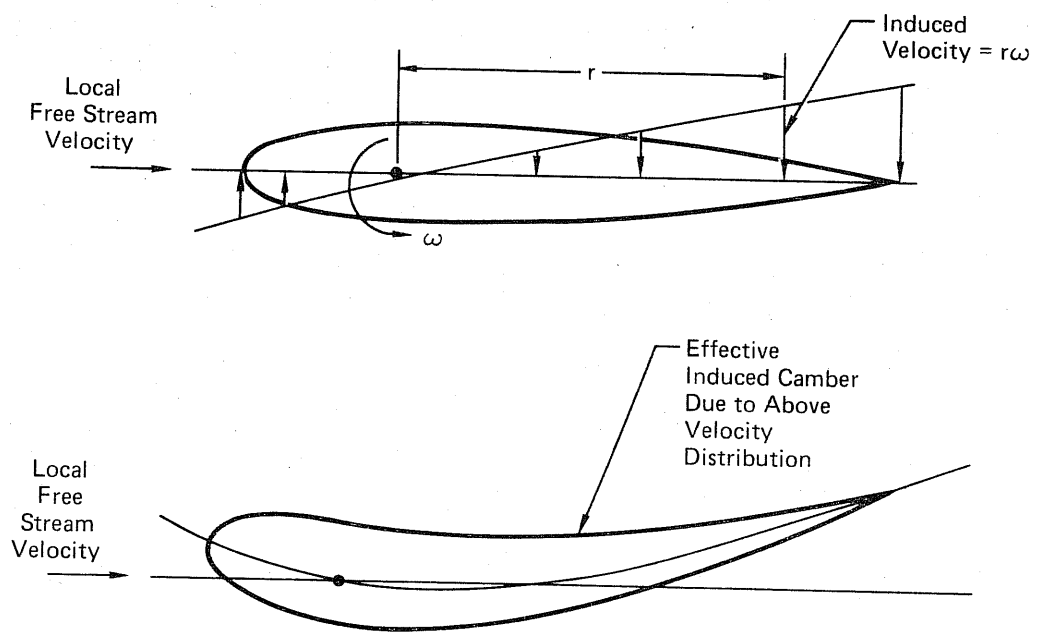


FIGURE 29
INDUCED CAMBER EFFECT

The moment due to C_{Dq} is

$$M = \frac{-2 C_{Lq}}{\pi A e} (C_{LSTATIC} + C_{Lq} \frac{qc}{2V_B}) \frac{qc}{2V_B} \frac{1}{2} \rho V_B^2 S N R \quad (6)$$

using the same method as above

$$\Delta C_p = \frac{-2 C_{Lq}}{\pi A e N^2} (N C_{LSTATIC} + C_{Lq} \sigma) \lambda^3 \sigma^2 \quad (7)$$

However, for the Giromill, $C_{Lstatic}$ is negative on the upwind side of the orbit and positive on the downwind side. Summing ΔC_p for the upwind side and the downwind side gives

$$\Delta C_p = \frac{-2 C_{Lq}^2 \lambda^3 \sigma^3}{\pi A e N^2}$$

Combining the effects of C_{mq} and C_{lq} gives

$$\Delta C_p = \frac{-2}{N^2} \left(\frac{C_{Lq}}{\pi A e} - C_{mq} \right) \lambda^3 \sigma^3 \quad (8)$$

For a non swept, non tapered airfoil (Reference 8)

$$C_{Lq} = -3.0$$

$$C_{mq} = -.53$$

The Giromill model blades had an aspect ratio of 7.14 and an e of .97. Solidity, σ , was .300.

$$\Delta C_p = -.00566 \lambda^3$$

For $\lambda = 2.17$, peak power;

$$\Delta C_p = -.058$$

A typical full scale Giromill could be expected to have $\sigma = .12$, λ for peak power = 3.1 and a blade aspect ratio of 12. With such a configuration, ΔC_p at peak power would be .009, which is much less than for the wind tunnel model.

The relationships derived above were verified by the more precise method of applying the effects of C_{Lq} and C_{mq} at 10° increments of ψ using the actual blade velocity including wind and induced effects and the actual blade rotation rates $q = \omega + \dot{\theta}$ obtained from the vortex theory program. The simplified relationships proved extremely accurate for $\lambda = 2.17, 1.85$, and 1.3 . The negligible effect of C_{Lq} on lift induced ΔC_p was also verified. The simplified relationships become more valid as λ increases so the accuracy at these low λ 's is gratifying.

When the above corrections are applied to Figures 25 and 27, the final predicted performance curves result. These are given in Figures 30 and 31.

The Darrieus mode performance prediction is shown in Figure 32. Since the Giromill vortex theory program cannot be used for the Darrieus mode, the predictions were obtained from Robert E. Wilson of Oregon State University using our lift and drag data in the Wilson and Lissaman multiple stream tube approach. (See Reference 9). This method does not account for blade moment effects, but he suggested that they could be significant for our model. This provided the incentive for deriving the rotation rate corrections previously described. These corrections were applied to his predictions to obtain the data in Figure 32. For the Darrieus mode, which experiences blade stall through a significant portion of its operating range, stalled blade pitching moment may also be significant, according to Wilson, but this effect was not accounted for.

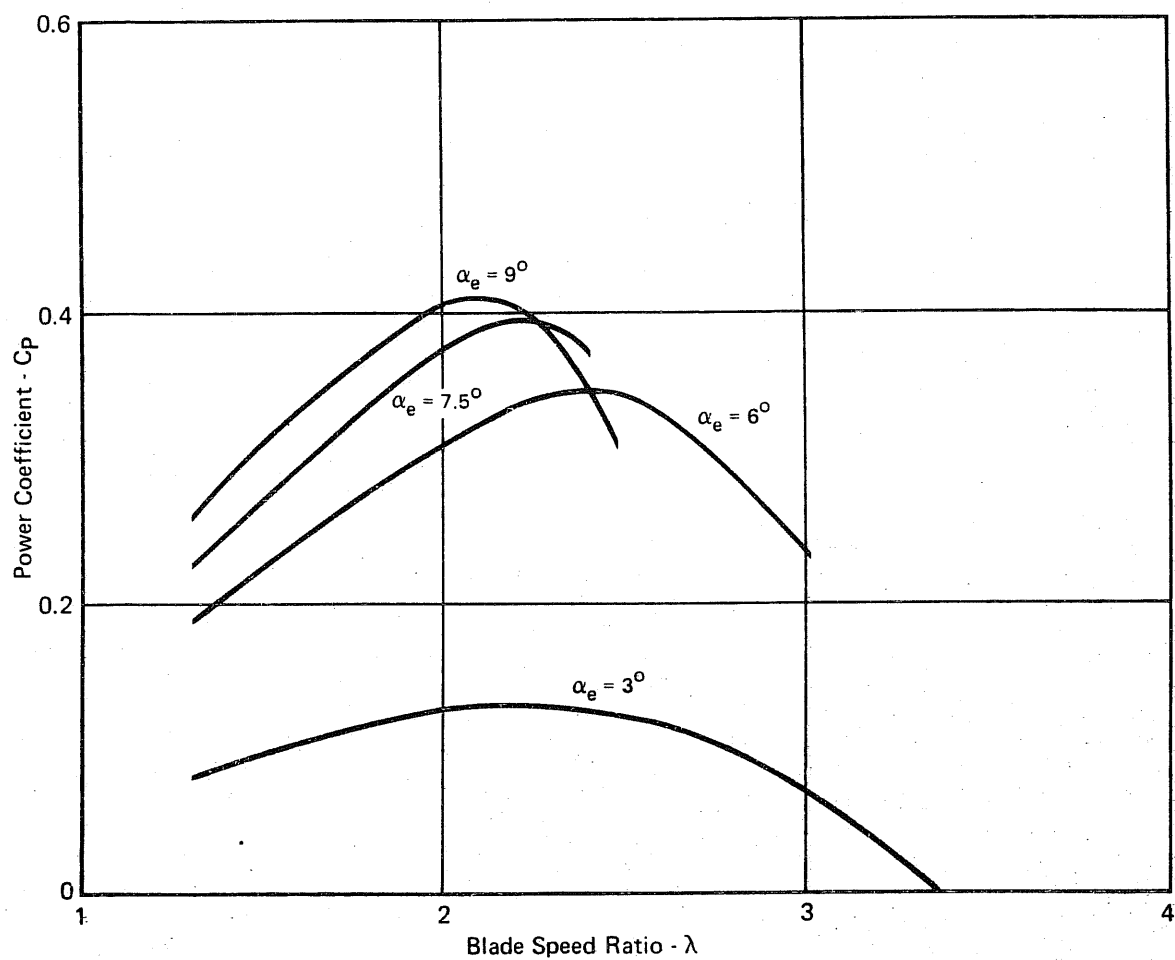
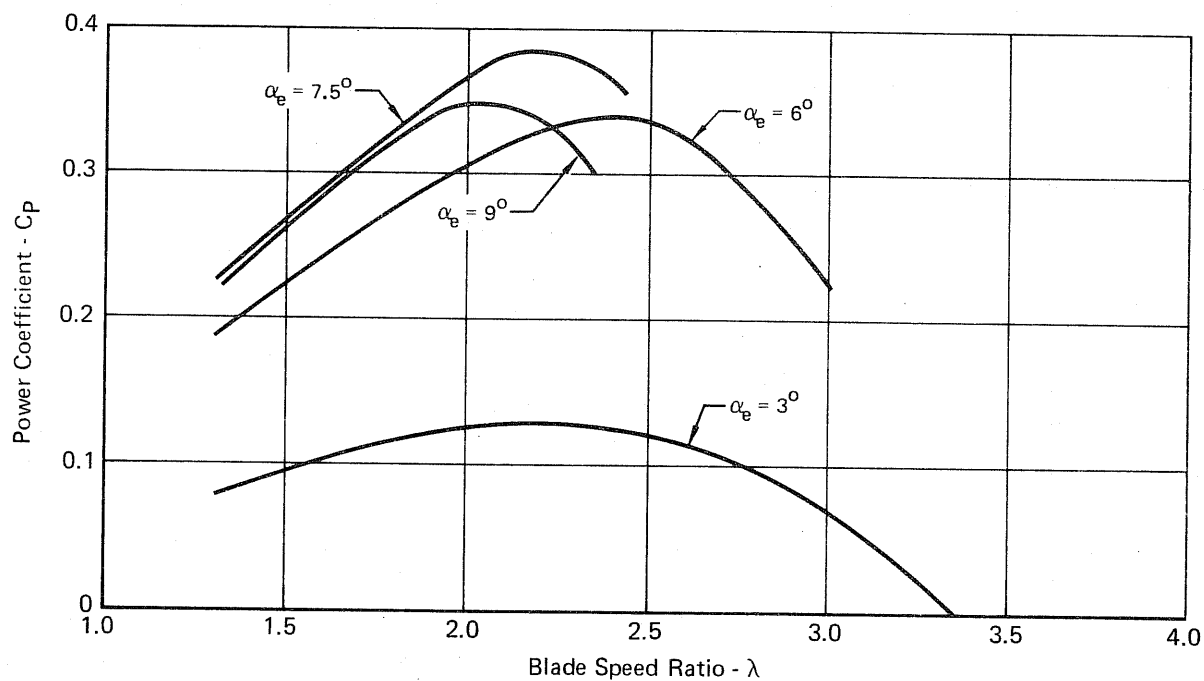


FIGURE 30
GIROMILL MODEL PERFORMANCE ESTIMATES INCLUDING
BLADE ROTATION RATE EFFECTS
 Vortex Theory Program Computed Rack Angles



GP77-0810-18

FIGURE 31
GIROMILL MODEL PERFORMANCE ESTIMATES
INCLUDING BLADE ROTATION RATE EFFECTS
 Smoothed Rack Angles

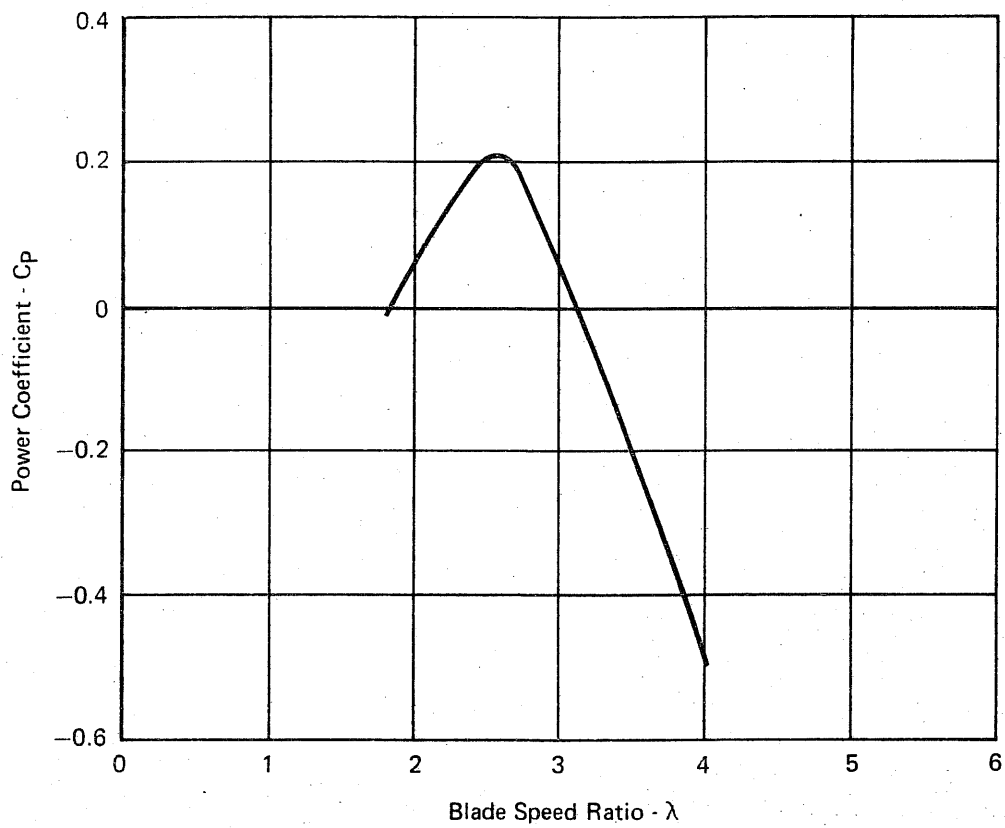


FIGURE 32
PREDICTED DARRIEUS MODE PERFORMANCE
INCLUDING ROTATION RATE EFFECTS

7. WIND TUNNEL TEST

The test conditions were defined to cover the operating range of the Giro-mill to the extent possible within the limitations of the wind tunnel and model. Blade speed ratios from 1.3 to 3.8 were tested with nominal blade angles of attack ranging from 3° to 9° . Blade speed ratios of less than 1.3 could not be tested due to the fact that the large blade rock angles required for low λ 's could not be mechanized using the cam and push rod method. Blade speed ratios above 3.8 result in tunnel velocities and torques which are approaching values too low for accurate performance measurements at the 80 to 100 RPM range tested.

For the Darrieus mode, blade speed ratios ranging from 1.8 to 8.5 were tested. A rotational velocity of 120 RPM was used for this mode in order to keep the velocity and torques high enough for acceptable accuracy.

Figure 33 shows the run schedule followed during the test. The arrangement is according to test conditions rather than chronological.

Group 1 of Figure 33 was the peak power cam, designed for $\alpha_e = 9^\circ$ and $\lambda = 2.17$. The flip axis angle, β , was -80° (see Figure 11). All Giromill cams except those for Group 3 were designed to have $\beta = -80^\circ$.

The induced angles of attack calculated by the program are strongly influenced by the vortex distribution, and this distribution is based on greatly simplified approximations (see Reference 1). The Group 2 configuration were therefore designed to explore the effect of changes in the assumed induced α . Assumed α_i values 1.25 and .75 times the nominal were used in designing the cams for Group 2. This resulted in a maximum of 3° change in blade angle from the nominal occurring at about $\psi = 160^\circ$.

Group 3 used a blade flip axes angle, β of -100° . The vortex theory program predicted an insignificant change in C_p and this cam was designed to verify that prediction.

Group 4 runs are the $\alpha_e = 9^\circ$ configurations at various λ 's. Cams 5, 6, and 8 were designed using Fourier series curve fits of the rock angles obtained directly from the vortex theory program.

Cam 9 ($\lambda = 3.0$) was designed by plotting the Fourier series coefficients for cams 5, 6 and 8 vs. λ and extrapolating to $\lambda = 3.0$. This was done because the vortex theory program could not be used at this high λ due to convergence problems as explained in Reference 1. Since the induced α computation at high λ 's was suspect, an alternate method was used to design cam 10 for $\lambda = 3.0$. This was accomplished by using the rock angles computed by the program for $\lambda = 2.27$ and interpolating between these and $\theta_R = 0$ (Darrieus) at $\lambda = 4.0$. This was done since preliminary computations had indicated that the Darrieus mode peak power coefficient would occur near $\lambda = 4.0$.

Group No.	Run No.	Cam No.	Design Values for			Nominal rpm	Comments
			α_e	β	λ		
1	8	1	9.0	-80	2.17	80	This is the Peak Power Condition
	20					100	
	38					100	
2	9	2	9.0	-80	2.17	80	Cam Designed by Assuming Induced α 's are 0.75 those Calculated by Theory
	10	3				80	Cam Designed by Assuming Induced α 's are 1.25 those Calculated by Theory
3	11	4	9.0	-100	2.17	80	
	12					100	
4	31	5	9.0	-80	1.30	100	
	7	6	9.0	-80	1.85	80	
	28					100	
	13	8	9.0	-80	2.40	100	
	14	9	9.0	-80	3.00	100	Cam Determined by Extrapolating Fourier Series Coefficients that Determined Cams 5 through 8
	39					100	
	15	10	9.0	-80	3.00	100	Cam Determined by Interpolating Between a Cam for $\lambda = 2.27$ and a Darrieus (Circular) Cam at $\lambda = 4.0$
5	19	20	7.5	-80	1.30	100	
	16	7	7.5	-80	2.17	100	
6	30	11	6.0	-80	1.30	100	
	17	12	6.0	-80	1.85	100	
	40						
	19	13	6.0	-80	2.50	100	
	21	14	6.0	-80	2.63	100	
	22	15	6.0	-80	2.90	100	Cam Determined by Fourier Series Coefficient Extrapolation
7	32	16	3.0	-80	1.30	100	
	18	17	3.0	-80	1.85	100	
	23	18	3.0	-80	2.85	100	
	24	19	3.0	-80	3.57	100	

FIGURE 33
GIROMILL TEST RECORD

Group No.	Run No.	Cam No.	Design Values for			Nominal rpm	Comments
			α_e	β	λ		
8	37	21	Sinusoidal Modulation Simulating $\alpha_e = 9^\circ$ $\beta = -80^\circ$ $\lambda = 2.17$			100	
9	25	22	Darrieus			120	$\lambda = 3.5$ to 6.8
	26						$\lambda = 2.3$ and 5.9
	27						$\lambda = 1.8$ to 3.0
10	33	23	Modified Darrieus $\pm 3^\circ$ Rock Angle			120	$\lambda = 2.0$ and 2.5
	36						$\lambda = 3.7$ to 7.5
	34	24	Modified Darrieus $\mp 3^\circ$ Rock Angle				$\lambda = 2.0$ to 2.5
	35						$\lambda = 3.6$ to 7.1
11	41	12	6.0	-80	1.85	100	Performance Effect of Vertical Support Struts
	42	14	6.0	-80	2.63		

FIGURE 33 (Continued)
GIROMILL TEST RECORD

Group 5 through 7 were to explore α_e variations. Group 8 used a sinusoidal blade modulation in which a blade modulation equation, given below, was used.

$$\theta_R = \theta_{R_0} + a \sin(\psi + b)$$

Values for θ_{R_0} , a and b were determined by a least squares curve fit program which gave the closest fit to the $\alpha_e = 9$, $\lambda = 2.17$ blade modulation.

Group 9 was the Darrieus mode and Group 10 was denoted "Modified Darrieus". The Group 10 configurations were to explore the value of small blade modulations in improving the Darrieus mode performance. Cam 23 (denoted as \pm flip) flipped the blade $+3^\circ$ (nose inward) on the upwind side (ψ from 270° to 90°) and -3° on the downwind (ψ from 90° to 270°). A 30 degree transition region about the $\psi = 90^\circ$ and 270° points was used for flipping. Cam 24 used opposite flip angles (and is denoted as $\bar{\pm}$ flip) from cam 23.

Group 11 consisted of the addition of dummy vertical support struts (see Figure 3). These were added in order to determine the effect on performance that this type of support may have.

7.1 Torque Meter Calibration and Tare Runs

The torque motor was calibrated by the MCAIR calibration laboratory and was found to be repeatable within \pm one inch pound up to 200 inch pounds of torque. Two check loadings were conducted by the wind tunnel personnel. One just prior to the test and one near the end of the test, just after run 39. Figure 34 shows the check loading data points and the calibration curve (3 read-out-counts per in. lb.).

The worst check loading disagreement is 10%. The method of applying the check loads (weights and pulleys, since the installed axis of rotation is vertical) probably accounts for most of the disagreement.

In order to be able to separate the torque required to overcome system friction from the aerodynamic torque, a series of tare runs were conducted.

Torque data were collected in the RPM range of 80 to 120 with the blades off at zero air speed. This was done with no cam, cam 22 (circular) and cam 6. Cam 22 was used for Darrieus and 3° blade flip Darrieus tares and cam 6 was selected as being representative of the Giromill cams. Since arm drag effects were in the tare data, the calculated arm drag values vs RPM were subtracted from the tare data to obtain the values for cam and bearing friction torque used in computing the aerodynamic performance.

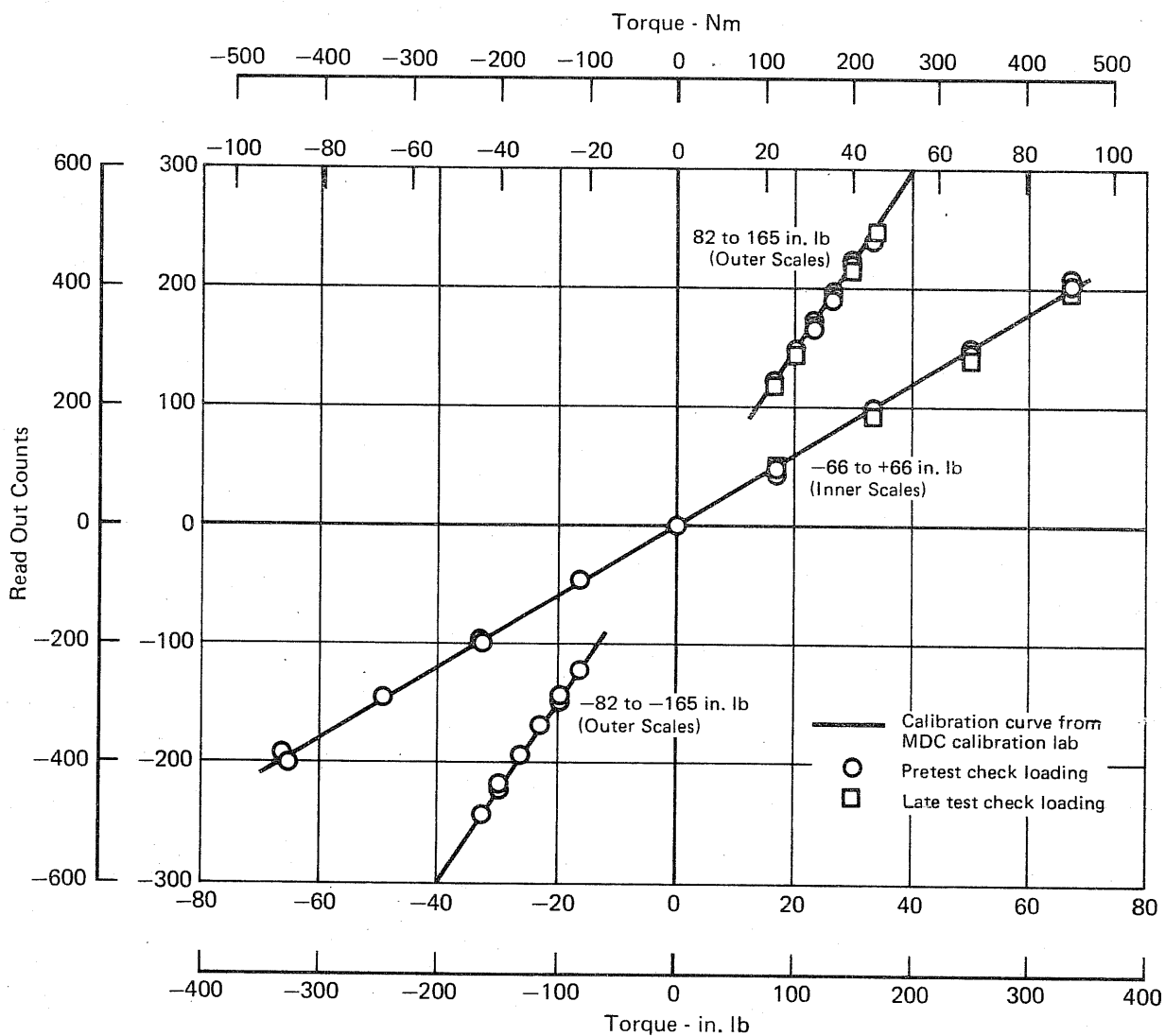


FIGURE 34
COMPARISON BETWEEN TORQUE METER CHECK LOADINGS
AND CALIBRATION CURVE

7.2 Performance Runs

The Giromill performance runs were originally planned for 80 RPM in order to minimize the possibility of structural problems. Tare runs and performance runs at 100 RPM, however, indicated no problems. In the interest of greater data accuracy through higher torques and higher tunnel velocity, this RPM range was used for all Giromill runs after run 11.

Some minor difficulties were experienced with the torque meter zero setting during the test. Occasional wind blowing into the test section and eccentric loadings transmitted by the push rods spring at certain cam positions made it difficult to determine when the torque meter was truly unloaded. This could be compensated for to a great extent by slowly rotating the Giromill until a consistent average zero reading was obtained. However, this technique was not employed in the first half of the test. An indication of the magnitude of the possible zero shift was obtained by comparing zero readings obtained before and after each run. Analysis revealed an RMS difference of 4 in. lb. This is undoubtedly high since the post run zero return values were generally obtained without rotating the model to obtain a consistent average zero reading.

As described in Section 4, concern over possible inaccuracies of the wind tunnel pitot-static airspeed measurement system prompted the addition of a Thermo Systems Inc. hot film anemometer. During the test, an 11% average discrepancy existed between the tunnel pitot-static (V_T) system and the hot film probe output (V_P); the V_T system indicating a higher velocity than V_P . Due to the unexpectedly large magnitude of the discrepancy it was decided to use the V_T system as the standard during the test and to concurrently investigate the hot film system for possible errors. None were found. At the completion of the test, a velocity comparison calibration run was made by installing a Kollsman pitot tube 1 ft. below the hot film probe. The measured velocities of both probes showed good agreement throughout the test velocity range lending credence to the accuracy of the hot film anemometer. A subsequent tunnel velocity survey was conducted as part of another study in June 1977 to relate the velocity measured at the hot film anemometer probe position used during the Giromill test with the velocity in the test section. Both a hot film and Kollsman probe were used. Figure 35 shows the location of the test section velocity survey points with reference to the wind tunnel Giromill model cross section. The measured test section survey velocities agreed well with the measured velocity obtained at the Giromill test hot film anemometer probe position, V_P ; however, the test section survey velocities also agreed well with the pitot static

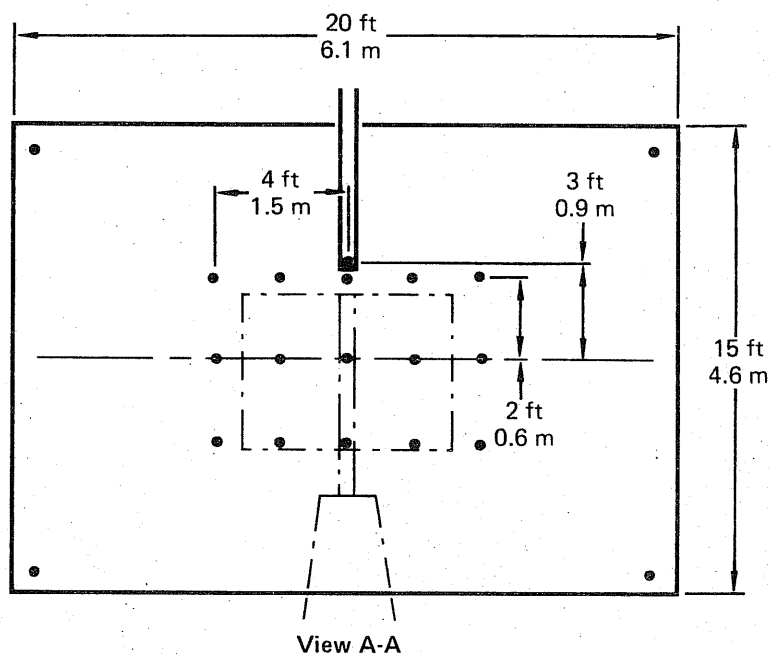
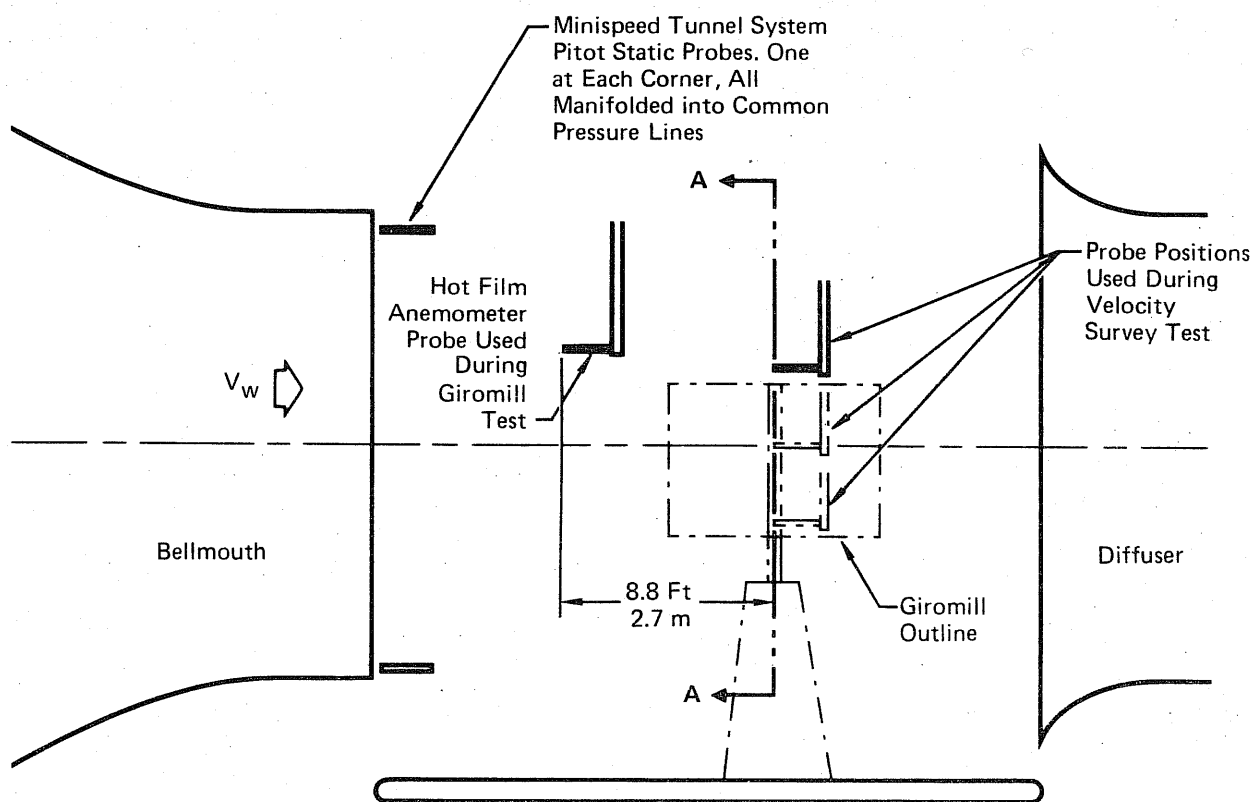


FIGURE 35
PROBE POSITION DIAGRAM

tunnel system velocity V_T . This created a dilemma as to what velocity, V_P or V_T , should be used for data reduction. Ramifications of this are discussed in the next section.

8. TEST RESULTS AND ANALYSIS

Figure 36 shows the comparison between the velocity measured by the hot film probe, V_p , and the velocity measured by the tunnel pitot static system, V_T , during both the Giromill test and during a flow survey test conducted in June 1977. In both tests the hot film probe measured lower than the pitot-static system but the difference was much larger during the Giromill test. Figure 37 shows the excellent agreement between the hot film probe velocity measurements and the Kollsman probe measurements obtained at the end of the Giromill test. Unfortunately, the transducer for the V_T system was used for the Kollsman probe and was therefore not available for measuring V_T .

The fact that the Kollsman and hot film probes agreed at the end of the Giromill test tends to give credibility to the hot film velocity but on the other hand no plausible explanation can be found for V_T to read too high. The upper velocity range used (28 fps) was in the region of previous calibrations of the tunnel system which had indicated good accuracy for V_T . The possibility of blockage or flow retardation at the hot film probe due to power extraction by the Giromill rotor was investigated. Figure 38 shows that the velocity difference was not correlatable with C_p indicating that the hot film probe was sufficiently away from the rotor to be unaffected by the rotor flow retardation.

Due to the lack of overwhelming evidence to support either velocity, and due to the significant effect of such a velocity variation on the results, it was decided to conduct separate analyses on the data under the assumption that either velocity could be correct and then draw conclusions based on each set of results which would then lead to some overall conclusions and recommendations.

8.1 Power Coefficient Based on Hot Film Probe Velocity V_p

In general, the test results were in excellent agreement with the predicted values at low λ 's, but the C_p drop off at high λ 's is not nearly as great as predicted. Figure 39 shows a comparison between the smoothed rock angle theoretical results and the test data resolved at the blade speed ratio design point for each cam. Figure 40 shows the comparison between the same test data and the vortex theory computed rock angle theoretical results. As explained in Section 6, the primary reason for the $\alpha_e = 9^\circ$ smoothed rock angle prediction showing such a degradation was that the predicted angle of attack for stall was 10 degrees. This angle was occasionally exceeded due to the rock angle smoothing. Since no degradation in performance was evident for $\alpha_e = 9^\circ$, it can be assumed that stall did not occur. This was due either to the real fluid induced angles of attack being smoothed or to the stall angle of attack being higher than predicted. The latter is the most likely reason

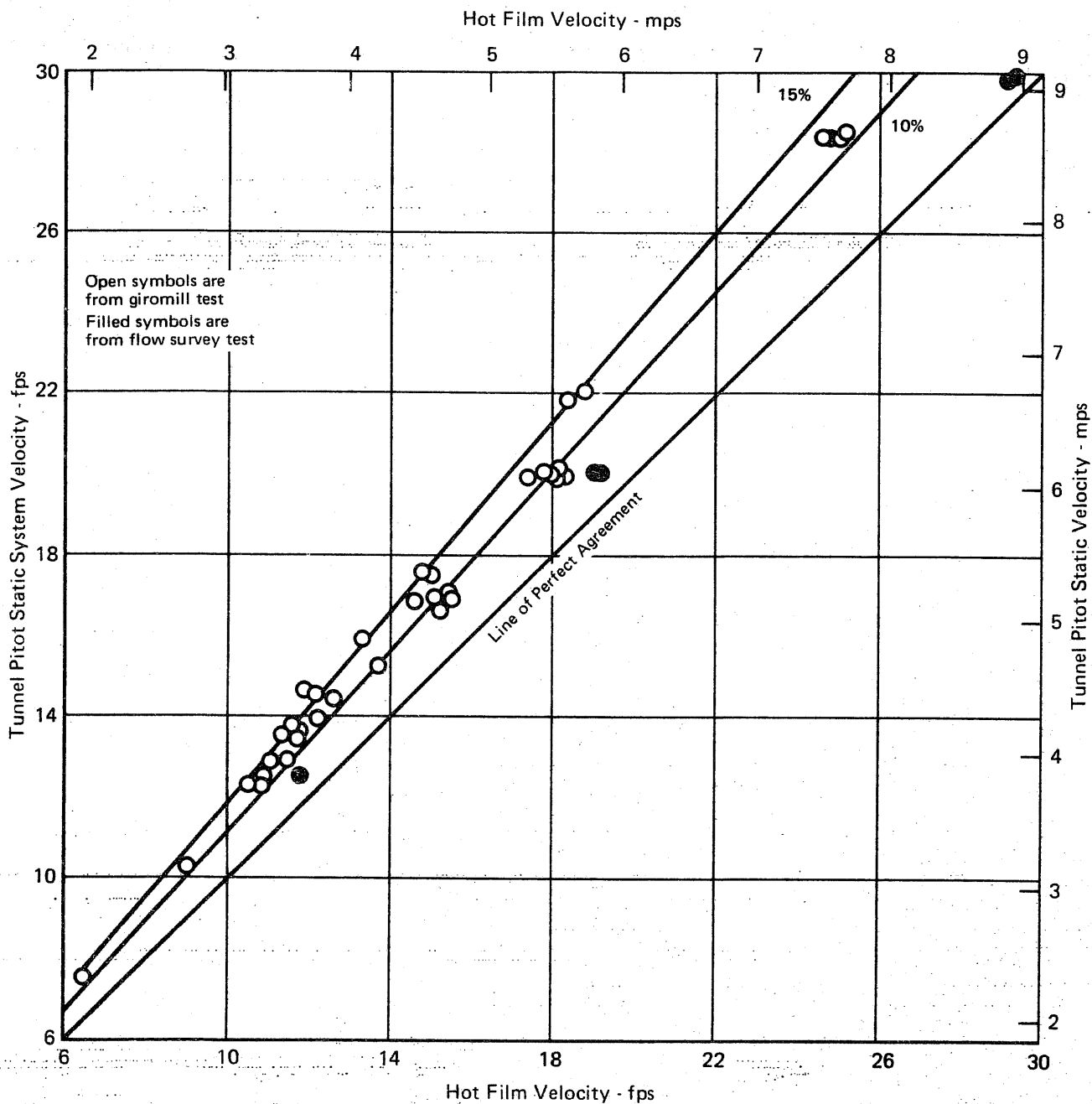


FIGURE 36
VELOCITY COMPARISON
HOT FILM PROBE vs PITOT-STATIC SYSTEM

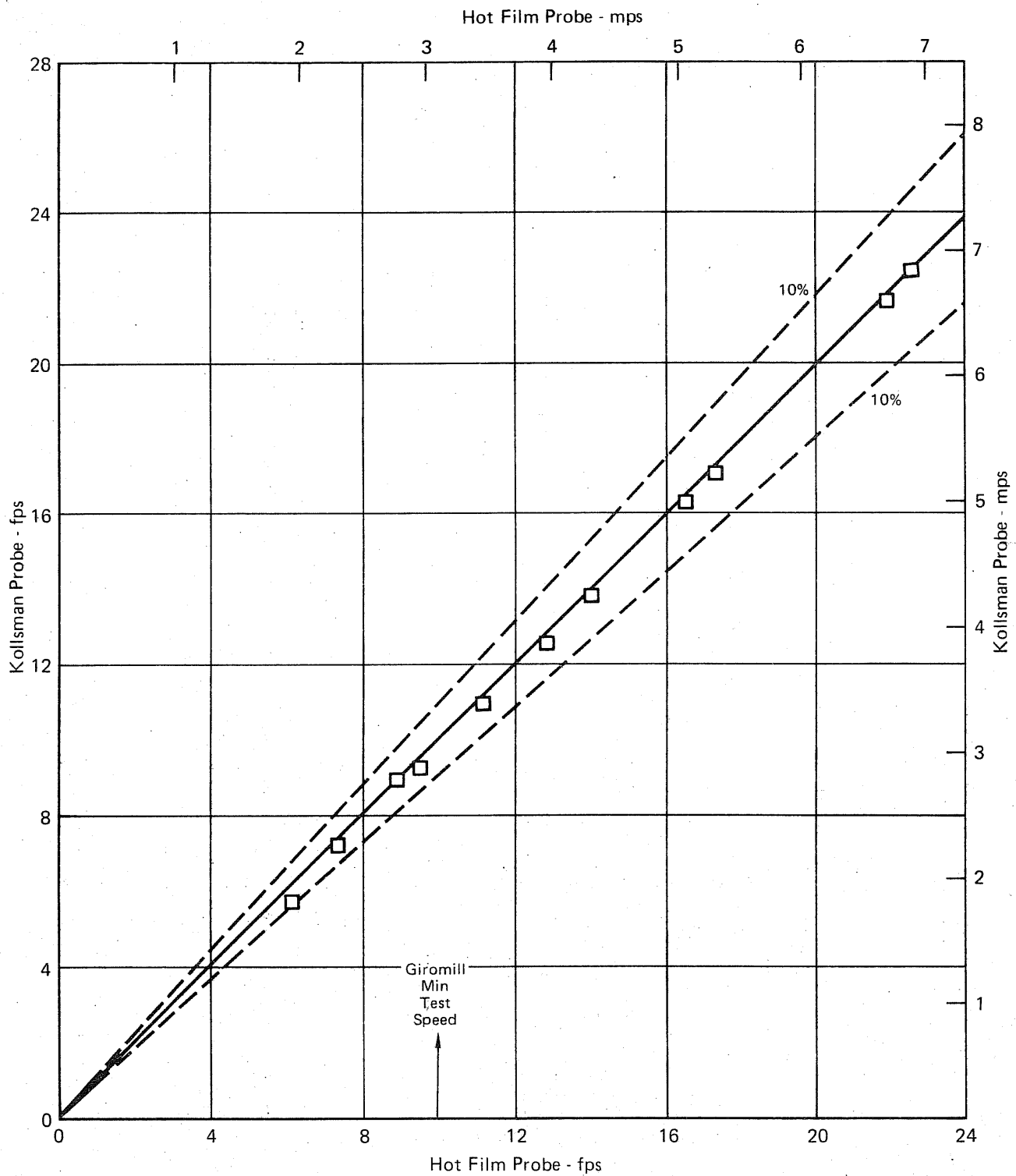


FIGURE 37
KOLLSMAN AND HOT FILM PROBE
VELOCITY COMPARISON

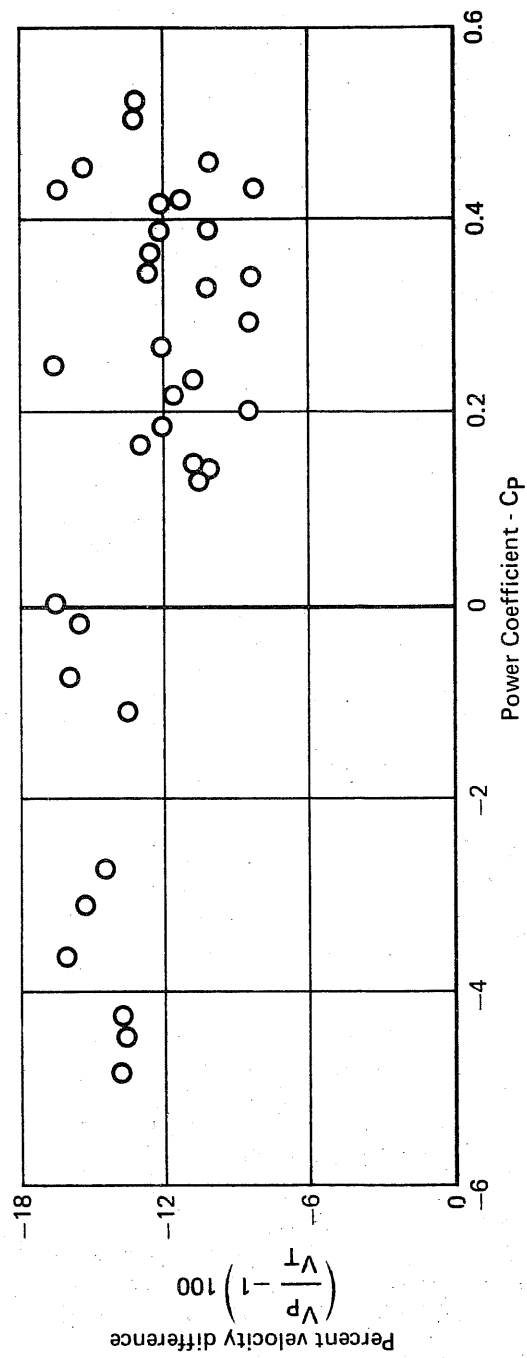


FIGURE 38
PERCENT VELOCITY DIFFERENCE BETWEEN TUNNEL SYSTEM
AND HOT FILM PROBE vs GIROMILL POWER COEFFICIENT

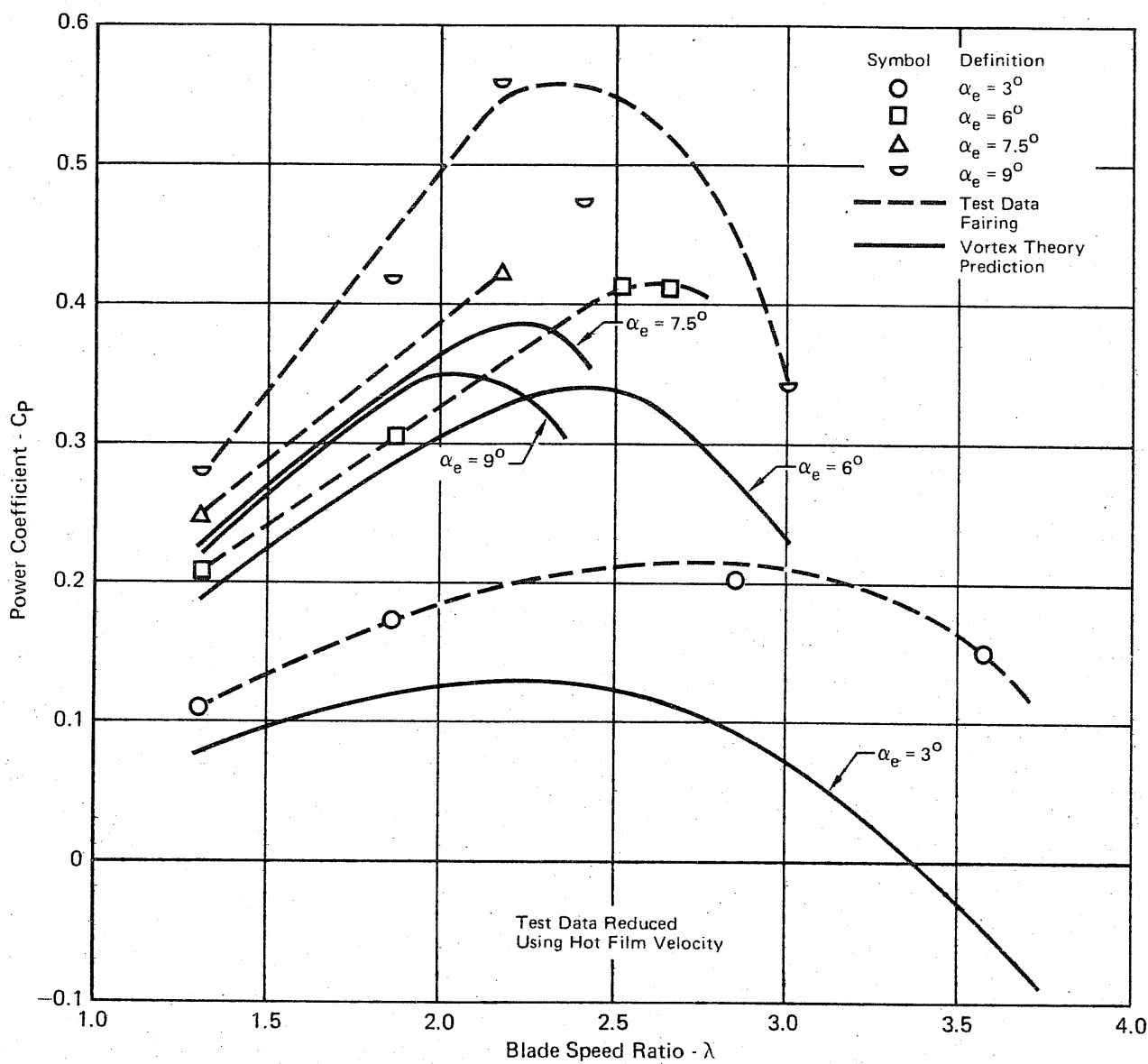


FIGURE 39
COMPARISON BETWEEN PREDICTED GIROMILL PERFORMANCE
AND TEST DATA AT THE CAM DESIGN POINTS
 Smoothed Rock Angles

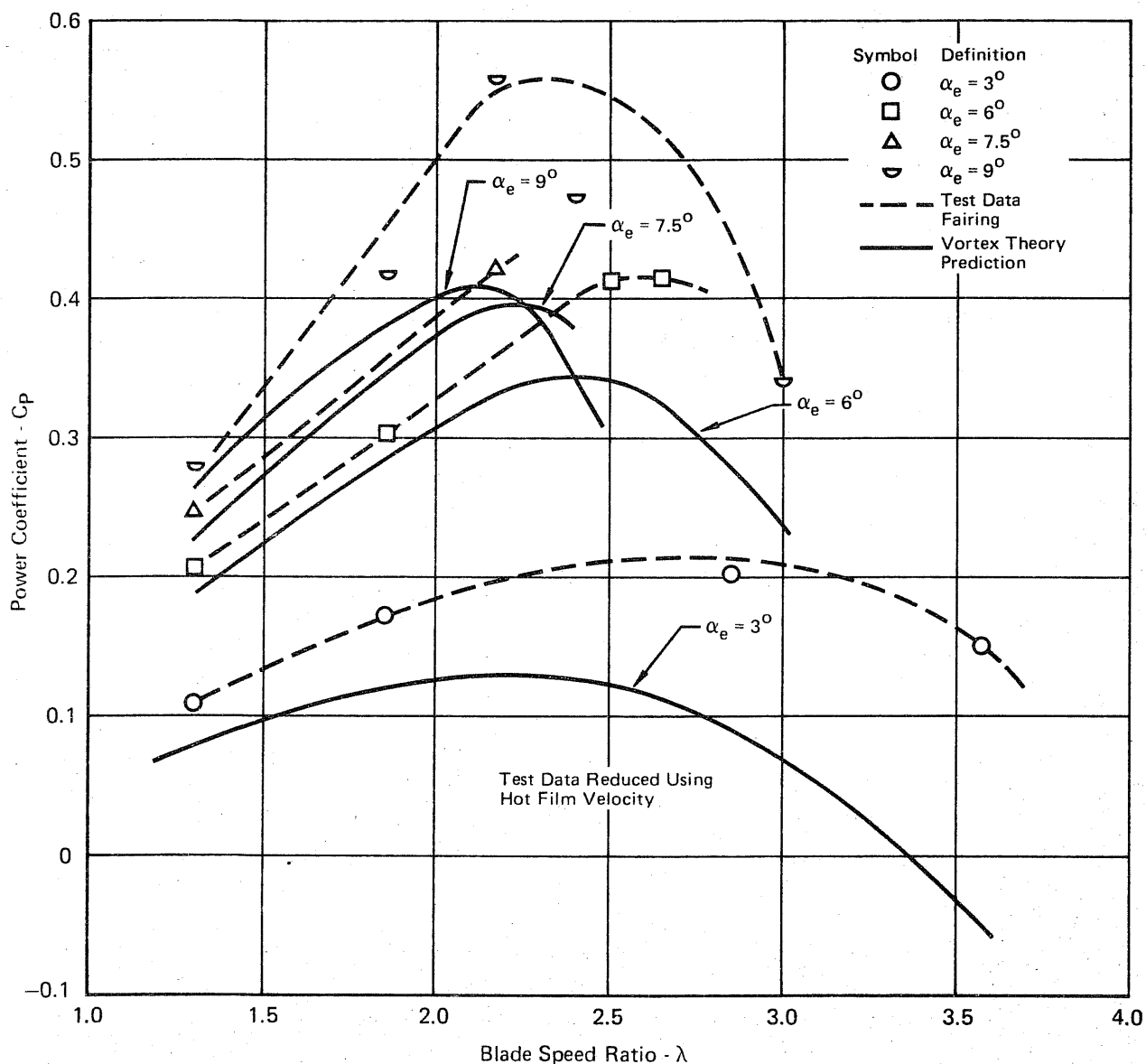


FIGURE 40
COMPARISON BETWEEN PREDICTED GIROMILL PERFORMANCE
AND TEST DATA AT THE CAM DESIGN POINTS
 Vortex Theory Computed Rock Angles

since any tunnel turbulence should serve to increase the effective RN and hence increase the stall angle of attack. Also, airfoils experiencing angle of attack oscillations have been shown to attain peak α 's higher than that for static stall without stalling.

The test data points shown in Figures 39 and 40 were obtained from Figures 41 through 44 and are generally the result of an extrapolation of C_p vs λ obtained during the λ sweeps for a given cam. This was due to the fact that calculation of λ based on hot film velocity shifts the data to higher values of this parameter. In most cases, the extrapolation was small and for the peak power points, none was required.

Three runs were conducted with cam 1, the peak power cam. As can be seen in Figure 44 two runs repeated well but the C_p for run 38 was 20% higher than the others. Run 38, the 2nd repeat run with cam 1, was run because of suspected zero shift problems with runs 8 and 20. Investigation of torque meter zero shift and recalibration of the torque meter after run 39 showed no indications of any problems associated with the torque meter for run 38. Evidence exists however, that the C_p values for runs 8 and 20 should be increased. The pre test tare run using cam 6 was conducted 2 runs prior to run 8 (run 6) and indicated an unusually high tare torque (See Figure 45). This tare value was not used for the data reduction; the post test tares were used. However, whatever condition was causing the high torque in run 6 apparently existed for runs 7 and 8. Additionally, run 20 had a 43 count (14.3 in. lb.) zero return at the end of the run. Adding this zero shift to the running torque shifts it up to the vicinity of run 38.

Validation of the run 38 C_p is also obtained from runs 9 through 12 (Figure 46). These runs are not expected to be greatly different from the peak power runs since the cam variations were minor (see Figure 33 groups 2 and 3 for a description of these cams).

The low C_p values for run 12 are disturbing however since no large torque zero shift occurred during this run. However, the hot film probe velocity and the tunnel system velocity agreed within about 8.5% on run 12 which is unusually good agreement. As will be seen later, when tunnel velocity is used to reduce the data, no difference is seen between run 11 and run 12 results.

The difference between runs 14 and 39 are accounted for by a 21 in. lb. torque meter zero shift between the pre run zero and the post run zero on run 14. The actual difference between run 14 and run 39 ranged from 16 to 21 in. lb.

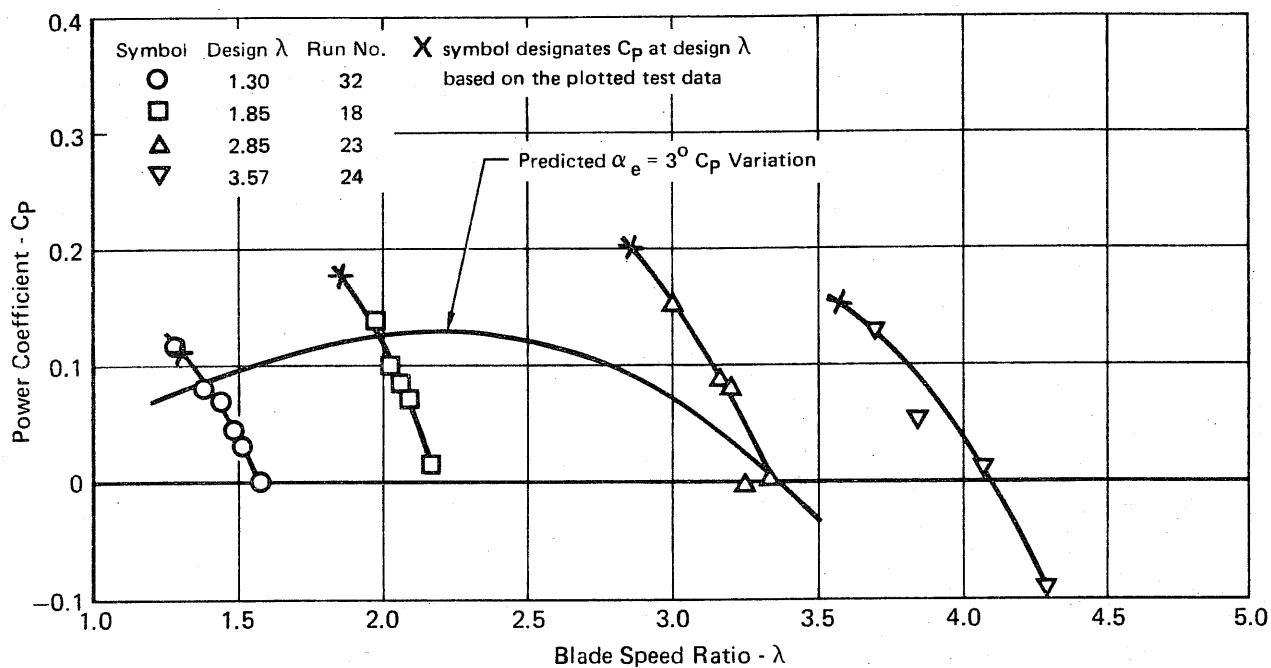


FIGURE 41
GIROMILL
POWER COEFFICIENT VARIATION WITH BLADE SPEED RATIO
 Based on Hot Film Velocity
 $\alpha_e = 3^\circ$

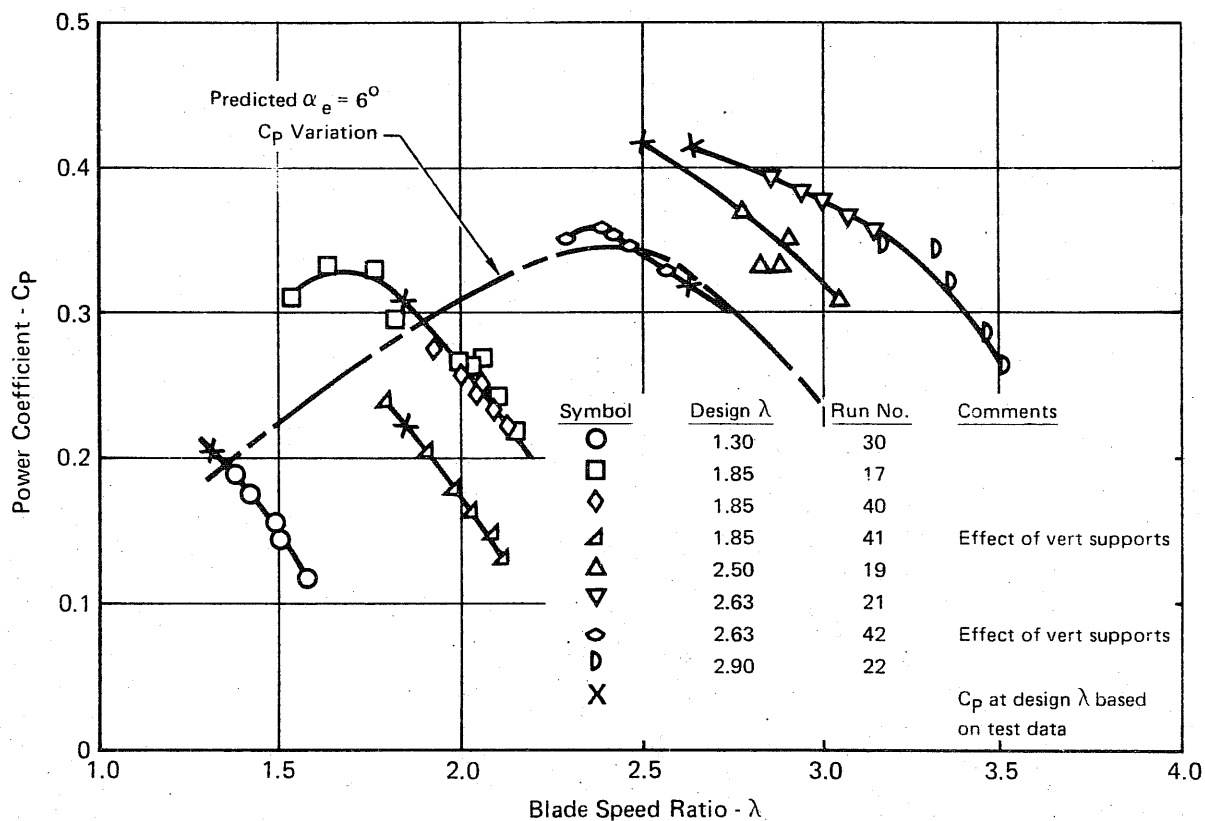


FIGURE 42
GIROMILL
POWER COEFFICIENT VARIATION WITH BLADE SPEED RATIO
Based on Hot Film Velocity
 $\alpha_e = 6^\circ$

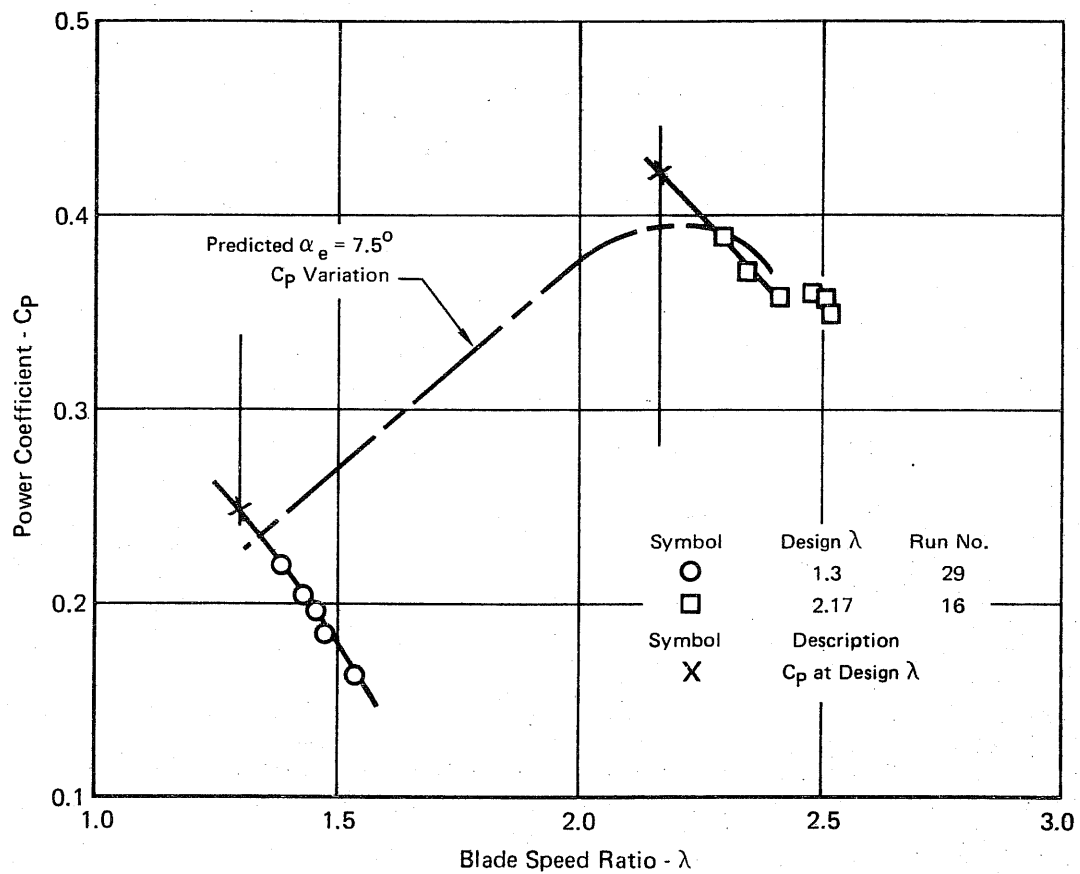


FIGURE 43
GIROMILL
POWER COEFFICIENT VARIATION WITH BLADE SPEED RATIO
 Based on Hot Film Velocity
 $\alpha_e = 7.5^\circ$

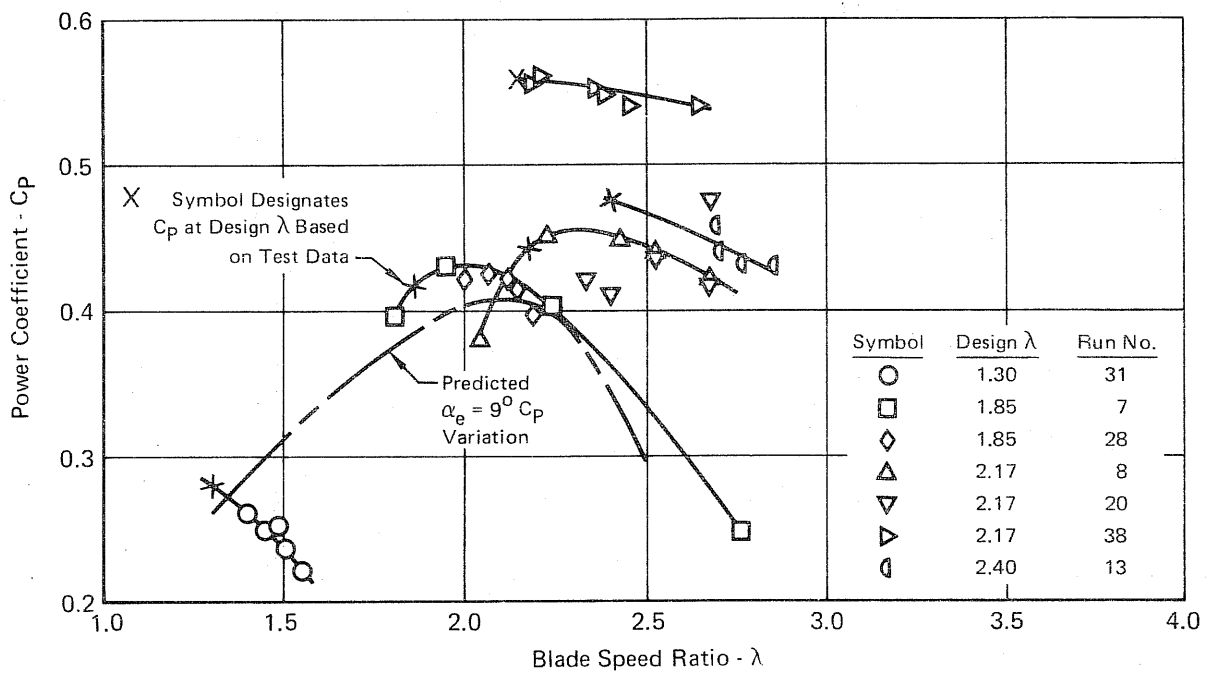


FIGURE 44
GIROMILL
POWER COEFFICIENT VARIATION WITH BLADE SPEED RATIO
 Based on Hot Film Velocity
 $\alpha_e = 9^\circ$

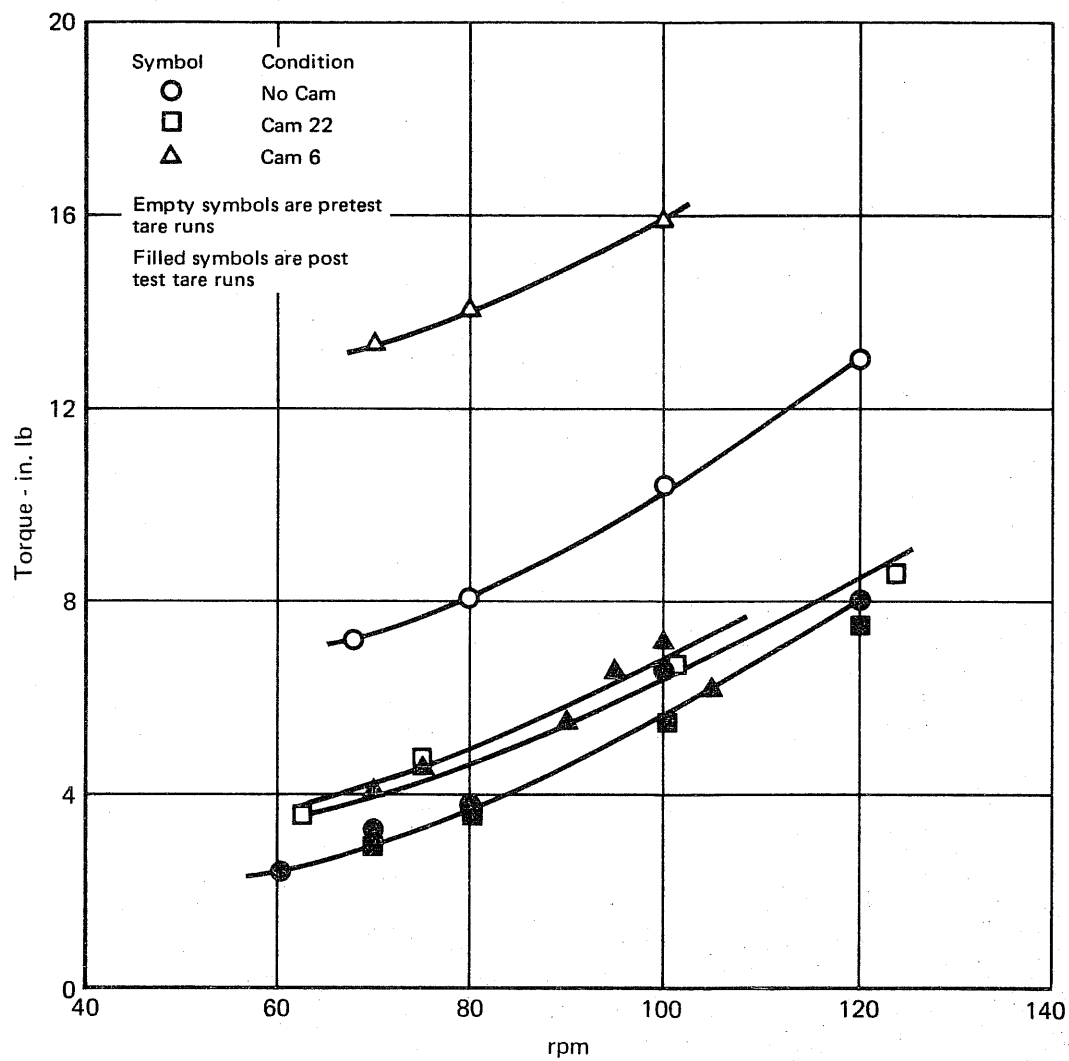


FIGURE 45
TARE RUN DATA

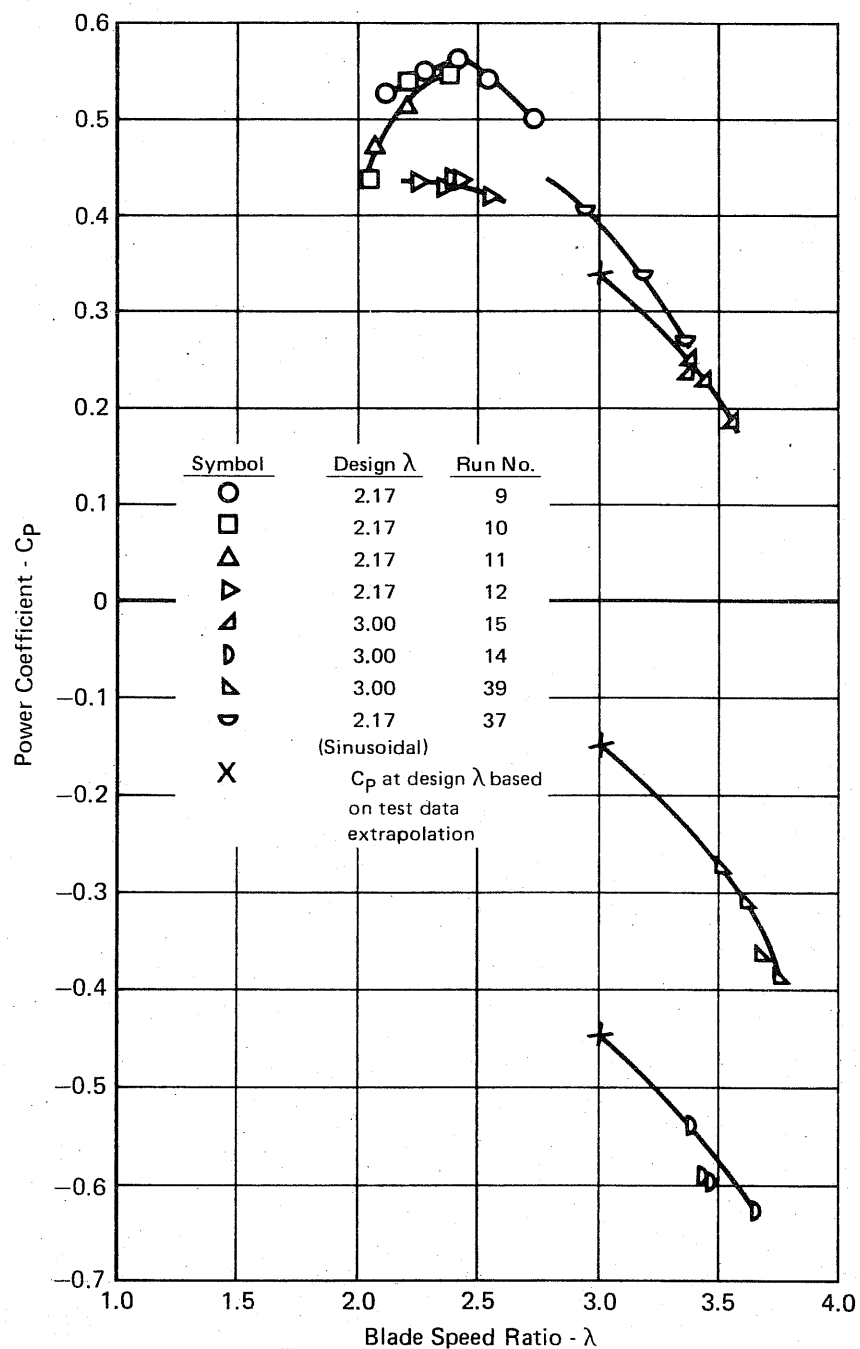


FIGURE 46
GIROMILL
POWER COEFFICIENT VARIATION WITH BLADE SPEED RATIO
 Based on Hot Film Velocity
 $\alpha_e = 9^\circ$
 Special Cam Variations

Run 37 in Figure 46 is the sinusoidal mode. The cam was designed to produce a sinusoidal modulation, $\theta = \theta_0 + \sin(a\psi + b)$, that was the best least squares fit to the actual $\alpha_e = 9^\circ$, $\lambda = 2.17$ blade modulation. These were inadvertently run with the wrong blade speed ratio schedule but the results appear to be slightly less than the exact blade modulation results in Figure 45. Runs 41 and 42 of Figure 42 were with the dummy vertical support struts installed. These struts had significant adverse effects on power coefficient. A decrease in C_p of about .09 was evident from the runs when compared with no support struts, runs 40 and 21. The significance of this is that large Giromills that would require struts of this type for structural support could experience a significant C_p reduction.

The general trend of C_p with λ for a given Giromill cam is as expected throughout the range tested. Increasing the blade speed ratio from the design point results in generally decreased angles of attack and therefore less C_p .

If the hot film velocity is correct, then the following conclusions and observations apply to the Giromill mode results:

(1) The vortex theory program is quite accurate in predicting the low λ performance but significantly underpredicts the high λ performance. It appears logical for the vortex theory program to accurately predict the performance at low λ , even though the blade modulation is quite severe, since the induced flow effects, which should be the major source of error in the program, are small at low λ . The rigid cam and push rod mechanism of the test model provided extremely accurate blade modulation even at the low λ conditions where large modulations are required.

(2) Under-prediction at the high λ values is possible since the vortex theory program has convergence problems at high λ 's as discussed in Reference 1. Also the induced flow on the downwind ($\psi = 180^\circ$) portion of the rotor is very large. Inaccurate induced flow computation would result in inaccurate blade modulation profiles which in turn adversely affect performance of the model. This seems to be the case for run 13, Figure 44, and run 39, Figure 46. These cams did not produce the maximum C_p possible for those blade speed ratios. This is evident, for example, by noting that run 38, Figure 44, which had a cam designed for $\lambda = 2.17$, produced a higher C_p at $\lambda = 2.4$ than did run 13 which was designed for $\lambda = 2.4$.

The Darrieus mode results are shown in Figure 47 along with those of the two modified Darrieus modes which were described in Section 7. The $\bar{+}3^\circ$ flip mode serves to reduce the blade angle of attack and the $\bar{+}3^\circ$ flip mode increases angle of attack over that which is attained on the standard Darrieus blade.

From Figure 47 it can be seen that the $\bar{+}3^\circ$ flip mode and the standard Darrieus mode results cross at $\lambda = 6.0$, and at λ 's below 6 the $\bar{+}3^\circ$ flip mode has higher C_p

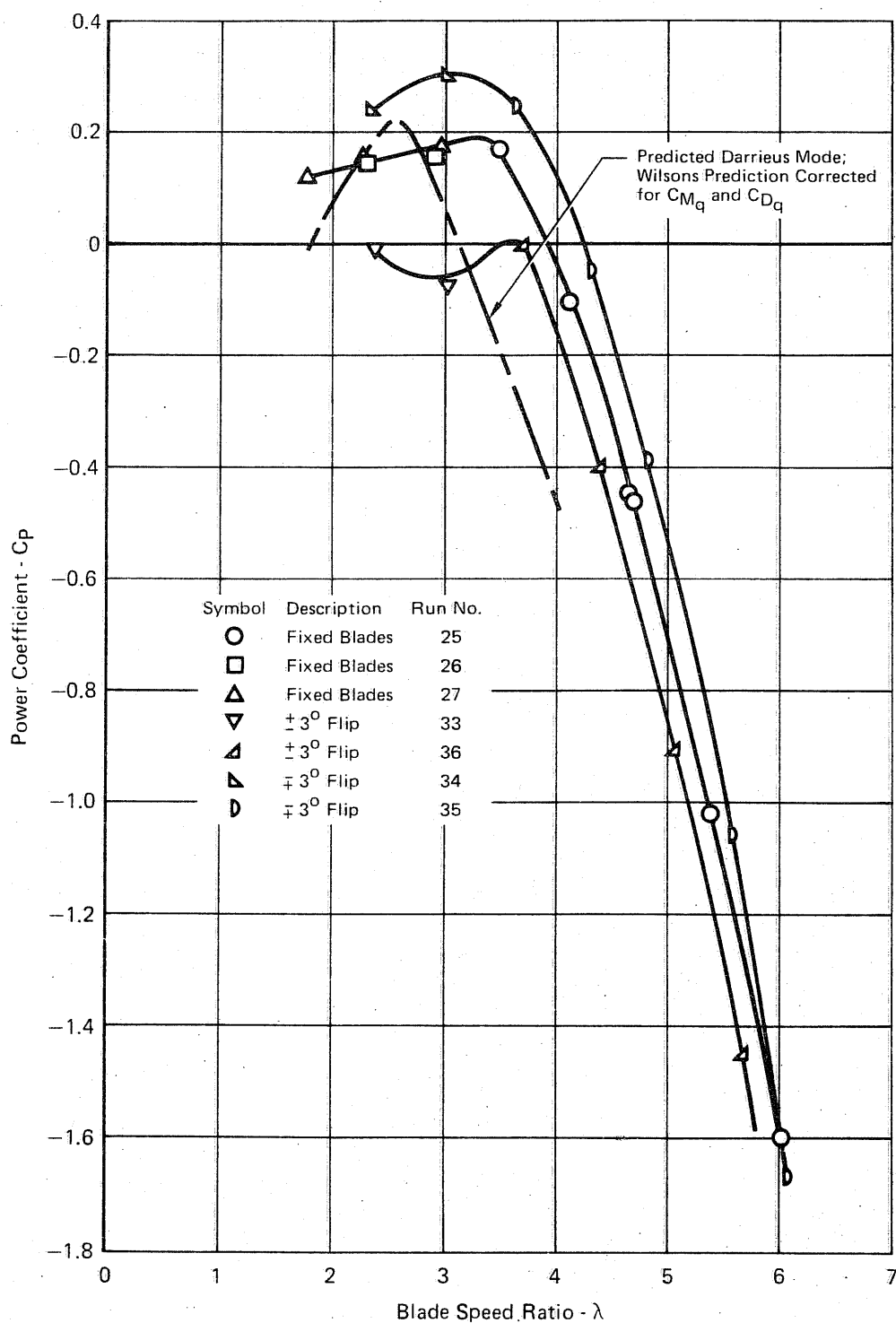


FIGURE 47
DARRIEUS MODE
POWER COEFFICIENT VARIATION WITH BLADE SPEED RATIO
 Based on Hot Film Velocity

values than Darrieus. It seems apparent that the only reason for a reduced angle of attack (as produced by the $\mp 3^\circ$ flip) to result in increased C_p values is that the standard Darrieus configuration (fixed blades) suffers stall over a phase angle region extensive enough to adversely affect performance at blade speed ratios less than 6.0

It is interesting to note that the maximum angle of attack due to the relative wind angle only (no induced effects) is 9.7° at $\lambda = 6$. Since this is near the predicted stall angle of attack and since stall is apparently occurring here it appears that induced effects on the upwind segment are not large. If there were a large flow retardation ahead of the model the blade angle of attack would remain below stall for some region of λ below 6.0 and the Darrieus C_p values would be greater than the $\mp 3^\circ$ flip results.

The predicted Darrieus performance does not compare well with the wind tunnel results for several possible reasons. An accurate estimate for the stall angle of attack and the lift and drag characteristics above stall are critical in performance prediction at λ 's where stall occurs. These characteristics are difficult to predict especially under conditions of time varying angle of attack and Reynolds number. Also, an accurate calculation of the rotor induced flow field is required since that in turn determines the blade angle of attack. This is a difficult theoretical problem. The flow field approximation in the strip theory analysis are described in Reference 9. Additionally, the values of C_{mq} and C_{Lq} used to correct for rotation rate effects were derived based on unstalled linear aerodynamic characteristics. These effects can be quite different, even of opposite sign, in the stall regime.

8.2 Power Coefficient Based on Pitot-Static Velocity

Figure 48 shows a comparison between the idealized rock angle predicted C_p envelope and the C_p data obtained from the test using the tunnel pitot-static system for velocity measurement. The data for Figure 47 was obtained from Figures 49 through 52 which present C_p data for the λ sweeps conducted with the various cams. As can be seen from these figures, the test data is much lower than predicted at the low blade speed ratios and is in closer agreement at the higher blade speed ratios.

As discussed in Section 8.1 there is reason to believe that runs 8 and 20 should actually be raised to the vicinity of run 38. Figure 52 also shows run 7 to be below repeat run 28. This is consistent with the logic exposed in Section 8.1 which theorized that the friction torque in runs 7 and 8 may be about 9 inch lb. higher than the remaining runs based on the fact that run 6 (tare run) torque was unusually high.

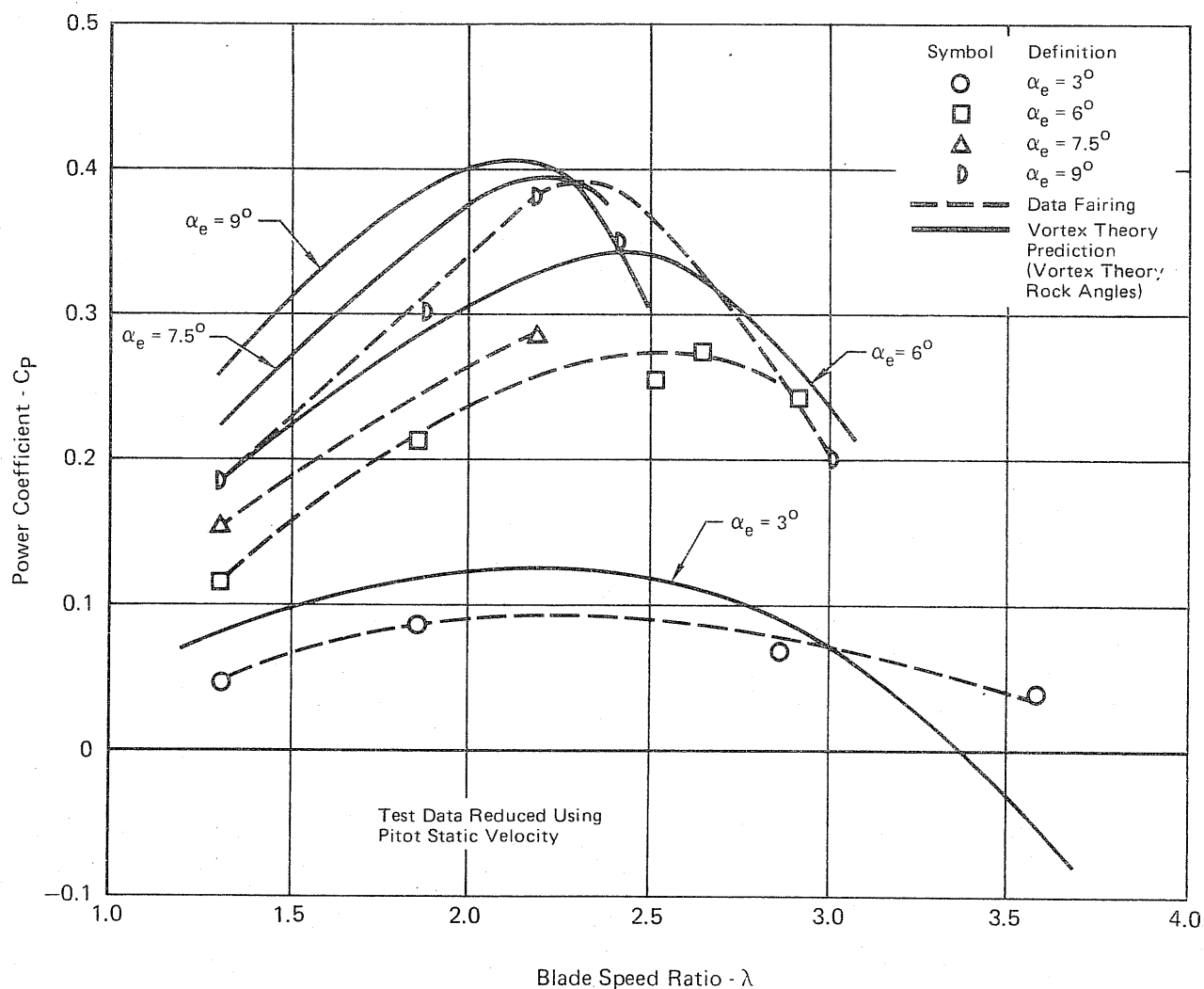


FIGURE 48
COMPARISON BETWEEN PREDICTED GIROMILL PERFORMANCE
AND TEST DATA AT THE CAM DESIGN POINTS

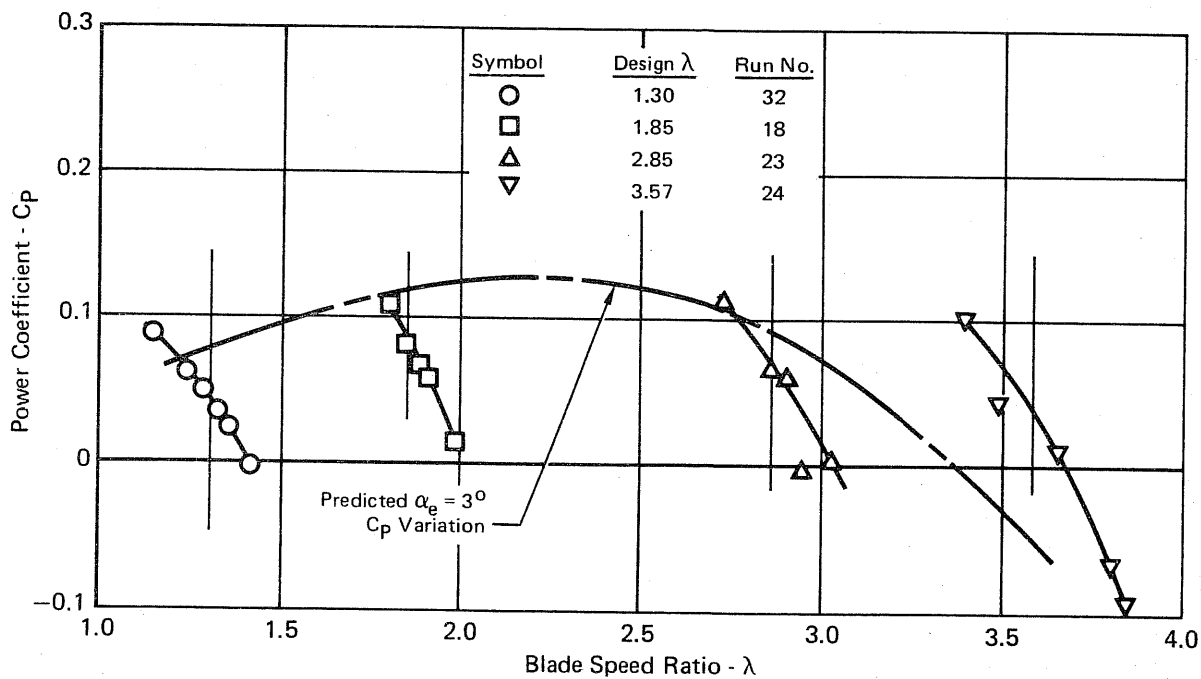


FIGURE 49
GIROMILL
POWER COEFFICIENT VARIATION WITH BLADE SPEED RATIO
 Based on Pitot-Static Velocity
 $\alpha_e = 3^\circ$

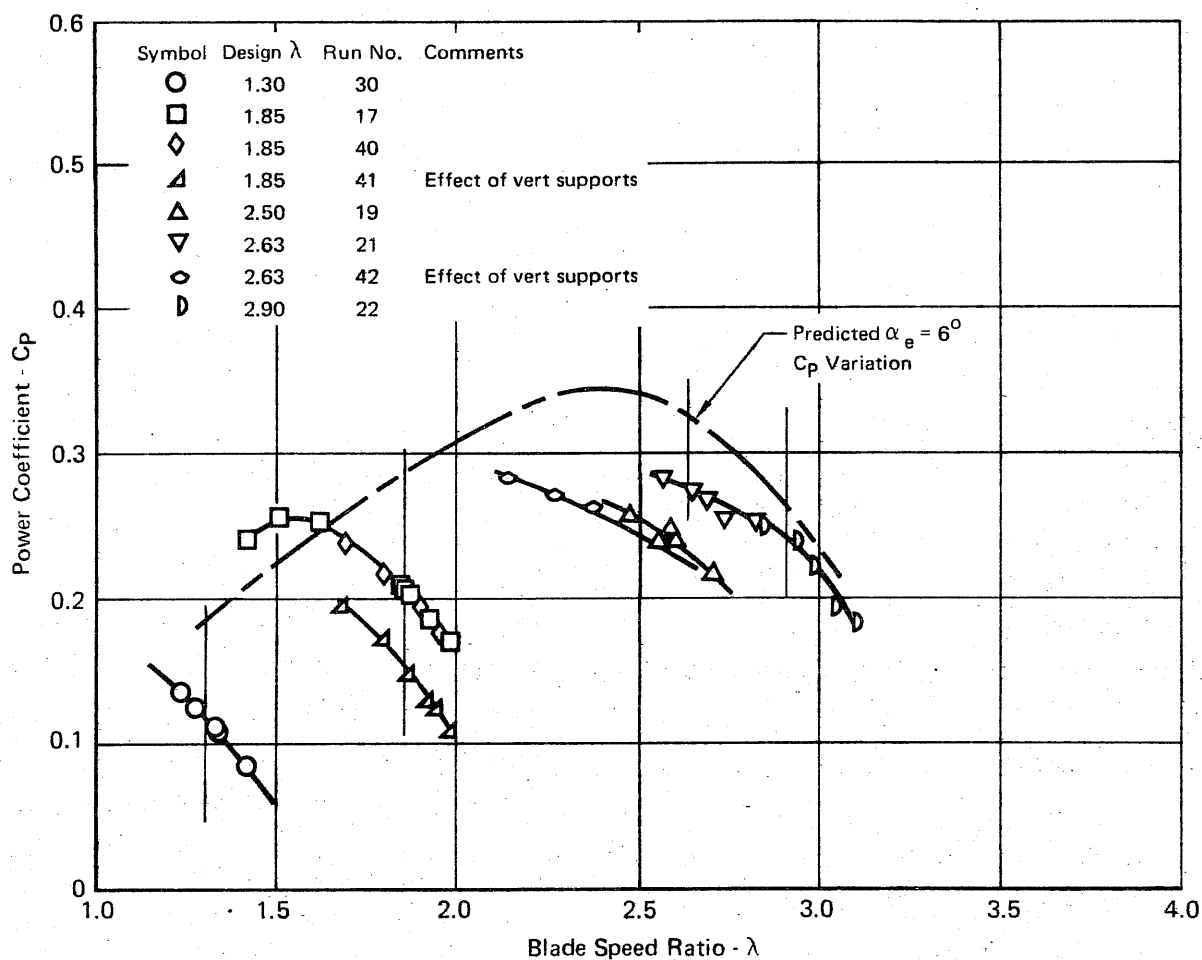


FIGURE 50
GIROMILL
POWER COEFFICIENT VARIATION WITH BLADE SPEED RATIO
 Based on Pitot Static Velocity
 $\alpha_e = 6^\circ$

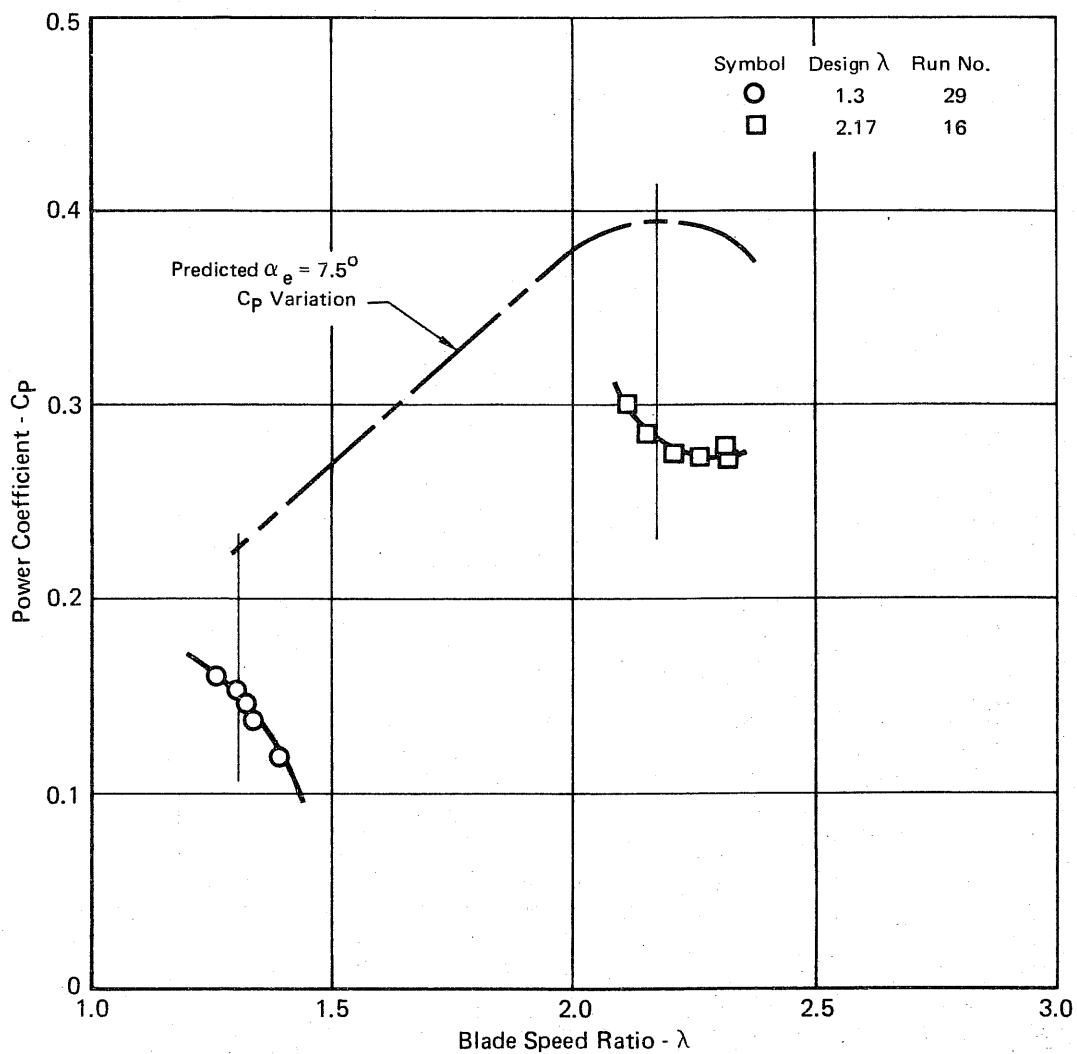


FIGURE 51
GIROMILL
POWER COEFFICIENT VARIATION WITH BLADE SPEED RATIO
Based on Pitot-Static Velocity
 $\alpha_e = 7.5^\circ$

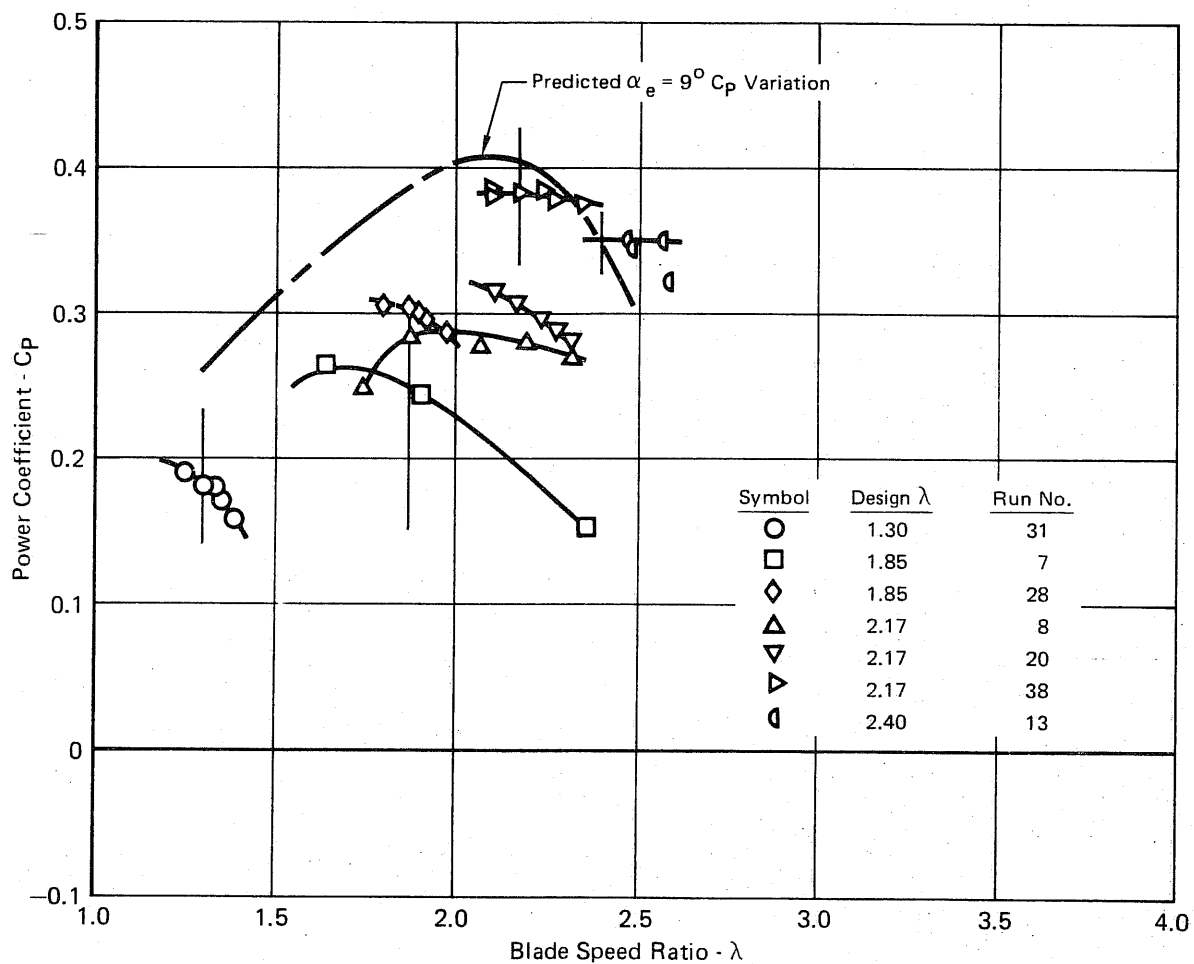


FIGURE 52
GIROMILL
POWER COEFFICIENT VARIATION WITH BLADE SPEED RATIO
 Based on Pitot Static Velocity
 $\alpha_e = 9^\circ$

GP77-0810-2

Runs 9 through 12 of Figure 53 support run 38 in that they were minor modifications of the peak power cam and were therefore expected to produce C_p values close to peak C_p . The difference between run 14 and 39 was previously explained in Section 8.1.

Figure 54 shows that the test results are in better agreement with the predicted results than in Figure 47. The discussion in Section 8.1 still applies here however.

If the pitot-static velocity is assumed to be correct, the following observations and conclusions apply:

- (1) The test values of C_p are significantly lower than predicted except at the high values of λ where the predicted C_p falls off much faster than the test C_p .
- (2) The maximum C_p is only about 7% less than predicted.
- (3) The overprediction of C_p at the low λ 's is surprising since as explained in Section 8.1, this should be the region of highest confidence. The rapid fall off in predicted C_p at high λ is also explained in Section 8.1 as probably being due to convergence problems discussed in Reference 1.
- (4) In any event, the peak C_p is close to the predicted value and the C_p at higher λ appears to have the potential of being higher than predicted. This is significant, since the low λ values are associated with higher than rated wind speeds and the Giromill would be operating at reduced C_p 's in order not to exceed rated power. The high λ 's are associated with wind speeds lower than rated power and therefore the largest C_p possible is needed.

8.3 Comparison of Hot Film and Pitot Static Results

Figure 55 shows the envelope of test results obtained using V_t as the normalizing velocity, and Figure 56 shows the envelope obtained using V_p . Figure 57 compares these envelopes to the predicted Giromill power coefficients.

The V_T test results give the closest overall agreement with the predicted results. The underprediction at low λ is, as explained in Section 8.1, surprising but not a detriment to performance since the Giromill will have to operate at even further reduced C_p at λ 's below that for peak C_p in order to avoid exceeding the rated power limitation.

8.4 Analog Magnetic Tape Data

Data from all the runs were collected on analog magnetic tape as a backup to the filtered digital data that were used to determine performance. Some runs were plotted from the tape to provide a check on the filtered digital data and to inspect

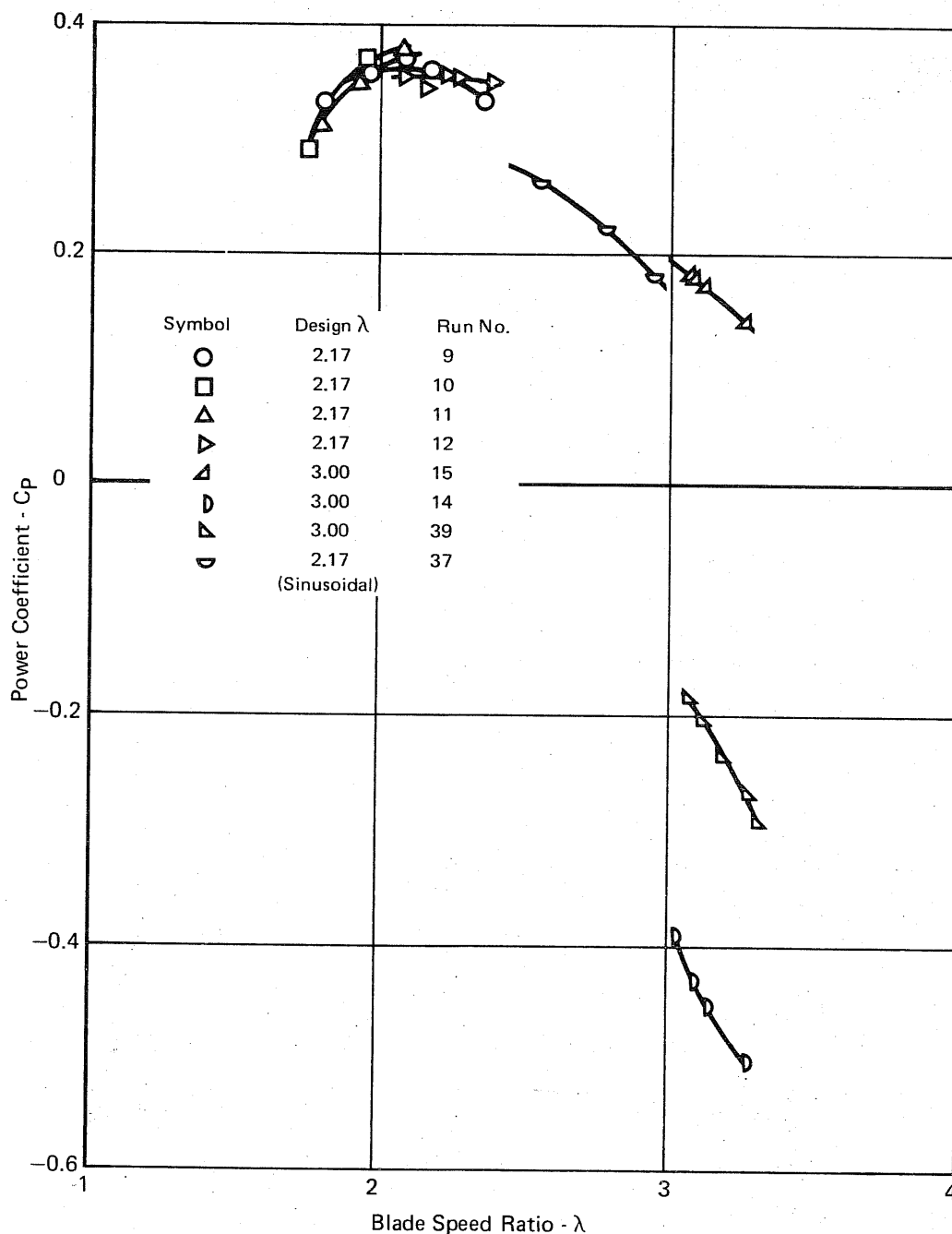


FIGURE 53
GIROMILL
POWER COEFFICIENT VARIATION WITH BLADE SPEED RATIO
 Based on Pitot-Static Velocity
 $\alpha_e = 9^\circ$
 Special Cam Variations

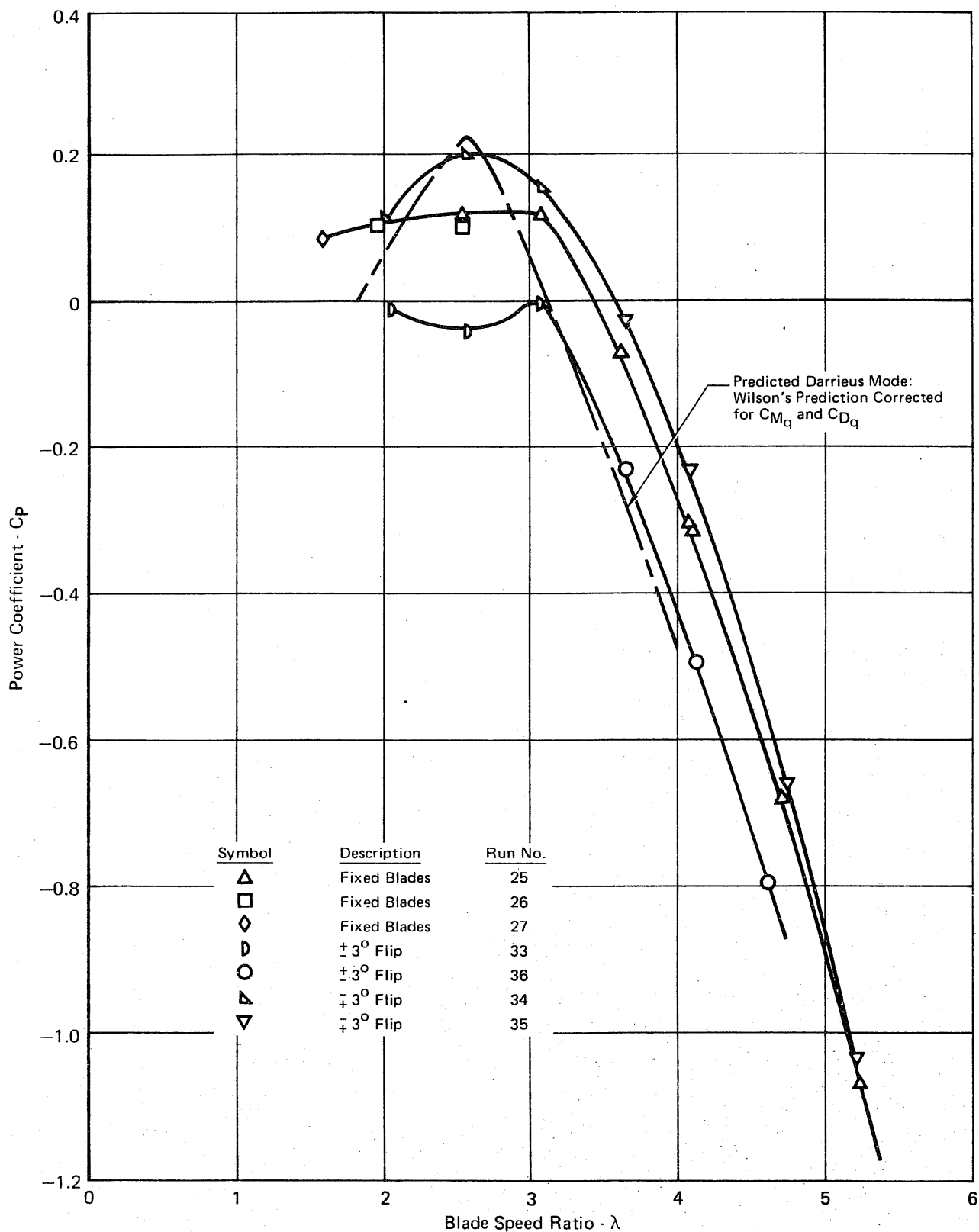


FIGURE 54
DARRIEUS MODE
POWER COEFFICIENT VARIATION WITH BLADE SPEED RATIO
 Based on Pitot-Static Velocity

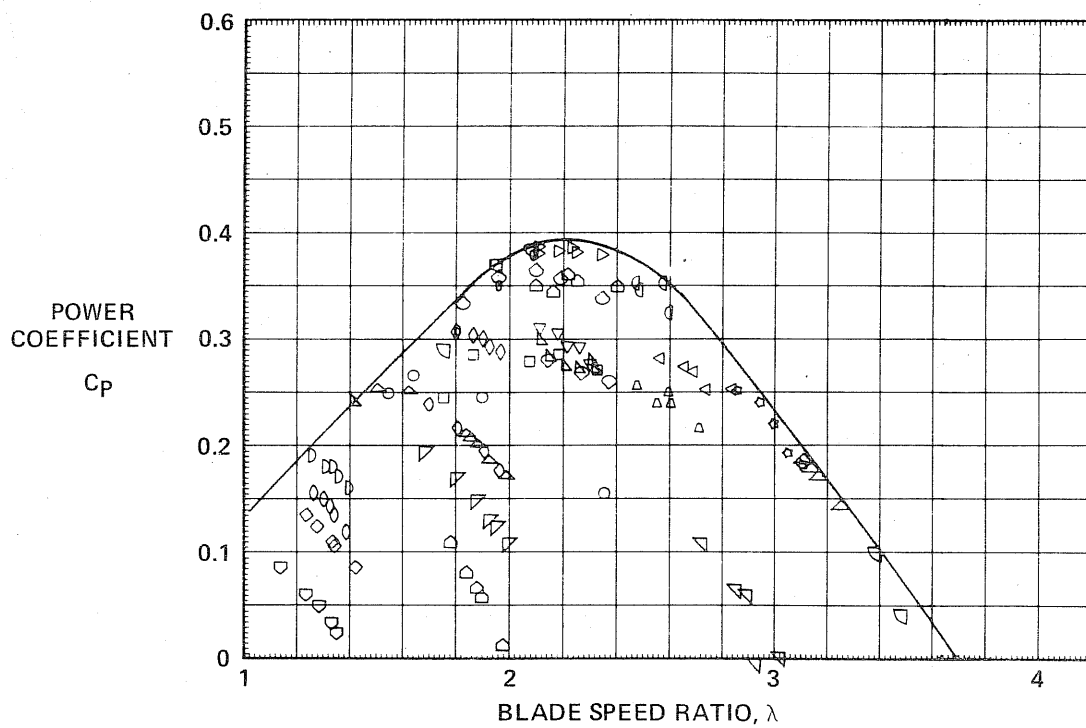


FIGURE 55
GIROMILL WIND TUNNEL TEST MODEL PERFORMANCE ENVELOPE
 Normalized Using Tunnel System Velocity

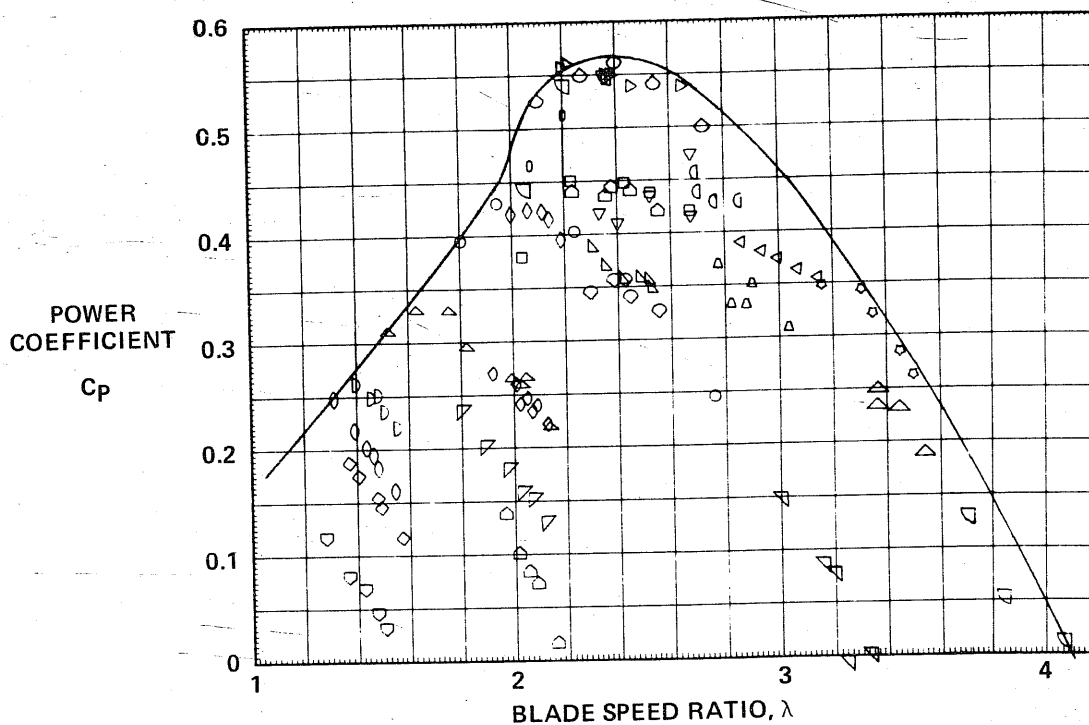


FIGURE 56
GIROMILL WIND TUNNEL TEST MODEL PERFORMANCE ENVELOPE
 Normalized Using Hot Film Anemometer Velocity

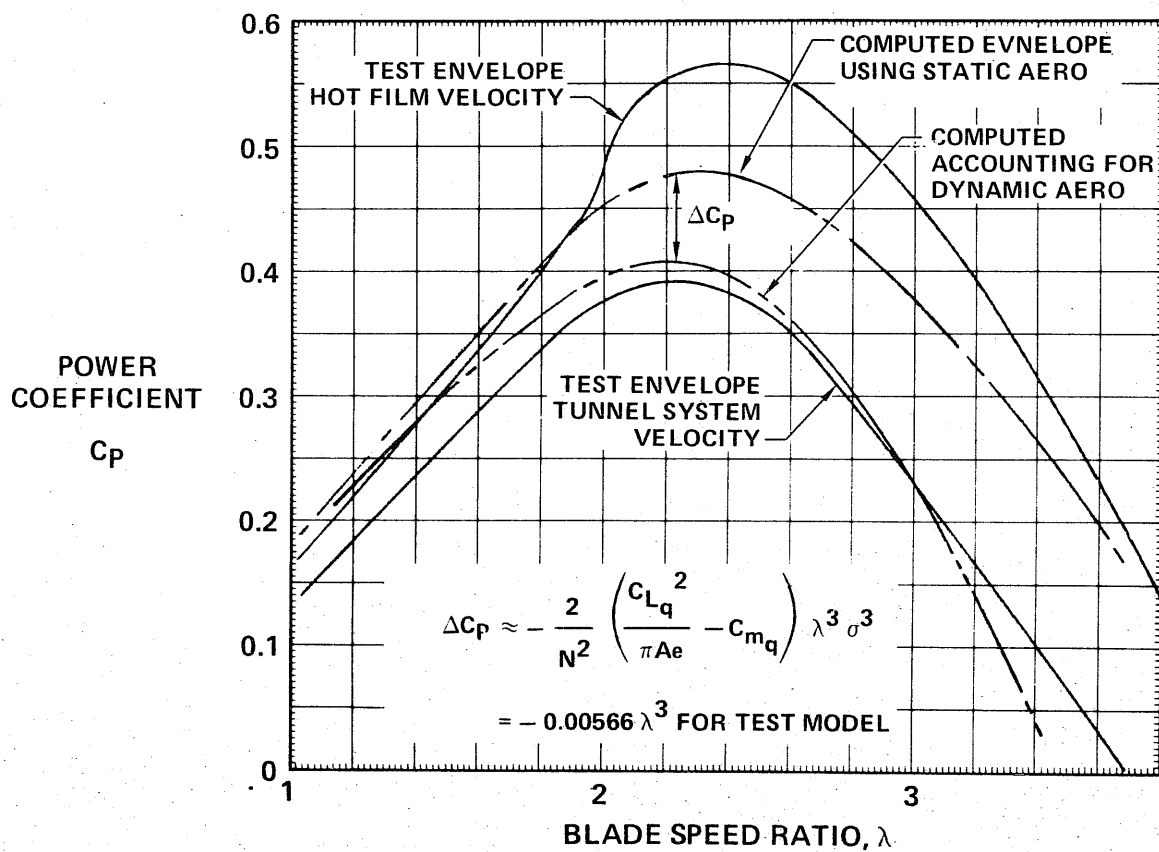


FIGURE 57
COMPARISON OF COMPUTED AND TEST GIROMILL
PERFORMANCE ENVELOPES

the time variation of torque and RPM. Figure 58 shows an example of this data from run 20. Comparing the blade phase angle (ψ) versus time trace with the average RPM obtained from the RPM trace shows agreement to within 0.4 RPM. The spike in ψ just after going from 360° to 0° is an induced voltage spike due to the rapid voltage transient.

Average values of torque and RPM generally compared well with the filtered digital data so that further analysis using the analog magnetic tape was not considered necessary.

9. CONCLUSIONS

The Giromill wind tunnel test results show the Giromill to have good performance, nearly equal to or possibly better than that predicted by the Larsen cyclogiro vortex theory program.

Due to the unresolved discrepancy between the two velocity measurement systems used during the test, the higher than predicted performance indicated by the use of the hot film velocity cannot be verified. Until further tests verify the high C_p values, the vortex theory program will be used for performance prediction.

A simplified relationship was derived to determine the aerodynamic effect of rotation rate on power output. The rotational effects are not presently accounted for in the Larsen vortex theory program or in the strip theory methods used for Darrieus performance prediction.

The rotation rate effect causes a degradation in C_p which is a function of the cube of both solidity and blade speed ratio. This was significant for the test model but will be much less for full scale models because of the lower solidity.

Inclusion of vertical support arm stabilizers at the $1/2$ radius position had a significant ($\Delta C_p \approx .09$) effect on performance and use of this type of support should be avoided.

Using the Larsen cyclogiro vortex theory program for Reynolds numbers and solidities associated with full scale Giromills, maximum C_p values are predicted that are higher than that attained with the wind tunnel model. For a Giromill 60 ft. (18.3m) in diameter, with blades 30 ft. (9.1m) in span having an aspect ratio of 12, and with a solidity of .125, a maximum C_p of .54 is obtained.

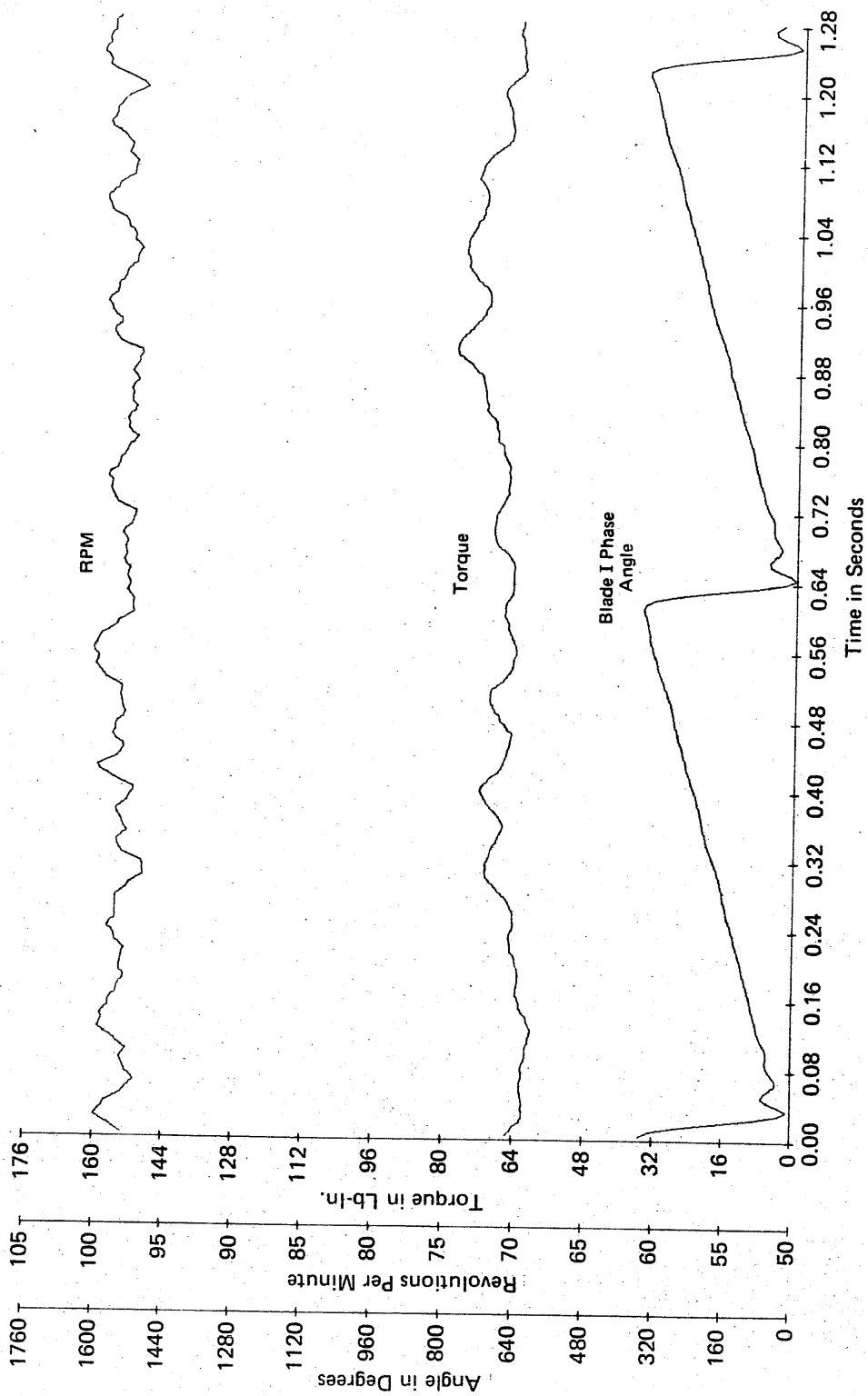


FIGURE 58
GIROMILL WIND TUNNEL TEST ANALOG TAPE DATA REDUCTION

10. REFERENCES

1. Brulle, R. V., et. al., "Feasibility Investigation of the Giromill for Generation of Electrical Power," ERDA Report C00-2617-75/1, Midterm Report, November 1975.
2. Brulle, R. V., "Feasibility Investigation of the Giromill for Generation of Electrical Power," ERDA Report C00-2617-76/1, Final Report, to be published.
3. Blackwell, B. F., Sheldahl, R. E., Felts, L. V., "Wind Tunnel Performance Data for the Darrieus Wind Turbine with NACA 0012 Blades," Sandia Laboratories Report SAND76-0130, May 1976.
4. Jacobs, E., Sherman, A., "Airfoil Section Characteristics as Affected by Variation in Reynolds Number," NACA Report 586, 1937.
5. Larsen, H. C., Low Reynolds Number Tests of Various Airfoils in the 5 Foot AFIT/END Wind Tunnel, Unpublished data dated 1950 from the Air Force Institute of Technology, Wright-Patterson AFB, Ohio.
6. Abbot, I. H., Von Doenhoff, A. E., "Theory of Wing Sections," Dover Publications, 1959.
7. Hoerner, S. F., "Fluid Dynamic Drag," Published by the Author in 1965, 148 Busted Dr., Midland Park, N.J. 07432.
8. Finck, R. D., "USAF Stability and Control DATCOM," Revised Jan 1975.
9. Wilson, R. E., Lissaman, P. B. S., and Walker, S. N., "Aerodynamic Performance of Wind Turbines", Oregon State University, June 1976.